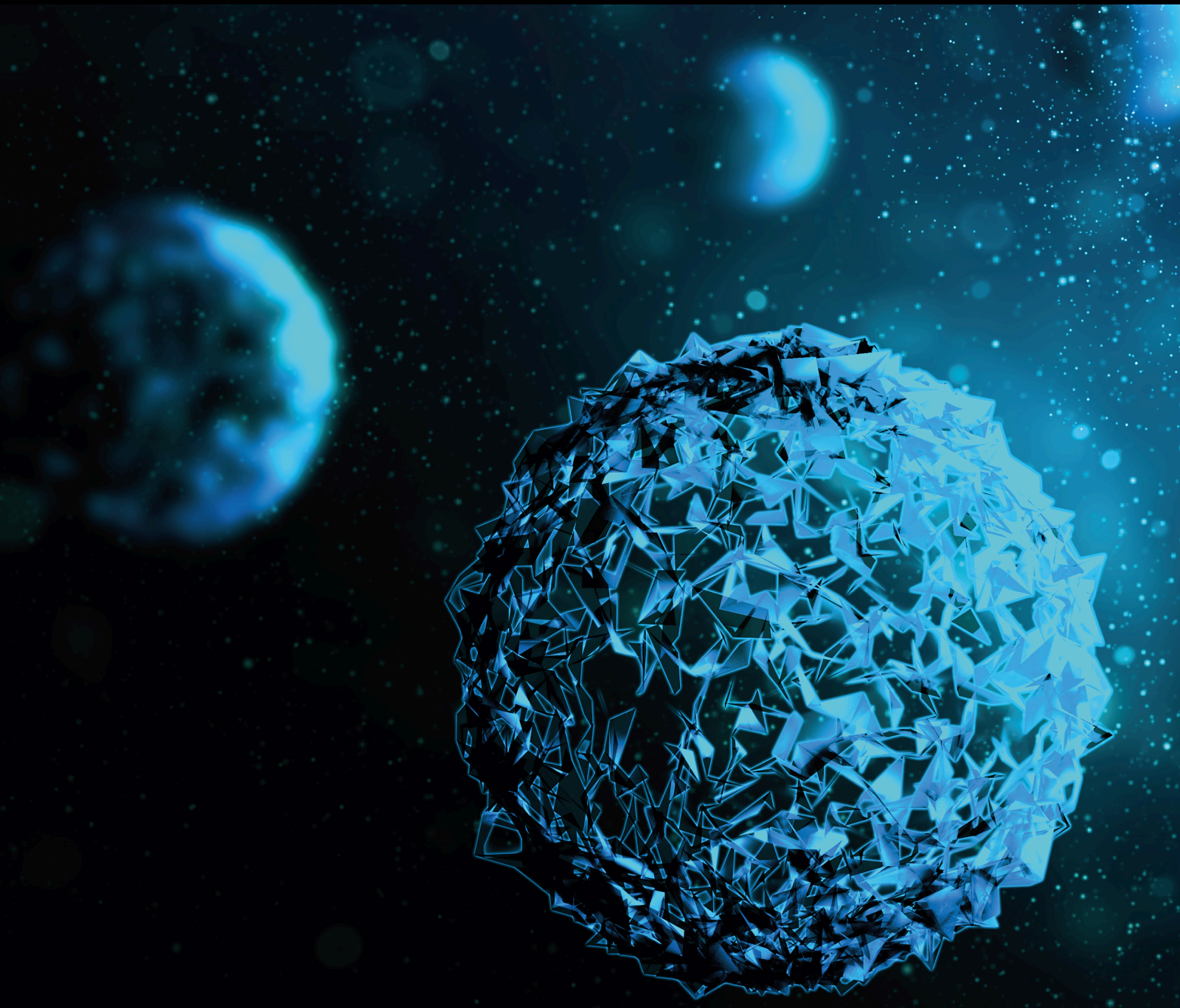


Animal Models of Human Pathology 2020

Special Issue Editor in Chief: Monica Fedele

Guest Editors: Oreste Gualillo and Andrea Vecchione





Animal Models of Human Pathology 2020

BioMed Research International

**Animal Models of Human Pathology
2020**

Special Issue Editor in Chief: Monica Fedele
Guest Editors: Oreste Gualillo and Andrea
Vecchione



Copyright © 2022 Hindawi Limited. All rights reserved.

This is a special issue published in "BioMed Research International." All articles are open access articles distributed under the Creative Commons Attribution License, which permits unrestricted use, distribution, and reproduction in any medium, provided the original work is properly cited.

Editorial Board



Atif A. Ahmed, USA
Shinichi Aishima, Japan
Valeria Barresi, Italy
EWA BIEN, Poland
Tarek A. Bismar, Canada
Rosario Caltabiano, Italy
Jin-Jer Chen, China
Chandu de Silva, Sri Lanka
Vasiliki Galani, Greece
Wan-Ming Hu, China
Genichiro Ishii, Japan
Glen Jickling, USA
Shigeru Kobayashi, Japan
Neeta Kumar, Switzerland
Kun Li, China
Mirella Marino, Italy
Satoshi Maruyama, Japan
Kathleen Montone, USA
Fazul Nabi, China
Yasuhiro Nakamura, Japan
Yukihiro Nakanishi, USA
Margaret A. Niznikiewicz, USA
Stefania Pizzimenti, Italy
Jianyu Y. Rao, USA
Takashi Saku, Japan
Claire Troakes, United Kingdom
Koichiro Wada, Japan
Nina Zidar, Slovenia

Contents










Animal Models of Human Pathology 2020

Monica Fedele , Oreste Gualillo , and Andrea Vecchione 
Editorial (2 pages), Article ID 9839314, Volume 2022 (2022)




Tetrandrine Ameliorates Myocardial Ischemia Reperfusion Injury through miR-202-5p/TRPV2

Wei Zhao, Youyang Wu, Fanhao Ye, Shiwei Huang, Hao Chen , Rui Zhou, and Wenbing Jiang 
Research Article (16 pages), Article ID 8870674, Volume 2021 (2021)


Development of Microsatellite Marker System to Determine the Genetic Diversity of Experimental Chicken, Duck, Goose, and Pigeon Populations

Xiulin Zhang , Yang He , Wei Zhang , Yining Wang , Xinmeng Liu , Aique Cui , Yidi Gong , Jing Lu, Xin Liu, Xueyun Huo, Jianyi Lv, Meng Guo, Xiaoyan Du, Lingxia Han, Hongyan Chen, Jilan Chen, Changlong Li , and Zhenwen Chen 
Research Article (14 pages), Article ID 8851888, Volume 2021 (2021)






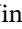



Coadministration of Ketamine and Perampanel Improves Behavioral Function and Reduces Inflammation in Acute Traumatic Brain Injury Mouse Model

Faleh Alqahtani , Mohammed A. Assiri, Mohamed Mohany, Imran Imran , Sana Javaid, Muhammad Fawad Rasool, Waleed Shakeel, Farzane Sivandzade, Ahmed Z. Alanazi, Salim S. Al-Rejaie , Musaad A. Alshammari, Fawaz Alasmari, Mohammed Mufadhe Alanazi, and Faisal F. Alamri
Research Article (12 pages), Article ID 3193725, Volume 2020 (2020)



Effect of Selenium on Expression of Apoptosis-Related Genes in Cryomedia of Mice Ovary after Vitrification

Reza Nori-Garavand, Maryam Hormozi, Leila Narimani, Nasim Beigi Boroujeni, Asghar Rajabzadeh, Leila Zarei, Masoud Beigi Boroujeni, and Mandana Beigi Boroujeni 
Research Article (8 pages), Article ID 5389731, Volume 2020 (2020)



A Modified Murine Calvarial Osteolysis Model Exposed to Ti Particles in Aseptic Loosening

Zhantao Deng , Shuai Wang , Mengyuan Li , Guangtao Fu, Chang Liu , Shuxian Li , Jiewen Jin , Feng-Juan Lyu , Yuanchen Ma , and Qiujian Zheng 
Research Article (7 pages), Article ID 3403489, Volume 2020 (2020)

Impact of Acute Pancreatic Injury on Sphingolipid Metabolism in the Salivary Glands

Małgorzata Żendzian-Piotrowska, Dominika M. Ziembicka, Bartłomiej Łukaszuk , and Krzysztof Kurek 
Research Article (7 pages), Article ID 6403482, Volume 2020 (2020)

Resveratrol Improves Hepatic Redox Status and Lipid Balance of Neonates with Intrauterine Growth Retardation in a Piglet Model

Kang Cheng, Shuli Ji, Peilu Jia, Hao Zhang, Ting Wang, Zhihua Song, Lili Zhang , and Tian Wang 
Research Article (12 pages), Article ID 7402645, Volume 2020 (2020)

Editorial

Animal Models of Human Pathology 2020

Monica Fedele ¹, Oreste Gualillo ², and Andrea Vecchione ³

¹Istituto di Endocrinologia ed Oncologia Sperimentale (IEOS)–CNR, 80131 Naples, Italy

²Santiago University Clinical Hospital IDIS (Instituto de Investigación Sanitaria de Santiago), 15706 Santiago de Compostela, Spain

³University of Rome “Sapienza”, Department of Clinical and Molecular Medicine, 00100 Rome, Italy

Correspondence should be addressed to Monica Fedele; mfedele@unina.it

Received 6 December 2021; Accepted 6 December 2021; Published 22 January 2022

Copyright © 2022 Monica Fedele et al. This is an open access article distributed under the Creative Commons Attribution License, which permits unrestricted use, distribution, and reproduction in any medium, provided the original work is properly cited.

Studying *in vivo* the effects of new therapeutic approaches and compounds is necessary after *in vitro* research and before clinical trials. To this aim, animal models play an essential role in providing preclinical validation for efficacy and toxicity testing.

In this frame, during 2020, animal models have been vital for the current global health priority of coronavirus disease 2019 caused by severe acute respiratory syndrome coronavirus 2 (SARS-CoV-2). Indeed, neutralizing monoclonal antibodies derived from convalescence donors have been tested in Syrian hamsters to demonstrate their *in vivo* protective efficacy, opening the avenue to their use as one of the significant medical countermeasures against SARS-CoV-2 [1]. Furthermore, transgenic mice that express human angiotensin-converting enzyme 2 (ACE2) have been generated and successfully employed to test the effects of SARS-CoV-2 infection and study its pathogenicity [2].

Although animal models may show certain discrepancies with human pathophysiology, due to their great potential to resemble the complexity of the human body, well-established animal models can also represent invaluable models for the discovery of novel pathophysiological mechanisms of human disease. To cite just one example, recent evidence, performed in an experimental arthritis model used for more than 50 years, has shown that arthritis promotes a central catabolic state that can be targeted and reversed by activation of hypothalamic AMPK [3]. This might open new therapeutic alternatives to treat rheumatoid arthritis- (RA-) associated metabolic comorbidities, improving RA-patients overall prognosis.

Animal models have also represented an irreplaceable ally in outstanding research studies of the last years in the

fight against cancer. Xu et al., using orthotopic tumor models in mice, demonstrated the efficacy of new personalized nano vaccines based on fluoropolymers for postsurgical cancer immunotherapy [4]. More recently, subcutaneous triple-negative breast cancer xenograft mouse models have been employed to demonstrate *in vivo* tumor targeting and antitumor efficacy of aptamer-conjugated nanovectors, capable of delivering cisplatin specifically to tumor cells [5].

In this special issue, we collected some other interesting investigations on human pathologies that have been modeled in animals to get insight into their pathogenesis and therapy. Among them, using ischemia-reperfusion rats, Żendzian-Piotrowska et al. [6] demonstrated that Tetrandrine might reduce myocardial injury by targeting the miR-202-5p/TRPV2 axis. Zhao et al. [7] used well-established rat models of cerulein-induced acute pancreatitis and streptozotocin-induced diabetes to study and compare their effect on sphingolipid metabolism in the salivary glands. The traumatic brain injury (TBI) mouse model induced by the weight-drop method was used in the study by Alqahtani et al. [8] to demonstrate the coadministration of ketamine and perampanel can reduce inflammation and, consequently, improve the behavioral function of patients with TBI. Still, in mice, Nori-Garavand et al. [9] demonstrated the positive effects of selenium on suppression of apoptosis during the vitrification-thawing process of the ovary, which is used for the preservation of fertility in humans. A piglet model was instead used by Cheng et al. [10] to demonstrate that the treatment with oral administration of resveratrol plays a beneficial role in hepatic oxidative stress and lipid balance of neonatal fatty liver diseases associated with intrauterine growth retardation.

Further studies are required to develop clinically relevant acute and chronic animal models which reflect the clinical reality of the various factors and situations that influence the biological processes of humans (age, disease, comorbidities, and gender). The closer the model is to humans, the faster it opens the door to personalized therapies.

Conflicts of Interest

The editors declare that they have no conflicts of interest regarding the publication of this special issue.

Authors' Contributions

All authors researched data for the article, made substantial contributions to discussions of the content, and contributed to writing, reviewing, and/or editing the manuscript before submission.

Acknowledgments

We thank the invaluable effort of the expert reviewers for their critical evaluation of the submitted manuscripts and all the authors who have contributed their work to this special issue. O.G. is a staff personnel (I3SNS Stable Researcher) of Xunta de Galicia (Servizo Galego de Saude (SERGAS)) through a research-staff contract (Instituto de Salud Carlos III (ISCIII)/SERGAS). O.G. is member of the RETICS Programme, RD16/0012/0014 (RIER: Red de Investigación en Inflamación y Enfermedades Reumáticas) and RICORS Programme, RD21/0002/0025 via ISCIII and FEDER. The work of O.G. (PI17/00409 and PI20/00902), is funded by ISCIII and FEDER. O.G. is a beneficiary of a project funded by the Research Executive Agency of the European Union in the framework of MSCA-RISE Action of the H2020 Programme (project number 734899). O.G. is the beneficiary of a grant funded by Xunta de Galicia, Consellería de Educación, Universidade e Formación Profesional and Consellería de Economía, Emprego e Industria (GAIN) (GPC IN607B2019/10).

Monica Fedele
Oreste Gualillo
Andrea Vecchione

References

- [1] T. F. Rogers, F. Zhao, D. Huang et al., "Isolation of potent SARS-CoV-2 neutralizing antibodies and protection from disease in a small animal model," *Science*, vol. 369, no. 6506, pp. 956–963, 2020.
- [2] L. Bao, W. Deng, B. Huang et al., "The pathogenicity of SARS-CoV-2 in hACE2 transgenic mice," *Nature*, vol. 583, no. 7818, pp. 830–833, 2020.
- [3] P. Seoane-Collazo, E. Rial-Pensado, Á. Estévez-Salguero et al., "Activation of hypothalamic AMPK ameliorates metabolic complications of experimental arthritis," *Arthritis and rheumatology*, 2021.
- [4] J. Xu, J. Lv, Q. Zhuang et al., "A general strategy towards personalized nanovaccines based on fluoropolymers for post-surgical cancer immunotherapy," *Nature Nanotechnology*, vol. 15, no. 12, pp. 1043–1052, 2020.
- [5] L. Agnello, S. Tortorella, A. d'Argenio et al., "Optimizing cisplatin delivery to triple-negative breast cancer through novel EGFR aptamer-conjugated polymeric nanovectors," *Journal of Experimental Clinical Cancer Research*, vol. 40, no. 1, p. 239, 2021.
- [6] M. Zendzian-Piotrowska, D. M. Ziembicka, B. Łukaszuk, and K. Kurek, "Impact of acute pancreatic injury on sphingolipid metabolism in the salivary glands," *BioMed Research International*, vol. 2020, Article ID 6403482, 7 pages, 2020.
- [7] W. Zhao, Y. Wu, F. Ye et al., "Tetrandrine ameliorates myocardial ischemia reperfusion injury through miR-202-5p/TRPV2," *BioMed Research International*, vol. 2021, Article ID 8870674, 16 pages, 2021.
- [8] F. Alqahtani, M. A. Assiri, M. Mohany et al., "Coadministration of ketamine and perampanel improves behavioral function and reduces inflammation in acute traumatic brain injury mouse model," *BioMed Research International*, vol. 2020, Article ID 3193725, 12 pages, 2020.
- [9] R. Nori-Garavand, M. Hormozi, L. Narimani et al., "Effect of selenium on expression of apoptosis-related genes in cryome-dia of mice ovary after vitrification," *BioMed Research International*, vol. 2020, Article ID 5389731, 8 pages, 2020.
- [10] K. Cheng, J. Hu, H. Chen, L. Wu, J. Liao, and L. Cheng, "Effects of different methods of air disinfection of computed tomography rooms dedicated to COVID-19 cases," *BioMed Research International*, vol. 2020, Article ID 7402645, 5 pages, 2020.

Research Article

Tetrandrine Ameliorates Myocardial Ischemia Reperfusion Injury through miR-202-5p/TRPV2

Wei Zhao, Youyang Wu, Fanhao Ye, Shiwei Huang, Hao Chen , Rui Zhou, and Wenbing Jiang 

Department of Cardiology, The Third Clinical Institute Affiliated to Wenzhou Medical University, Wenzhou, 325000 Zhejiang, China

Correspondence should be addressed to Wenbing Jiang; jiangwenbing163126@163.com

Received 6 September 2020; Revised 5 February 2021; Accepted 23 February 2021; Published 9 March 2021

Academic Editor: Monica Fedele

Copyright © 2021 Wei Zhao et al. This is an open access article distributed under the Creative Commons Attribution License, which permits unrestricted use, distribution, and reproduction in any medium, provided the original work is properly cited.

Objective. This study is aimed at investigating the therapeutic effects of tetrandrine (Tet) on myocardial ischemia reperfusion (I/R) injury and probe into underlying molecular mechanism. **Methods.** H9C2 cells were divided into hypoxia/oxygenation (H/R) group, H/R+Tet group, H/R+Tet+negative control (NC) group, and H/R+Tet+miR-202-5p inhibitor group. RT-qPCR was utilized to monitor miR-202-5p and TRPV2 expression, and TRPV2 protein expression was detected via western blot and immunohistochemistry in H9C2 cells. Cardiomyocyte apoptosis was evaluated through detection of apoptosis-related markers and flow cytometry. Furthermore, myocardial enzyme levels were detected by ELISA. Rats were randomly separated into sham operation group, I/R group, I/R+Tet group (50 mg/kg), I/R+Tet+NC group, and I/R+Tet+miR-202-5p inhibitor group. miR-202-5p and TRPV2 mRNA expression was assessed by RT-qPCR. TRPV2 protein expression was detected through western blot and immunohistochemistry in myocardial tissues. Apoptotic levels were assessed via apoptosis-related proteins and TUNEL. Pathological changes were observed by H&E staining. Myocardial infarction size was examined by Evans blue-TCC staining. **Results.** Abnormally expressed miR-202-5p as well as TRPV2 was found in H/R H9C2 cells and myocardial tissues of I/R rats, which was ameliorated following Tet treatment. Tet treatment significantly suppressed H/R- or I/R-induced cardiomyocyte apoptosis. ELISA results showed that CK-MB and LDH levels were lowered by Tet treatment in H/R H9C2 cells and serum of I/R rats. H&E staining indicated that Tet reduced myocardial injury in I/R rats. Also, myocardial infarction size was lowered by Tet treatment. The treatment effects of Tet were altered following cotreatment with miR-202-5p inhibitor. **Conclusion.** Our findings revealed that Tet may ameliorate myocardial I/R damage via targeting the miR-202-5p/TRPV2 axis.

1. Introduction

Myocardial ischemia/reperfusion (I/R) is a process when the blood reperfusion caused by the recovery of blood flow after myocardial tissue ischemia, which could aggravate myocardial damage and dysfunction, thereby leading to myocardial infarction and even heart failure [1–3]. I/R injury can induce cell apoptosis and increase in infarct area. It has been a key factor that affects the treatment effect of acute myocardial infarction [4]. Therefore, it is of importance to explore novel treatment strategies to improve myocardial I/R damage.

MicroRNA (miRNA) is a membrane of the noncoding RNA family, with about 21 nucleotides in length [5]. miR-

NAs usually target multiple genes. Myocardial I/R injury involves various miRNAs [6]. It has been emphasized that miRNAs mediate the regulation of I/R-induced myocardial damage and dysfunction, which may be myocardial ischemic disease as a potential therapeutic target [7]. As a member of the miRNA family, miR-202-5p may participate in regulating the progression of various cancers. For example, it is related to breast cancer cell resistance to Adriamycin [8]. Furthermore, it may mediate biological behaviors of thyroid carcinoma cells [9]. Recently, the protective function of miR-202-5p against myocardial I/R damage has been reported via Transient Receptor Potential Cation Channel Subfamily V Member 2 (TRPV2) [10]. Ca^{2+} overload as well as

mitochondrial dysfunction has been found to be stimulating factors for myocardial I/R injury [11]. TRPV2 is a family membrane of TRPV channel within and around the cardiovascular system [12]. Under pathological conditions, TRPV2 mediates abnormal Ca^{2+} , thereby accelerating the progression of diseases [13]. It has been considered as a therapeutic target for cardiovascular diseases [14–16].

Tetrandrine (Tet) is a bisbenzylisoquinoline alkaloid extracted from *Stephania tetrandra* S. Moore plant [17]. Tet possesses a variety of pharmacological effects such as anti-cancer [18], anti-inflammation [19], and antioxidant stress [20]. Excessive apoptosis of cardiomyocytes is also the main cause of myocardial I/R damage [21]. Therefore, antiapoptosis therapy could reduce I/R injury and ameliorate cardiac dysfunction [22]. Cellular and animal experiments have demonstrated that Tet is effective for treatment of cardiovascular diseases [23]. However, it remains unclear concerning the effects and underlying molecular mechanism of Tet on myocardial I/R injury. Thus, a myocardial I/R injury model was constructed at the cellular and animal levels. We observed the therapeutic effect of Tet on myocardial I/R damage and explored its molecular mechanism. Our findings revealed that Tet could be a new therapeutic drug for myocardial I/R damage.

2. Materials and Methods

2.1. Cell Culture. H9C2 cells were grown in the Dulbecco's modified Eagle medium (SH30243.01B; Hyclone, Beijing, China) containing 10% fetal bovine serum (SH30084.03; Hyclone) at 37°C and 5% CO₂ saturated humidity. These cells were separated into four groups: control group (without any treatment), hypoxia/oxygenation (H/R) group (hypoxia (120 min, 95% N₂/5% CO₂) and reoxygenation (30 min, 95% O₂/5% CO₂)), H/R+tetrandrine (Tet) group (H9C2 cells were exposed to H/R, followed by treatment with 1.5 μmol/L Tet for 48 h), H/R+Tet+negative control (NC) group (H9C2 cells were exposed to H/R, treated with 1.5 μmol/L Tet for 48 h, and transfected NC via Lipofectamine 2000 for 48 h), and H/R+Tet+miR-202-5p inhibitor group (H9C2 cells were exposed to H/R, treated with 1.5 μmol/L Tet for 48 h, and transfected miR-202-5p inhibitor via Lipofectamine 2000 for 48 h).

2.2. Real-Time Quantitative PCR (RT-qPCR). Takara minibeat universal RNA extraction kit (9767; Takara) was utilized to extract total RNA from tissues or cells. 1 μL RNA was measured at OD260 and OD280 with a UV spectrophotometer. According to the OD260/OD280 ratio, the RNA quality was estimated. Then, the total RNA was stored at -80°C. Then, reverse transcription was presented in the following reverse transcription system: 1 μL PrimeScript enzyme mix, 1 μL RT primer mix, 4 μL 5x PrimeScript buffer, 3.1574 μg RNA, and up to 20 μL RNase-free H₂O. Primer sequences were as follows: TRPV2: 5'-CGACGGGCTTCTACAA ATGG-3' (forward), 5'-AGGACCGTAACACCACTCAG-3' (reverse); GAPDH: 5'-ACTCCATTCTTCCACCTT TG-3' (forward), 5'-CCCTGTTGCTGTAGCCATATT-3'

(reverse); miR-202-5p: 5'-TGCGCTTCCTATGCATATA CT-3' (forward), 5'-CAGTGGGTGTCGTGGAGT-3' (reverse); and U6: 5'-GCTTCGGCAGCACATATACTA AAAT-3' (forward), 5'-CGCTTCACGAATTTGCGGTGC AT-3' (reverse). The reverse transcription reaction procedure was as follows: 37°C for 15 min, 85°C for 5 s and 4°C hold. RT-qPCR was utilized to quantify the mRNA expression of target genes by ABI 12K fluorescence RT-qPCR instrument (ABI, USA).

2.3. Cell Counting Kit-8 (CCK-8) Assay. Cell viability was determined utilizing CCK-8 detection kit (Dojindo, Shanghai, China). The cells in each group were seeded onto 96-well plates. Each well was treated with 10 μL CCK-8 solution at 37°C for 3-4 h. After adding 10 μL stop solution to each well, the OD450 value was determined with a microplate reader.

2.4. Flow Cytometry Assay. Cells were plated at 6-well plates (3 × 10⁵ cells/well) overnight. After different treatments, the cells were harvested. Apoptotic levels were assessed by apoptosis detection kit (Vazyme, Nanjing, China). After centrifugation, 100 μL Annexin Binding Buffer was used to resuspend the cells. The cells were, respectively, processed by 5 μL Annexin FITC and 5 μL PI at room temperature in the dark for 15 min. After adding 150 μL Annexin Binding Buffer, apoptosis was detected using a flow cytometer (Cytometer FLEX S; Beckman, USA).

2.5. Western Blot. Tissues or cells were lysed by RIPA lysis buffer (P0013B; Beyotime, Beijing) on ice for 30 min. Following ultrasound in an ice bath for 3 min and centrifugation at 12000 rpm at 4°C for 10 min, the supernatant was transferred to a new EP tube. Using the BCA protein quantitative detection kit (P0009; Beyotime), the protein concentration was determined. The protein sample was separated through a polyacrylamide gel. After transferring the membrane, the sample was sealed in a 5% milk/TBST room at temperature for 1 h. The PVDF membrane was cocultured with the primary antibodies against TRPV2 (1 : 1000; BS-10297R; Bioss, Beijing), caspase3 (1:1000; AF7022; AFFINITY, Beijing), pro-caspase3 (1:3000; 19677-1-AP; Proteintech, Wuhan, China), Bax (1:3000; 60267-1-Ig; Proteintech), Bcl-2 (1:3000; 12789-1-AP; Proteintech), and GAPDH (60004-1-Ig; Proteintech) overnight at 4°C. Afterwards, the membrane was cocultured with the secondary antibody labeled with horseradish peroxidase (1:5000; SA00001-2; Proteintech) for 1 h at room temperature. The enhanced luminol reagent and oxidizing reagent were added to the membrane. After that, the membrane was colored by luminescent reagent 1.5 min. The results were observed with the gel imaging system.

2.6. ELISA. LDH and CK-MD levels were detected in cell culture fluid and serum samples by lactate dehydrogenase (LDH) detection kit (A020-2; Jiancheng, Nanjing, China) and creatine kinetic acid MD isoenzyme (CK-MB) detection kit (E0061-1; Jiancheng) in line with the manufacturer's instructions.

2.7. Animals. Totally, 25 male Sprague-Dawley rats with 220-250 g were purchased from Hangzhou Scientific Cloud Biotechnology Co., Ltd. (China). They were routinely housed in the Animal Experimental Center for 1 week. This study gained the approval of the Ethics Committee of The Third Clinical Institute Affiliated to Wenzhou Medical University (2018038). Experiments were presented in line with the recommendations in the Guide for the Care and Use of Laboratory Animals of the National Institutes of Health. All animals were randomly separated into five groups: sham operation (control) group, myocardial I/R group, I/R+Tet group (50 mg/kg), I/R+Tet+NC group, and I/R+Tet+miR-202-5p inhibitor group. After intraperitoneal injection of 1% sodium pentobarbital (40 mg/kg) to anesthetize the rats, the chest was opened and the left anterior descending (LAD) coronary artery was ligated for 30 min and then perfused for 120 min. The sternotomy was performed to expose the heart, followed by occlusion of the distal third of the coronary artery for 30 min through tightening the ligature. When cyanosis and protrusions occurred in the ischemic myocardium wall, the occurrence of ischemia was confirmed. The ligature was then removed, and the occluded coronary artery was reperfused for 120 min. In time of this period, the ECG confirmed that the ST segment recovered over 50%. Rats in the sham operation group received an open chest but did not ligate the coronary arteries. I/R rats were injected 50 mg/kg Tet through the tail vein after reperfusion. Rats in the sham operation group were injected with the same volume of saline. In the rats injected with Tet, miR-202-5p inhibitor or NC was injected through the tail vein 48 h until ligation of the LAD coronary artery. The rats were euthanized. Then, heart tissues and abdominal aorta blood were harvested. Tissues were fixed by 4% paraformaldehyde (E672002; Sangon Biotech, Shanghai, China).

2.8. Hematoxylin-Eosin (H&E) and Evans Blue-TCC Staining. After deparaffinization and hydration, the paraffin sections were separately stained by hematoxylin (Proteintech) as well as eosin (sigma, USA) for 3 min. Following mounting with neutral gum, images were taken under an optical microscope (OLYMPUS BX53; Olympus, Japan). Evans blue dye (Solarbio, Beijing, China) was injected into the aorta and coronary arteries to demarcate the ischemic risk or unstained areas of the heart. Following cutting the whole heart into five slices transversely, the slices were stained with 2% (*w/v*) triphenyltetrazolium chloride (TTC; T8877-25G; Sigma) at 37°C for 15 min. Image analysis software was used to quantify the infarct volume, risk area volume, and total heart volume. The percentage of infarct volume (%) was calculated by comparing to the whole heart.

2.9. Transferase-Mediated dUTP Nick End Labeling (TUNEL) Staining. Apoptotic levels were evaluated utilizing TUNEL apoptosis detection kit (ATK00001; AtaGenix, Wuhan). 10 U/mL DNase I and 1x DNase I Buffer were added in the positive control group, and 1x DNase I Buffer was added in the NC group. The sections were incubated with TUNEL detection solution in the dark for 60 min. Then, the sections were treated with 0.05 µg/µL DAPI solution for 10 min at

room temperature and dark. Antifluorescence quenching mounting tablets were used for mounting. Pictures were taken under a fluorescence microscope (BX53; Olympus, Japan). By Image-Pro® Plus (IPP) software, 3 nonrepetitive and nonoverlapping visual fields were randomly chosen. The integrated optical density (IOD) values and areas for each field were determined. The average and standard deviation were calculated for statistical analysis.

2.10. Immunohistochemistry. Briefly, the sections were blocked with goat serum (C0265; Beyotime) at room temperature for 30 min. The sections were cotreated with primary antibody against TRPV2 (1:100; BS-10297R; Bioss) overnight at 4°C. Horseradish peroxidase-labeled anti-mouse IgG antibodies (ATPA00025Go; AtaGenix, Wuhan) were added to the sections and cultured at room temperature for 30 min. Then, the sections were colored by DAB for 5-10 min. Nuclei were counterstained with hematoxylin (B600020; Proteintech) for 3-5 min. After dehydration and transparency, the sections were sealed with neutral gum.

2.11. Statistical Analysis. All statistical analysis was presented through GraphPad Prism 7.0. Data were presented as the mean ± standard deviation. The differences between ≥3 groups were compared via one-way analysis of variance. *p* value < 0.05 was considered statistically significant.

3. Results

3.1. Tet Ameliorates the miR-202-5p/TRPV2 Axis in H/R-Treated H9C2 Cells. In the H/R-treated H9C2 cells, miR-202-5p expression was detected to be decreased in comparison to controls (Figure 1(a)), consistent with a previous study [10]. Tet treatment distinctly ameliorated H/R-induced suppression of miR-202-5p level, which was reversed after cotransfection with miR-202-5p inhibitor. The transfection effects of miR-202-5p inhibitor were assessed in H9C2 cells by RT-qPCR. The data confirmed that miR-202-5p expression was distinctly suppressed after transfection of its inhibitor compared controls (Figure 1(b)). As a previous study, TRPV2 has been identified as a direct target of miR-202-5p in rat cardiomyocytes [10]. Herein, we also found that the expression of TRPV2 protein was significantly lowered following transfection with miR-202-5p inhibitor in H9C2 cells (Figures 1(c) and 1(d)). In Figure 1(e), TRPV2 mRNA had a higher expression in H/R-induced H9C2 cells than controls. Its mRNA expression was suppressed in H/R H9C2 cells after treatment with Tet. However, miR-202-5p inhibitor could reverse the decrease in TRPV2 mRNA expression induced by Tet in H/R H9C2 cells. Furthermore, we examined the expression of TRPV2 protein through western blot. Similar to the RT-qPCR results, TRPV2 protein exhibited a distinctly higher expression in H/R H9C2 cells compared with controls (Figures 1(f) and 1(g)). Following treatment with Tet, its expression was prominently lowered in H/R-induced H9C2 cells, which was elevated through cotransfection with miR-202-5p inhibitor. Thus, Tet treatment could ameliorate the miR-202-5p/TRPV2 axis in H/R-induced H9C2 cells.

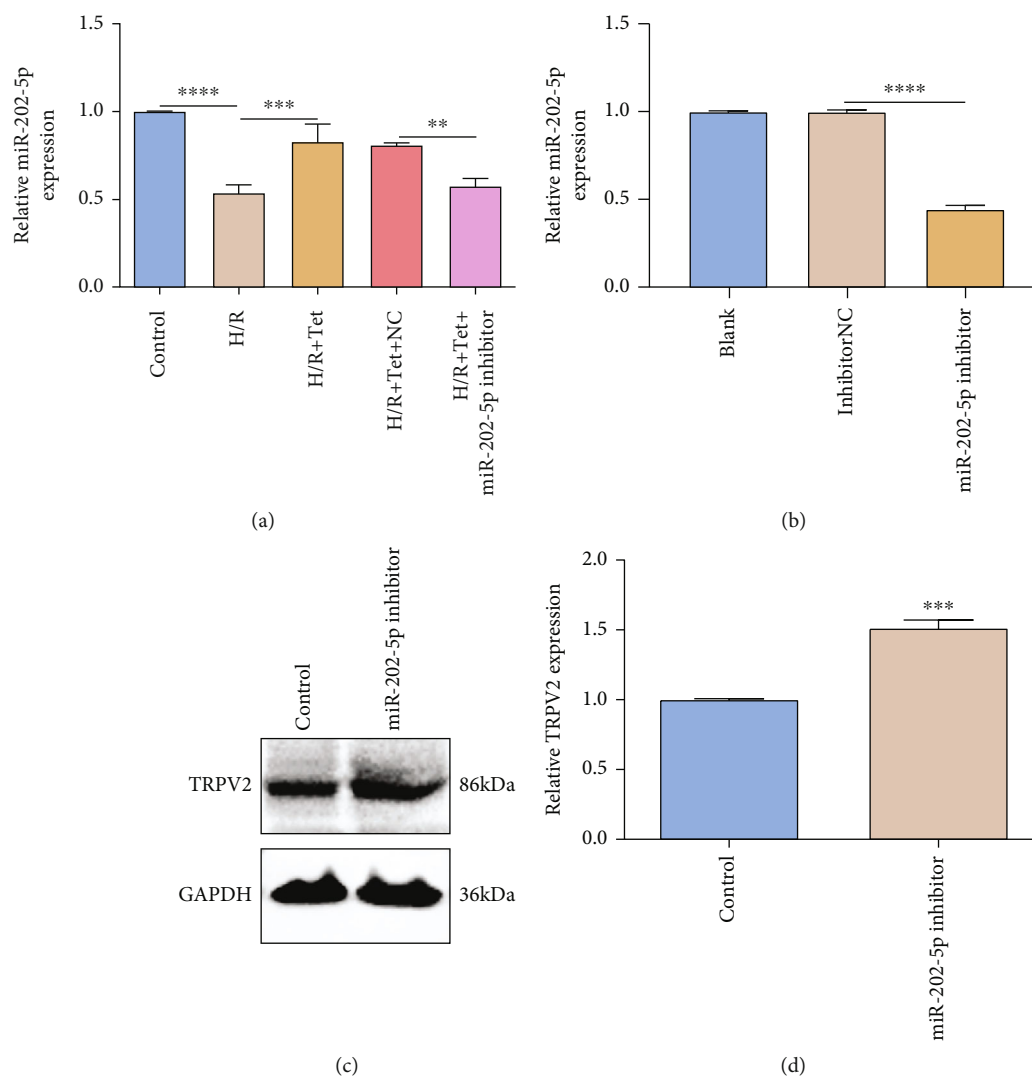


FIGURE 1: Continued.

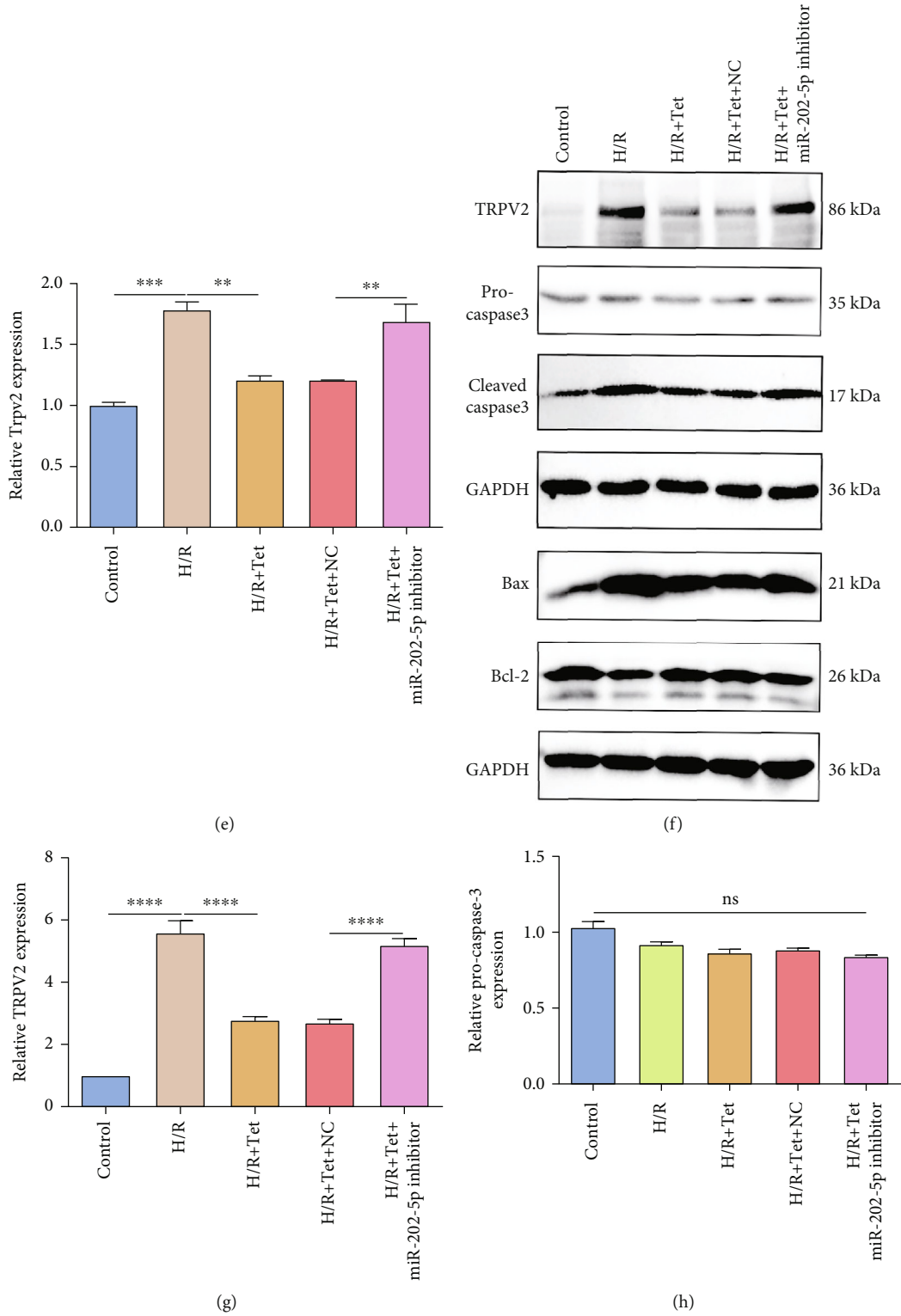


FIGURE 1: Continued.

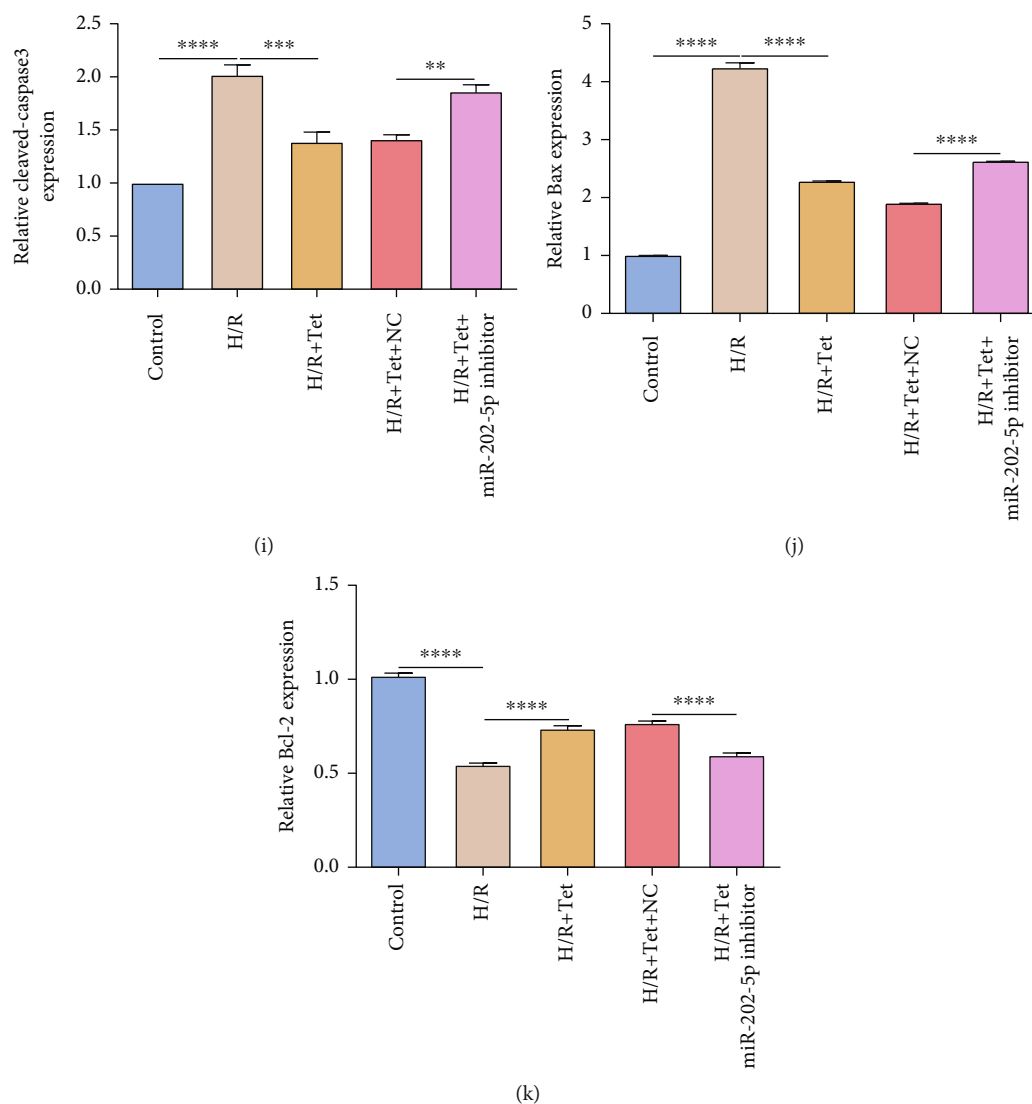


FIGURE 1: Tet ameliorates the miR-202-5p/TRPV2 axis in H/R H9C2 cells. (a) RT-qPCR detecting the expression of miR-202-5p in H/R H9C2 cells treated with Tet and/or miR-202-5p inhibitor. (b) The transfection of miR-202-5p inhibitor was evaluated in H9C2 cells by RT-qPCR. (c, d) Western blot showing the protein expression of TRPV2 in H9C2 cells transfected with miR-202-5p inhibitor. (e) RT-qPCR detecting the mRNA expression of TRPV2 in H/R H9C2 cells treated with Tet and/or miR-202-5p inhibitor. (f-k) Western blot showing the protein expression of TRPV2, pro-caspase3, cleaved caspase3, Bax, and Bcl-2 in H/R H9C2 cells treated with Tet and/or miR-202-5p inhibitor. ns: not significant; ** $p < 0.01$; *** $p < 0.001$; **** $p < 0.0001$.

3.2. Tet Treatment Suppresses H/R-Induced Apoptosis in H9C2 Cells through miR-202-5p. We further observed whether Tet treatment could ameliorate H/R-induced apoptosis in H9C2 cells through miR-202-5p. The expression of apoptosis-related markers including pro-caspase3, cleaved caspase3, Bax, and Bcl-2 was examined by western blot. There was no significant difference in pro-caspase3 expression in these groups (Figures 1(f) and 1(h)). The expression of cleaved caspase3 (Figures 1(f) and 1(i)) and Bax (Figures 1(f) and 1(j)) was both markedly elevated in H/R H9C2 cells, which was improved by Tet treatment. With cotreatment with Tet and miR-202-5p inhibitor, cleaved caspase3 and Bax expression was distinctly higher in H/R H9C2 cells in comparison to those with Tet treatment. In Figures 1(f) and 1(k), Bcl-2 expres-

sion was significantly decreased in H/R H9C2 cells than controls, which was ameliorated by Tet treatment. However, miR-202-5p inhibitor weakened the treatment effects of Tet on Bcl-2 expression in H/R H9C2 cells. Apoptotic levels of H9C2 cells were also evaluated via flow cytometry. Apoptosis levels of H/R cells were significantly increased in comparison to controls (Figures 2(a) and 2(b)). Tet treatment could ameliorate H/R-induced apoptosis in H9C2 cells, which was reversed after cotreatment with miR-202-5p inhibitor. As depicted in CCK-8 assay results, the cell viability was significantly lowered in H/R-induced H9C2 cells than controls (Figure 2(c)). Tet treatment improved proliferation of H/R cells. Nevertheless, following cotreatment with miR-202-5p inhibitor and Tet, the proliferative capacity of H/R cells was distinctly

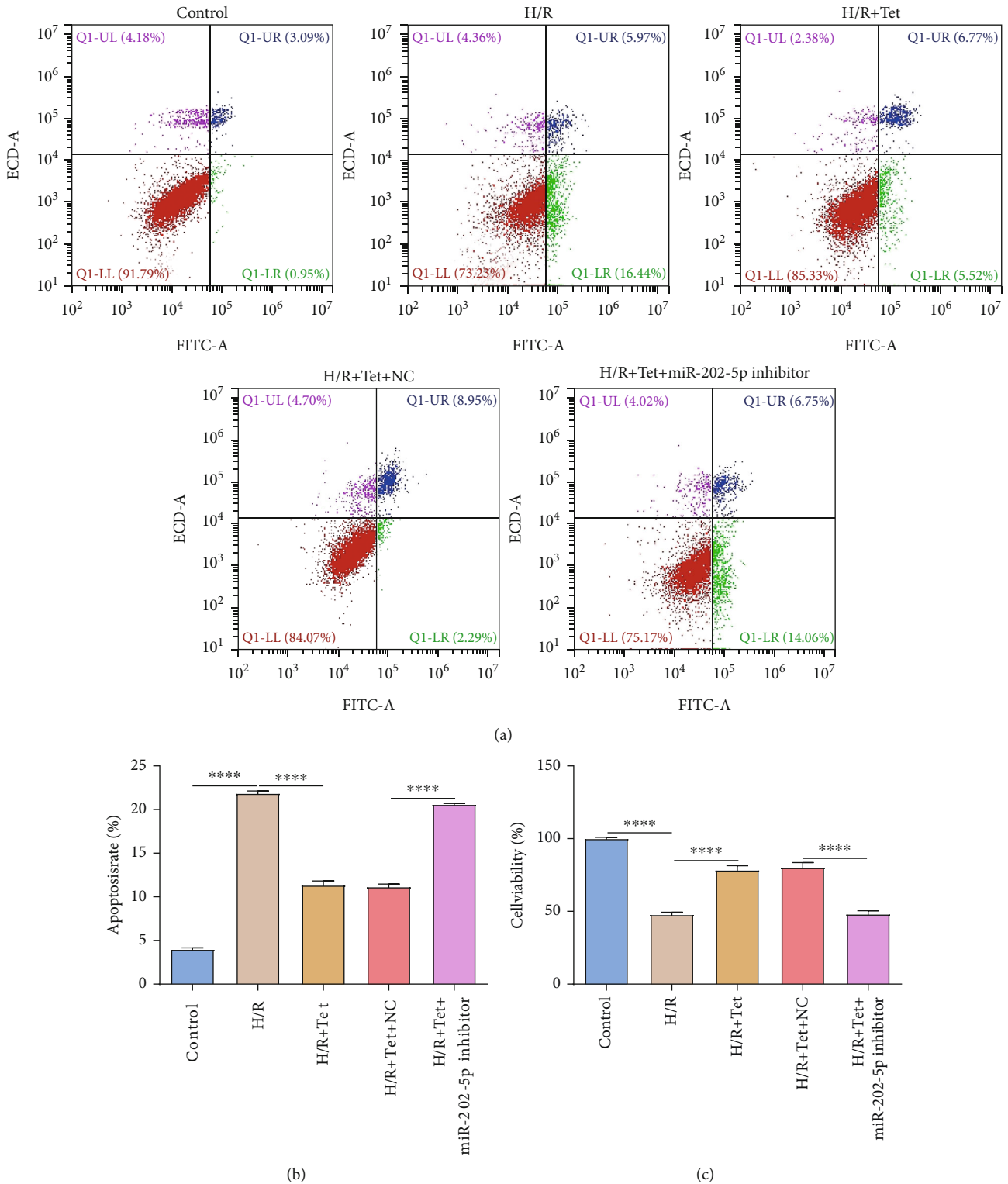


FIGURE 2: Tet treatment inhibits H/R-induced cardiomyocyte apoptosis through miR-202-5p. (a) Representative images of flow cytometry results. (b) Quantitative results of apoptosis levels for H/R H9C2 cells treated with Tet and/or miR-202-5p inhibitor. (c) CCK-8 assay was presented to assess the cell viability of H/R H9C2 cells treated with Tet and/or miR-202-5p inhibitor. **** $p < 0.0001$.

decreased (Figure 2(c)). Thus, Tet treatment could suppress H/R-induced cardiomyocyte apoptosis, which could be partly related to miR-202-5p.

3.3. *Tet Ameliorates the miR-202-5p/TRPV2 Pathway in Myocardial Tissues of I/R Rats.* RT-qPCR results exhibited that miR-202-5p had a lower expression in myocardial

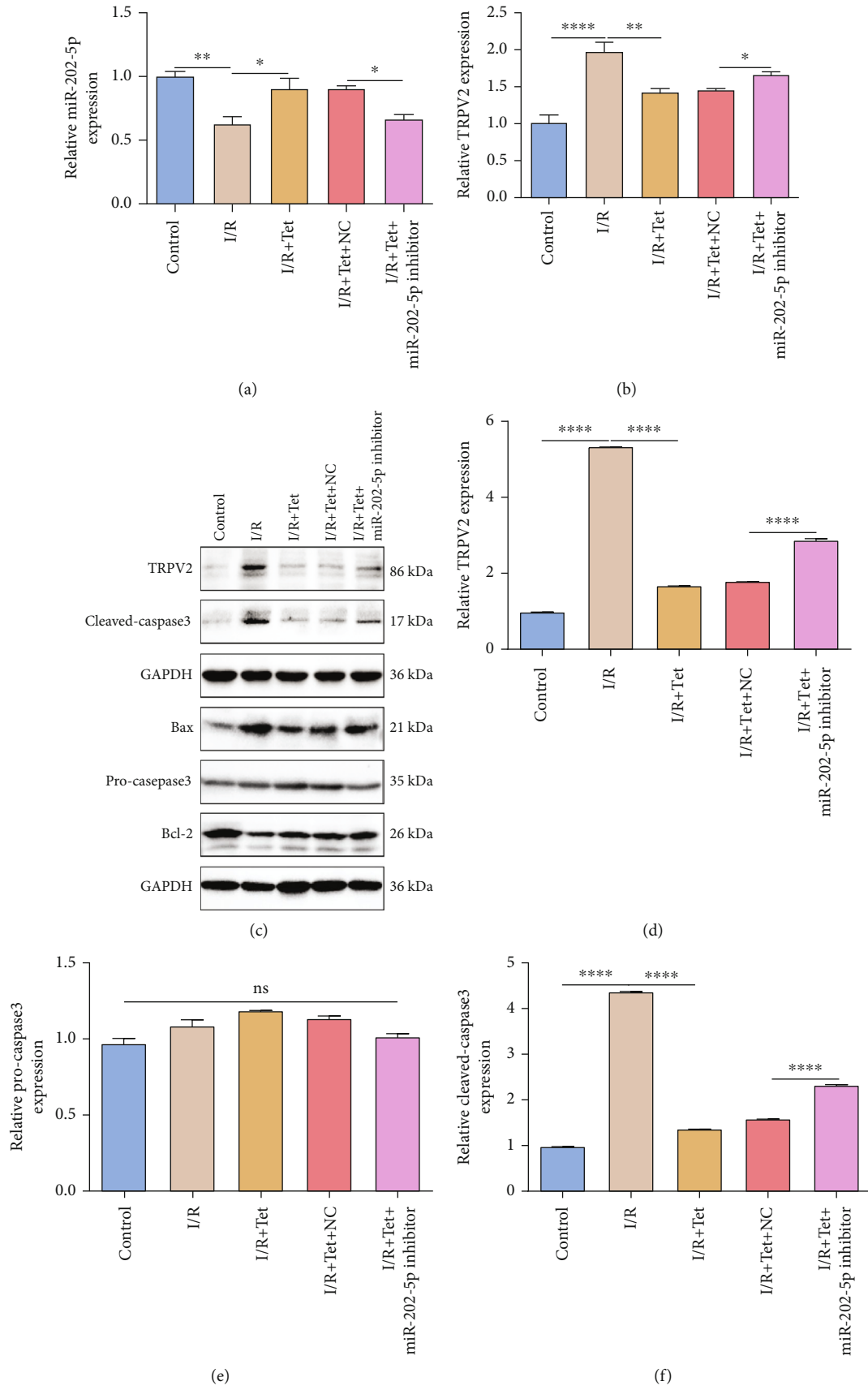


FIGURE 3: Continued.

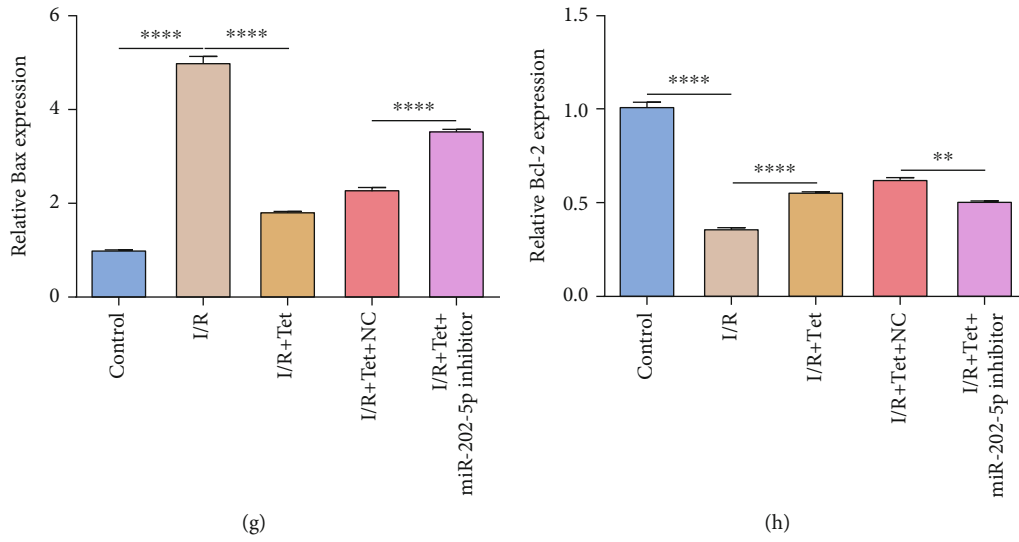


FIGURE 3: Tet ameliorates the miR-202-5p/TRPV2 pathway in myocardial tissues of I/R rats. (a, b) RT-qPCR examining the expression of miR-202-5p as well as TRPV2 in I/R rats treated with Tet and/or miR-202-5p inhibitor. (c-h) Western blot detecting the protein expression of TRPV2, pro-caspase3, cleaved caspase3, Bax, and Bcl-2 in I/R rats treated with Tet and/or miR-202-5p inhibitor. * $p < 0.05$; ** $p < 0.01$; **** $p < 0.0001$.

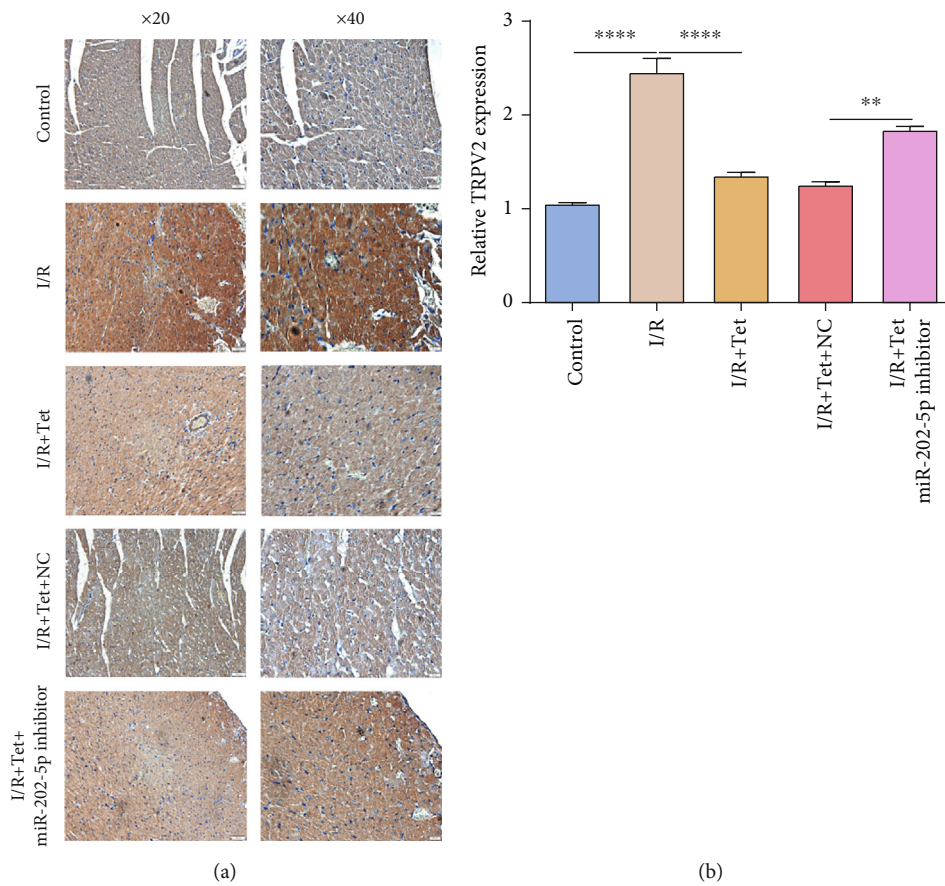


FIGURE 4: Tet decreases TRPV2 expression in I/R rats via increasing miR-202-5p. (a) Representative images of immunohistochemistry results for TRPV2 protein in I/R myocardial tissues treated with Tet and/or miR-202-5p inhibitor. Scar bar: 50 and 20 μm . Magnification: $\times 20$ and $\times 40$. (b) The expression of TRPV2 protein was quantified in myocardial tissues of each group. ** $p < 0.01$; **** $p < 0.0001$.

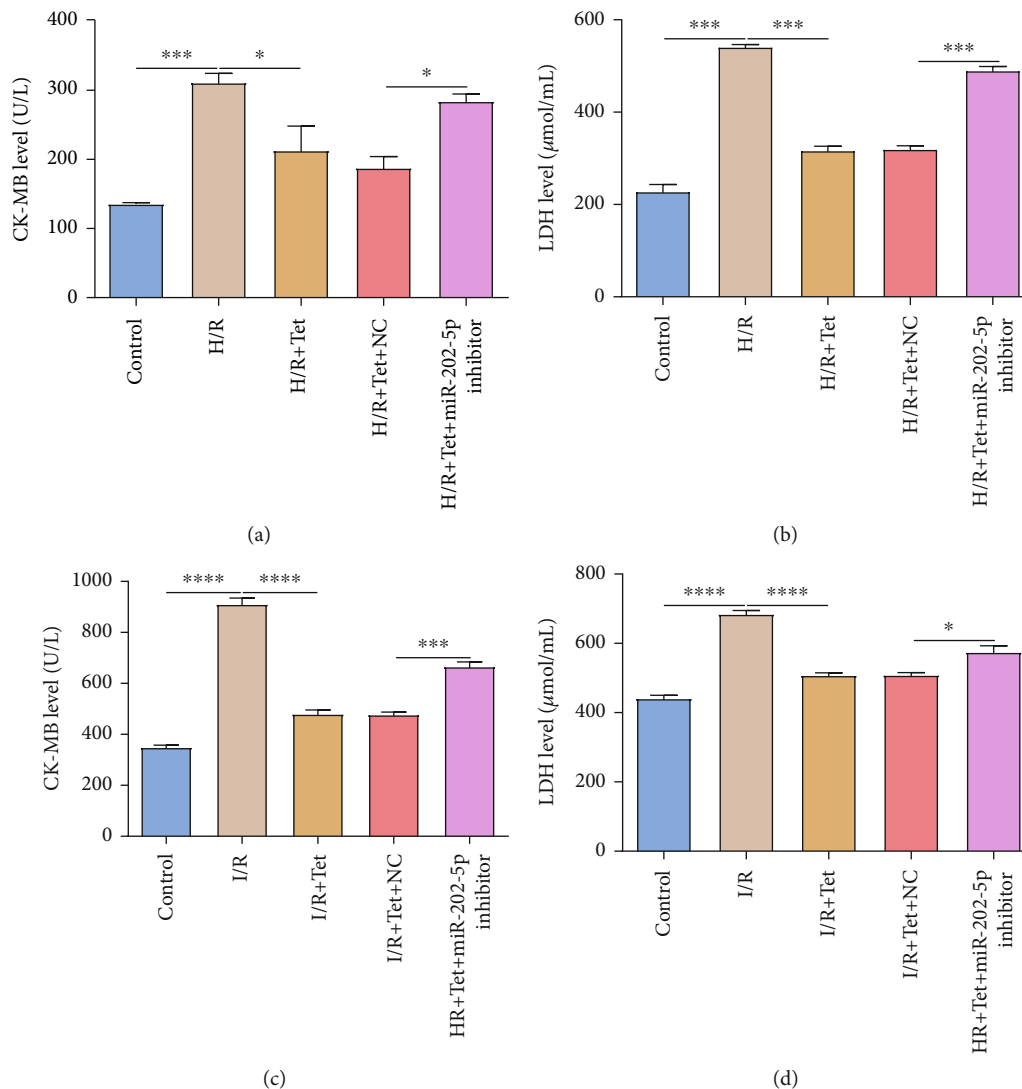


FIGURE 5: Tet lowers levels of cardiac marker enzymes in H/R-treated H9C2 cells and I/R rats via miR-202-5p. (a, b) ELISA results showing the levels of CK-MB and LDH in H/R H9C2 cells treated with Tet and/or miR-202-5p inhibitor. (c, d) ELISA detecting CK-MB and LDH levels in serum of I/R rats following treatment with Tet and/or miR-202-5p inhibitor. * $p < 0.05$; *** $p < 0.001$; **** $p < 0.0001$.

tissues of I/R rats in comparison to sham operation (Figure 3(a)). After treatment with 50 mg/kg Tet, its expression was distinctly elevated in myocardial tissues of I/R rats. However, following cotreatment with Tet and miR-202-5p inhibitor, its expression was lowered in I/R rats. In Figure 3(b), TRPV2 mRNA had a higher expression in I/R myocardial tissues than controls. Following treatment with Tet, its mRNA expression was reduced in I/R rats. However, during cotreatment with Tet and miR-202-5p inhibitor, TRPV2 mRNA expression was elevated in myocardial tissues of I/R rats compared to those treated with Tet (Figure 3(b)). Western blot was also presented to examine TRPV2 expression in myocardial tissues. As shown in Figures 3(c) and 3(d), higher expression of TRPV2 protein was detected in I/R myocardial tissues than controls. Tet treatment prominently decreased its expression in I/R myocardial tissues, which was reversed following cotreatment with miR-202-5p inhibitor. Apoptosis-related proteins were also detected by western blot. No significant difference in pro-caspase3

expression was found in myocardial tissues in different groups (Figures 3(c) and 3(e)). The expression of cleaved caspase3 (Figures 3(c) and 3(f)) and Bax (Figures 3(c) and 3(g)) was elevated in I/R myocardial tissues than controls. After treatment with Tet, their expression was significantly decreased. However, inhibition of miR-202-5p distinctly augmented cleaved caspase3 and Bax expression in myocardial tissues of I/R rats treated with Tet. Moreover, Bcl-2 expression was distinctly lowered in myocardial tissues of I/R rats than controls, which was improved by Tet treatment (Figures 3(c) and 3(h)). However, miR-202-5p inhibitor weakened the effects of Tet on Bcl-2 expression in myocardial tissues of I/R rats. Taken together, Tet treatment improved the miR-202-5p/TRPV2 axis in I/R-induced myocardial damage.

3.4. Tet Decreases TRPV2 Expression in I/R Myocardial Tissues via Increasing miR-202-5p. Using immunohistochemistry, we examined TRPV2 expression in myocardial

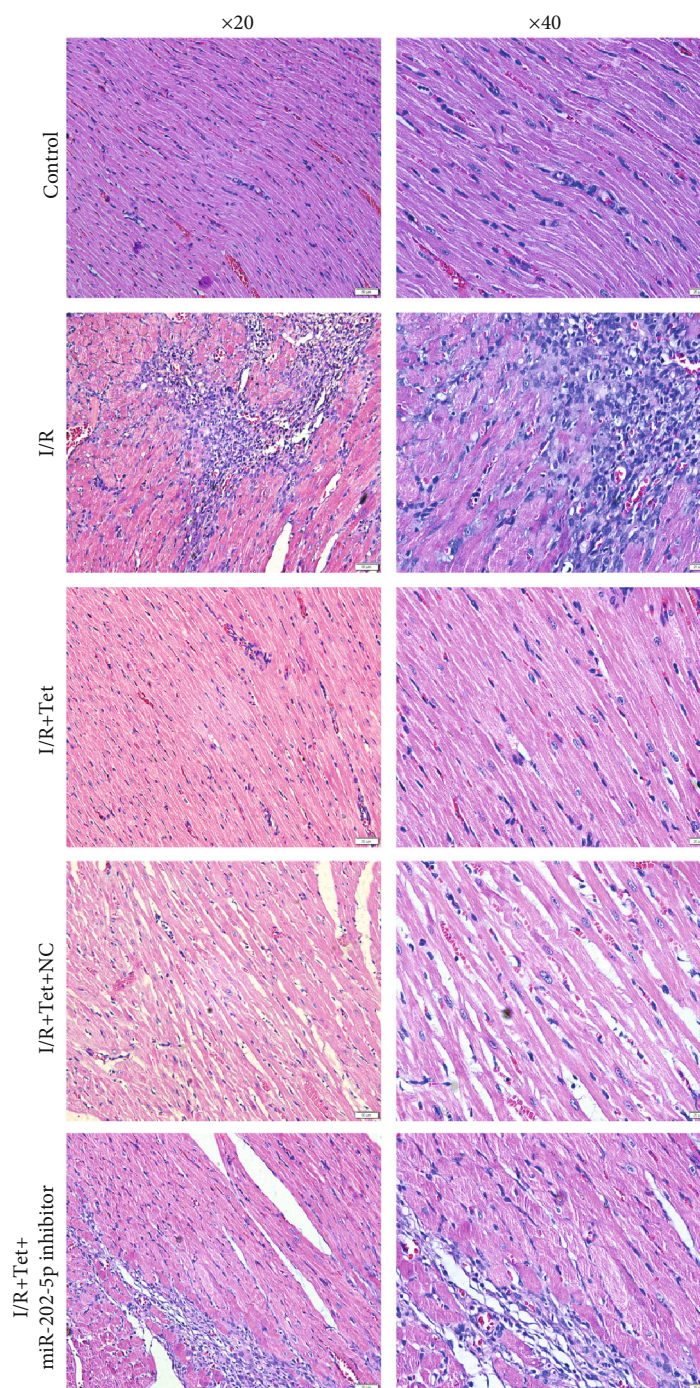


FIGURE 6: H&E staining showing the pathological changes in I/R myocardial tissues after treatment with Tet and/or miR-202-5p inhibitor. Scar bar: 50 and 20 μm . Magnification: $\times 20$ and $\times 40$.

tissues of each group. As shown in Figures 4(a) and 4(b), TRPV2 protein had a significantly higher expression in I/R myocardial tissues compared to controls. Following treatment with Tet, its expression was distinctly suppressed in I/R myocardial tissues. However, cotreatment of miR-202-5p inhibitor altered the decrease in TRPV2 expression induced by Tet in I/R myocardial tissues. Therefore, Tet could suppress TRPV2 expression in I/R myocardial tissues, partly related to miR-202-5p activation.

3.5. Tet Lowers Levels of Cardiac Marker Enzymes in H/R Cardiomyocytes and Serum of I/R Rats via miR-202-5p. ELISA was carried out to detect the levels of myocardial enzymes including CK-MB and LDH in H/R H9C2 cells and serum of I/R rats. In Figures 5(a) and 5(b), CK-MB and LDH levels were prominently gained in H/R-treated H9C2 cells. Tet could decrease their levels in H/R H9C2 cells. However, after inhibiting miR-202-5p, their levels were distinctly augmented in H/R cardiomyocytes treated with Tet

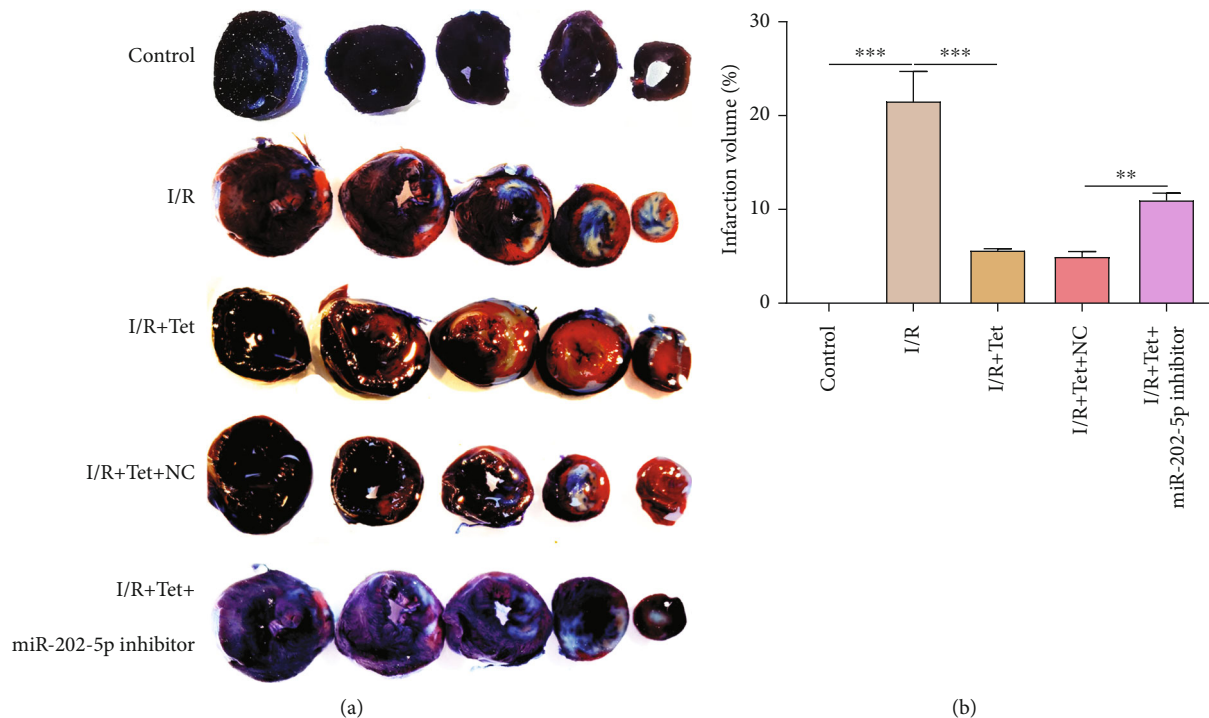


FIGURE 7: Evans blue-TCC staining detecting the myocardial infarction size in I/R rats treated with Tet and/or miR-202-5p inhibitor. (a) Representative images of Evans blue-TCC staining results. (b) The myocardial infarction size was quantified in each group. ** $p < 0.01$; *** $p < 0.001$; **** $p < 0.0001$.

(Figures 5(a) and 5(b)). Furthermore, in serum of I/R rats, CK-MB and LDH levels were both significantly higher than controls (Figures 5(c) and 5(d)). Tet treatment markedly decreased their levels in serum of I/R rats. But miR-202-5p inhibitor reversed their high levels in I/R rats treated with Tet. Thus, Tet may lower levels of cardiac marker enzymes in H/R cardiomyocytes as well as serum of I/R rats partly via activation of miR-202-5p.

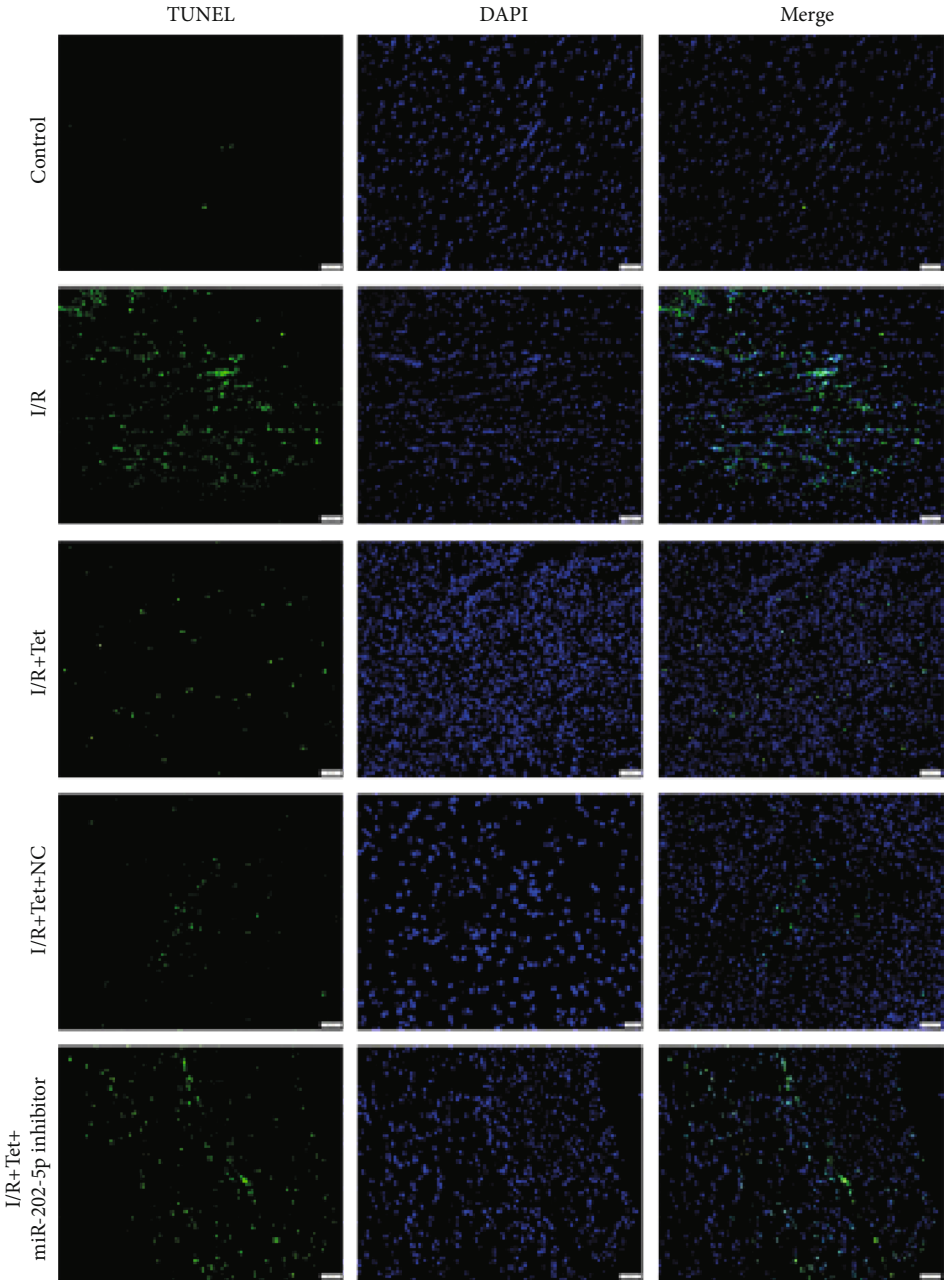
3.6. Tet Improves I/R-Induced Myocardial Infarction Size via miR-202-5p. H&E staining was used to investigate the myocardial damage in each group. As shown in Figure 6, myocardial injury was obvious in I/R-induced rats, which was distinctly ameliorated following treatment with Tet. However, myocardial injury was observed for I/R rats treated with Tet and miR-202-5p inhibitor. Myocardial infarction size was monitored via Evans blue-TCC staining. In Figures 7(a) and 7(b), myocardial infarction was obvious in I/R rats, improved by Tet treatment. miR-202-5p inhibitor could increase myocardial infarction volume in I/R rats treated with Tet.

3.7. Tet Decreases I/R-Induced Myocardial Apoptosis via miR-202-5p. Apoptosis in cardiomyocytes was examined via TUNEL staining. Our data demonstrated that cardiomyocyte apoptosis was markedly induced in I/R rats (Figures 8(a) and 8(b)). Following treatment with Tet, cardiomyocyte apoptosis was significantly ameliorated in I/R rats. miR-202-5p inhibitor improved cardiomyocyte apoptotic levels in I/R rats treated with Tet. Therefore, Tet treatment could reduce I/R-induced myocardial apoptosis partly via miR-202-5p.

4. Discussion

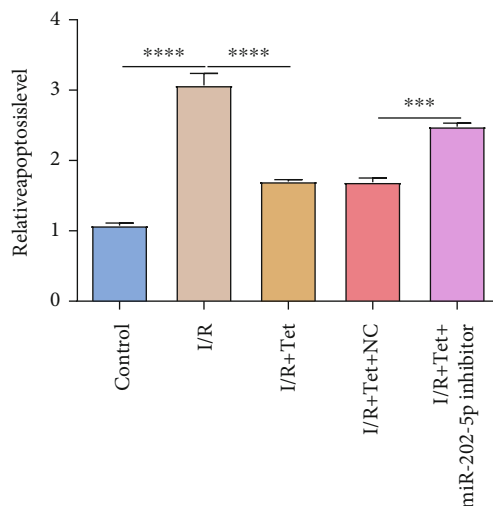
In this study, Tet could ameliorate cardiomyocyte apoptosis both in H/R cardiomyocytes cells and I/R rats. After treatment, I/R-induced myocardial infarction size was distinctly decreased. Previous studies have confirmed the protective roles of miR-202-5p on H/R cardiomyocytes and I/R myocardial tissues [10]. Hence, in this study, we investigated whether Tet treatment could increase miR-202-5p expression, thereby exerting the therapeutic effects on myocardial I/R damage. As expected, Tet increased miR-202-5p expression and decreased TRPV2 that was a target of miR-202-5p in myocardial I/R injury models. However, inhibiting miR-202-5p weakened the treatment effects of Tet. Thus, Tet could protect against myocardial I/R damage, which could have a close relationship with the miR-202-5p/TRPV2 axis.

miRNAs play a considerable part in regulating I/R-induced myocardial damage, which may be potential therapeutic targets for myocardial ischemic diseases [24–26]. Consistent with a previous study, miR-202-5p expression is lowered in H/R cardiomyocytes as well as I/R myocardial tissues [10]. Overexpression of miR-202-5p could ameliorate damage in H/R cardiomyocytes and I/R myocardial tissues. It has been found that miR-202-5p is involved in the regulation of cardiomyocyte autophagy [27]. Combining previous studies, inhibiting miR-202-5p may promote myocardial I/R injury. Thus, in this study, there were no miR-202-5p inhibitor and H/R+miR-202-5p groups. Herein, Tet treatment distinctly increased miR-202-5p expression in H/R cardiomyocytes as well as I/R myocardial tissues. Confirmed by dual luciferase report, miR-202-5p could directly bind to the



(a)

FIGURE 8: Continued.



(b)

FIGURE 8: Tet reduces myocardial apoptosis in I/R rats via miR-202-5p. (a) Representative images of TUNEL staining results. Scar bar: 50 μ m. (b) Cardiomyocyte apoptosis was quantified in I/R rats treated with Tet and/or miR-202-5p inhibitor. *** $p < 0.001$; **** $p < 0.0001$.

3'UTR region of TRPV2 [10]. TRPV2, as a target of miR-202-5p, is highly expressed in acute myocardial infarction tissues, consistent with our study results [28]. Overexpression of miR-202-5p could reduce myocardial I/R injury by inhibiting TRPV2. Studies have found that inhibiting TRPV2 activity can effectively improve heart function in patients with heart failure [29]. Tet treatment decreased miR-202-5p expression in H/R cardiomyocytes as well as I/R myocardial tissues. Thus, Tet ameliorated myocardial I/R injury, which may have a relationship with miR-202-5p and TRPV2.

Myocardial I/R damage exhibits a distinct relationship with cell apoptosis. Inhibition of apoptosis is a promising treatment strategy for I/R damage [30]. Our results showed that Tet treatment distinctly suppressed cardiomyocyte apoptosis in H/R-induced cardiomyocytes via flow cytometry. Moreover, according to TUNEL results, cardiomyocyte apoptosis was markedly ameliorated by Tet treatment in I/R myocardial tissues. Both in vitro and in vivo, cleaved caspase3 and Bax expression was suppressed and Bcl-2 expression was activated by Tet treatment. Previously, Tet could induce apoptosis of different cancer cells. For example, Tet can induce apoptosis of bladder cancer cells via the AMPK/mTOR axis [31]. Apoptosis of lung cancer cells is suppressed by Tet treatment through the VEGF/HIF-1 α /ICAM-1 pathway [32]. Based on these studies, Tet could be a promising drug for improvement of cardiomyocyte apoptosis in myocardial I/R damage.

It has been verified that Tet can improve cardiac function and weaken the progression of cardiac hypertrophy [33]. In H/R-induced cardiomyocytes as well as serum of I/R rats, Tet treatment significantly decreased the levels of myocardial enzymes (CK-MB and LDH), indicating the myocardial protection function was significantly ameliorated by Tet treatment. H&E depicted that I/R-induced myocardial damage was markedly reduced following treatment with Tet. More importantly, myocardial infarction was prominently lessened

for I/R rats treated by Tet. Our results revealed that Tet was a promising drug for treatment of myocardial I/R damage. Tet elevated miR-202-5p expression both in H/R cardiomyocytes and I/R myocardial tissues. After inhibiting miR-202-5p, the treatment effect of Tet on myocardial I/R injury was weakened. Thus, Tet exhibited a protective function against myocardial I/R damage, which could be in relationship with the miR-202-5p/TRPV2 axis.

5. Conclusion

Taken together, both in H/R cardiomyocytes and I/R rats, Tet may reduce myocardial I/R damage. Mechanically, Tet activated the miR-202-5p/TRPV2 pathway, thereby ameliorating myocardial I/R damage. Thus, Tet could become an underlying novel drug for treating myocardial I/R damage.

Abbreviations

Tet:	Tetrandrine
H/R:	Hypoxia/oxygenation
NC:	Negative control
I/R:	Ischemia reperfusion
miRNAs:	MicroRNAs
RT-qPCR:	Real-time quantitative PCR
CCK-8:	Cell Counting Kit-8 assay
LDH:	Lactate dehydrogenase
CK-MB:	Creatine kinetic acid MD
H&E:	Hematoxylin-eosin
TUNEL:	Transferase-mediated dUTP nick end labeling.

Data Availability

The datasets analyzed during the current study are available from the corresponding author on reasonable request.

Conflicts of Interest

The authors declare no conflicts of interest.

References

- [1] Z. Ma, Y. H. Lan, Z. W. Liu, M. X. Yang, H. Zhang, and J. Y. Ren, "MiR-19a suppress apoptosis of myocardial cells in rats with myocardial ischemia/reperfusion through PTEN/Akt/P-Akt signaling pathway," *European Review for Medical and Pharmacological Sciences*, vol. 24, no. 6, pp. 3322–3330, 2020.
- [2] Z. Ruan, W. Yu, and S. Wang, "CircNcX1/miR-133a: a potential novel biomarker and risk factor predictor for myocardial ischemia-reperfusion injury," *International Journal of Cardiology*, vol. 299, p. 256, 2020.
- [3] D. X. Tan, X. X. Chen, T. Z. Bai, J. Zhang, and Z. F. Li, "Sevoflurane up-regulates microRNA-204 to ameliorate myocardial ischemia/reperfusion injury in mice by suppressing Cot11," *Life Sciences*, vol. 259, article 118162, 2020.
- [4] S. Ghafouri-Fard, H. Shoorei, and M. Taheri, "Non-coding RNAs participate in the ischemia-reperfusion injury," *Biomedicine & Pharmacotherapy*, vol. 129, article 110419, 2020.
- [5] B. Kura, B. Szeiffova Bacova, B. Kalocayova, M. Sykora, and J. Slezak, "Oxidative stress-responsive microRNAs in heart injury," *International Journal of Molecular Sciences*, vol. 21, no. 1, p. 358, 2020.
- [6] Z. Zhao, Y. Zhao, L. Ying-Chun, L. Zhao, W. Zhang, and J. G. Yang, "Protective role of microRNA-374 against myocardial ischemia-reperfusion injury in mice following thoracic epidural anesthesia by downregulating dystrobrevin alpha-mediated Notch1 axis," *Journal of Cellular Physiology*, vol. 234, no. 7, pp. 10726–10740, 2019.
- [7] K. Liu, L. Ma, F. Zhou et al., "Identification of microRNAs related to myocardial ischemic reperfusion injury," *Journal of Cellular Physiology*, vol. 234, no. 7, pp. 11380–11390, 2019.
- [8] T. Liu, J. Guo, and X. Zhang, "MiR-202-5p/PTEN mediates doxorubicin-resistance of breast cancer cells via PI3K/Akt signaling pathway," *Cancer Biology & Therapy*, vol. 20, no. 7, pp. 989–998, 2019.
- [9] H. He, H. Yang, D. Liu, and R. Pei, "LncRNA NORAD promotes thyroid carcinoma progression through targeting miR-202-5p," *American Journal of Translational Research*, vol. 11, no. 1, pp. 290–299, 2019.
- [10] Y. Li, Q. Li, O. Zhang et al., "miR-202-5p protects rat against myocardial ischemia reperfusion injury by downregulating the expression of Trpv2 to attenuate the Ca²⁺ overload in cardiomyocytes," *Journal of Cellular Biochemistry*, vol. 120, no. 8, pp. 13680–13693, 2019.
- [11] G. Paradies, V. Paradies, F. M. Ruggiero, and G. Petrosillo, "Mitochondrial bioenergetics and cardiolipin alterations in myocardial ischemia-reperfusion injury: implications for pharmacological cardioprotection," *American Journal of Physiology. Heart and Circulatory Physiology*, vol. 315, no. 5, pp. H1341–h1352, 2018.
- [12] N. Robbins, S. E. Koch, and J. Rubinstein, "Targeting TRPV1 and TRPV2 for potential therapeutic interventions in cardiovascular disease," *Translational Research*, vol. 161, no. 6, pp. 469–476, 2013.
- [13] Z. Rozenbaum, L. Cohen, E. Bigelman, Y. Shacham, G. Keren, and M. Entin-Meer, "Downregulated expression of TRPV2 in peripheral blood cells following acute myocardial infarction is inversely correlated with serum levels of CRP and troponin I," *Cardiology*, vol. 139, no. 3, pp. 169–174, 2018.
- [14] E. Aguetaz, P. Bois, C. Cognard, and S. Seville, "Stretch-activated TRPV2 channels: role in mediating cardiopathies," *Progress in Biophysics and Molecular Biology*, vol. 130, Partt B, pp. 273–280, 2017.
- [15] R. Inoue, L. J. Jensen, J. Shi et al., "Transient receptor potential channels in cardiovascular function and disease," *Circulation Research*, vol. 99, no. 2, pp. 119–131, 2006.
- [16] Y. Iwata and T. Matsumura, "Blockade of TRPV2 is a novel therapy for cardiomyopathy in muscular dystrophy," *International Journal of Molecular Sciences*, vol. 20, no. 16, p. 3844, 2019.
- [17] M. Yu, T. Liu, Y. Chen, Y. Li, and W. Li, "Combination therapy with protein kinase inhibitor H89 and tetrandrine elicits enhanced synergistic antitumor efficacy," *Journal of Experimental & Clinical Cancer Research*, vol. 37, no. 1, p. 114, 2018.
- [18] Z. Zhang, T. Liu, M. Yu, K. Li, and W. Li, "The plant alkaloid tetrandrine inhibits metastasis via autophagy-dependent Wnt/ β -catenin and metastatic tumor antigen 1 signaling in human liver cancer cells," *Journal of Experimental & Clinical Cancer Research*, vol. 37, no. 1, p. 7, 2018.
- [19] Y. Jia, Y. Miao, M. Yue, M. Shu, Z. Wei, and Y. Dai, "Tetrandrine attenuates the bone erosion in collagen-induced arthritis rats by inhibiting osteoclastogenesis via spleen tyrosine kinase," *The FASEB Journal*, vol. 32, no. 6, pp. 3398–3410, 2018.
- [20] Y. Lin, J. Yao, M. Wu et al., "Tetrandrine ameliorates airway remodeling of chronic asthma by interfering TGF- β 1/Nrf-2/HO-1 signaling pathway-mediated oxidative stress," *Canadian Respiratory Journal*, vol. 2019, Article ID 7930396, 12 pages, 2019.
- [21] W. Guo, X. Liu, J. Li et al., "Prdx1 alleviates cardiomyocyte apoptosis through ROS-activated MAPK pathway during myocardial ischemia/reperfusion injury," *International Journal of Biological Macromolecules*, vol. 112, pp. 608–615, 2018.
- [22] Q. Li, J. Yang, J. Zhang et al., "Inhibition of microRNA-327 ameliorates ischemia/reperfusion injury-induced cardiomyocytes apoptosis through targeting apoptosis repressor with caspase recruitment domain," *Journal of Cellular Physiology*, vol. 235, no. 4, pp. 3753–3767, 2020.
- [23] T. J. Zhang, R. X. Guo, X. Li, Y. W. Wang, and Y. J. Li, "Tetrandrine cardioprotection in ischemia-reperfusion (I/R) injury via JAK3/STAT3/hexokinase II," *European Journal of Pharmacology*, vol. 813, pp. 153–160, 2017.
- [24] S. Ding, D. Liu, L. Wang, G. Wang, and Y. Zhu, "Inhibiting microRNA-29a protects myocardial ischemia-reperfusion injury by targeting SIRT1 and suppressing oxidative stress and NLRP3-mediated pyroptosis pathway," *The Journal of Pharmacology and Experimental Therapeutics*, vol. 372, no. 1, pp. 128–135, 2020.
- [25] Z. Liu, Y. Liu, Y. Zhu, and J. Gong, "HOTAIR/miRNA-1/Cx43: a potential mechanism for treating myocardial ischemia-reperfusion injury," *International Journal of Cardiology*, vol. 308, p. 11, 2020.
- [26] X. Lv, P. Lu, Y. Hu, and T. Xu, "miR-346 inhibited apoptosis against myocardial ischemia-reperfusion injury via targeting Bax in rats," *Drug Design, Development and Therapy*, vol. - Volume 14, pp. 895–905, 2020.
- [27] H. Xing, M. Peng, Z. Li, J. Chen, H. Zhang, and X. Teng, "Ammonia inhalation-mediated mir-202-5p leads to cardiac

- autophagy through PTEN/AKT/mTOR pathway,” *Chemosphere*, vol. 235, pp. 858–866, 2019.
- [28] M. Entin-Meer and G. Keren, “Potential roles in cardiac physiology and pathology of the cation channel TRPV2 expressed in cardiac cells and cardiac macrophages: a mini-review,” *American Journal of Physiology. Heart and Circulatory Physiology*, vol. 318, no. 1, pp. H181–h188, 2020.
- [29] Y. Iwata, S. Ito, S. Wakabayashi, and M. Kitakaze, “TRPV2 channel as a possible drug target for the treatment of heart failure,” *Laboratory Investigation*, vol. 100, no. 2, pp. 207–217, 2020.
- [30] Q. Zhao, Z. Cui, Y. Zheng et al., “Fenofibrate protects against acute myocardial I/R injury in rat by suppressing mitochondrial apoptosis as decreasing cleaved caspase-9 activation,” *Cancer Biomarkers*, vol. 19, no. 4, pp. 455–463, 2017.
- [31] B. Kou, W. Liu, X. Xu et al., “Autophagy induction enhances tetrandrine-induced apoptosis via the AMPK/mTOR pathway in human bladder cancer cells,” *Oncology Reports*, vol. 38, no. 5, pp. 3137–3143, 2017.
- [32] Z. Chen, L. Zhao, F. Zhao, G. Yang, and J. J. Wang, “Tetrandrine suppresses lung cancer growth and induces apoptosis, potentially via the VEGF/HIF-1 α /ICAM-1 signaling pathway,” *Oncology Letters*, vol. 15, no. 5, pp. 7433–7437, 2018.
- [33] D. F. Shen, Q. Z. Tang, L. Yan et al., “Tetrandrine blocks cardiac hypertrophy by disrupting reactive oxygen species-dependent ERK1/2 signalling,” *British Journal of Pharmacology*, vol. 159, no. 4, pp. 970–981, 2010.

Research Article

Development of Microsatellite Marker System to Determine the Genetic Diversity of Experimental Chicken, Duck, Goose, and Pigeon Populations

Xiulin Zhang ¹, Yang He ¹, Wei Zhang ¹, Yining Wang ¹, Xinmeng Liu ¹,
Aique Cui ¹, Yidi Gong ¹, Jing Lu,¹ Xin Liu,¹ Xueyun Huo,¹ Jianyi Lv,¹ Meng Guo,¹
Xiaoyan Du,¹ Lingxia Han,² Hongyan Chen,² Jilan Chen,³ Changlong Li ¹
and Zhenwen Chen ¹

¹Capital Medical University, School of Basic Medical Sciences, Beijing 100069, China

²Harbin Veterinary Research Institute of Chinese Academy of Agricultural Sciences, Harbin 150069, China

³Institute of Animal Sciences, Chinese Academy of Agricultural Sciences, Beijing 100193, China

Correspondence should be addressed to Changlong Li; licl@ccmu.edu.cn and Zhenwen Chen; czwen@ccmu.edu.cn

Received 10 September 2020; Revised 9 December 2020; Accepted 5 January 2021; Published 15 January 2021

Academic Editor: Monica Fedele

Copyright © 2021 Xiulin Zhang et al. This is an open access article distributed under the Creative Commons Attribution License, which permits unrestricted use, distribution, and reproduction in any medium, provided the original work is properly cited.

Poulties including chickens, ducks, geese, and pigeons are widely used in the biological and medical research in many aspects. The genetic quality of experimental poulties directly affects the results of the research. In this study, following electrophoresis analysis and short tandem repeat (STR) scanning, we screened out the microsatellite loci for determining the genetic characteristics of Chinese experimental chickens, ducks, geese, and pigeons. The panels of loci selected in our research provide a good choice for genetic monitoring of the population genetic diversity of Chinese native experimental chickens, ducks, geese, and ducks.

1. Introduction

Laboratory animals are important experimental materials for science research. They play key roles in the investigation of pathogenesis, diagnosis of diseases, pharmaceutical research, and other fields [1]. The genetic quality of laboratory animals directly affects the accuracy, repeatability, and scientificity of medical biological research results. Genetic monitoring is one of the effective methods to evaluate population's genetic diversity. Through genetic monitoring, whether genetic mutations and genetic pollution occurred can be analyzed.

Poultry, including chicken, duck, goose, and pigeon, has become commonly used laboratory animals [2]. They are easy to reproduce and hatch in vitro. Among them, chickens are the most widely used poultry in life science research [3, 4]. Ducks, geese, and pigeons also play important roles in

the research of epidemiology, immunology, virology, and pharmacotoxicology [5–9]. There are many genetic analysis and quality control methods applied to chickens [10, 11]. However, at present, we find few reports about the genetic analysis systems and quality control methods of duck, goose, and pigeon populations, especially in the Chinese native groups.

Hence, in this study, we screened out the microsatellite loci with uniform distribution, stable amplification, and rich polymorphism in experimental chickens, ducks, geese, and pigeons with different genetic backgrounds [12]. We developed effective microsatellite marker systems to determine the genetic diversity of experimental chickens, ducks, geese, and pigeons, which will lay the foundation for the genetic quality control of them and promote the application of experimental poultry.

2. Materials and Methods

2.1. Animal Sample. Three outbred groups and three haplotype groups of experimental chicken were used in this research: outbred group BWEL-SPF chickens ((SCXK (black) 2017-005)), 40 samples, 37 weeks old, 6 males and 34 females, which has been closed for 20 generations; outbred group BM chicken (from BWEL chicken lineage (SCXK (black) 2017-005)), 40 samples, 14 weeks old, 6 males and 34 females; outbred group Beijing oil chickens, 46 samples. MHC haplotype chickens were bred from the 13th generation of BWEL chicken, the haplotype was continuously selected based on the MHC core genes, and the half-sibling or sibling mating method was used to breed to the 8th generation [13]. We selected 5 G1 haplotype chickens, 53 weeks old, 1 male and 4 females; 5 G2 haplotype chickens, 93 weeks, 1 male and 4 females; and 5 G7 haplotype chickens, 82 weeks, 1 male and 4 females. The Beijing oil chickens came from the Institute of Animal Science (IAS), Chinese Academy of Agricultural Sciences (CAAS). Other samples were from Harbin Veterinary Research Institute (HVRI), CAAS. All the samples were blood.

Two outbred groups and four haplotype groups of experimental duck (bred from Jinding (JD) duck lineage (SCXK (black) 2017-006)) were selected: outbred group 1, 40 samples, 37 weeks old, 6 males and 34 females; outbred group JD duck, 40 samples, 37 weeks old, 6 males and 34 females; 10 A haplotype ducks, 53 weeks old, 1 male and 4 females; 10 B haplotype ducks, 53 weeks old, 1 male and 4 females; 10 C haplotype ducks, 53 weeks old, 1 male and 4 females; 10 D haplotype ducks, 53 weeks old, 1 male and 4 females. All the samples are duck muscle tissue and were from HVRI, CAAS.

We collected two outbred groups of experimental geese: outbred group Guangdong Wuzong goose, 44 samples, 37 weeks old, 6 males and 34 females; outbred group Yangzhou goose, 44 samples, 37 weeks old, 6 males and 34 females. All the samples are goose liver tissue. Guangdong Wuzong geese were from Southern Medical University, and Yangzhou geese were from Yangzhou University.

Forty pigeons were randomly selected from two populations of white king pigeons and silver king pigeons, half male and half female, with no age limit. All the animals were from Liujinlong pigeon farms in Beijing. Their heart tissues were collected.

All breeding is carried out in accordance with Chinese agricultural standards NY/T 1901. What is more, all experiments followed the 3R principle.

2.2. Microsatellite Locus Selection. By searching PubMed and using SSR Hunter software to analyze animal gene information, we obtained microsatellite loci for further screening.

2.3. DNA Extraction. Phenol-chloroform extraction method was used to extract DNA from muscle, liver, and heart tissue. TIANamp Blood DNA Kits (Tiangen, Beijing, China) were used to extract DNA from chicken blood samples. All DNA concentrations were diluted to 50 ng/ μ L, stored in -20°C .

2.4. PCR Procedure and Agarose Gel Electrophoresis. The PCR was performed in a 20 μ L reaction volume containing 10 μ L Dream Taq Green PCR Master Mix (Thermo Fisher Scientific, Massachusetts, MA), 2 μ L pure water (ddH₂O), 10 pmol each primer, and 50 ng of the extracted DNA template. The PCR protocol was as follows: 94 $^{\circ}\text{C}$ for 5 min, followed by 35 cycles of 94 $^{\circ}\text{C}$ for 30 s, suitable temperature for 30 s, 72 $^{\circ}\text{C}$ for 30 s, and a final extension at 72 $^{\circ}\text{C}$ for 5 min. Amplified products were stored at -20°C for further analysis.

Amplified products were electrophoresed on a 2% agarose gel at 130 V, 90 min.

2.5. STR Scanning. We performed STR scanning on PCR amplification products of candidate loci. The forward primers of candidate microsatellite loci were fluorescent labelled with FAM, HEX, and TAMRA. The sample genome was amplified with fluorescent primers, and the amplified products were scanned by STR through 3730xl DNA Analyzer (Applied Biosystems, Thermo Fisher Scientific, Massachusetts, USA). All the STR scanning was performed by Beijing Tianyi Huiyuan Biotechnology Co., Ltd.

2.6. Data Analysis. GeneMarker V2.2.0 software was used to analyze the length of amplified fragments from different populations at each microsatellite locus. Popgene 3.2 software was used to analyze the observed number of alleles, effective number of alleles, Shannon's information index, and effective heterozygosity of microsatellite loci. The polymorphic information content of multiple sites was calculated using PIC calculation software (PIC_CALC.0.6).

3. Results

3.1. Microsatellite Locus Selection

3.1.1. Preliminary Screening of Microsatellite Loci by PCR. Firstly, we obtained the microsatellite locus information of experimental chickens, ducks, geese, and pigeons by searching previous reports on PubMed and using the SSR Hunter software to analyze the genetic information of different populations [14, 15]. We collected 72, 59, 57, and 61 microsatellite loci of experimental chicken, duck, goose, and pigeon, respectively.

In order to clarify the amplification conditions of the microsatellite loci and exclude the loci with poor specificity, we performed temperature gradient PCR and agarose gel electrophoresis of microsatellite loci. Then, we performed PCR amplification on the most suitable conditions and subjected the PCR products to agarose gel electrophoresis to screen out loci with suitable length, good polymorphism in outbred groups, good monomorphism in haplotypes, and high specificity. Taking the chicken GGNCAMZO locus and duck AY264 locus as example, the results are shown in Figure 1. GGNCAMZO locus is monomorphic in the haplotype chicken population, and AY264 locus is polymorphic in the outbred duck group.

In summary, we selected 37 and 32 microsatellite loci with good polymorphism in the outbred groups and haplotypes of chicken, respectively [12, 16, 17]. In addition, 15 and 23 loci

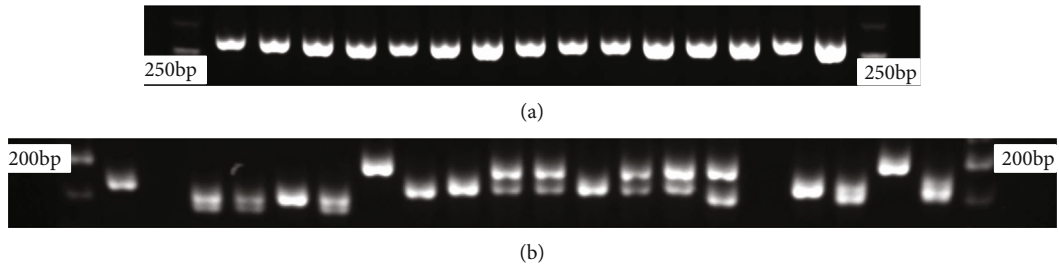


FIGURE 1: Results of agarose gel electrophoresis of microsatellite DNA locus GGNCAMZO in experimental chickens and locus AY264 in experimental ducks. (a) GGNCAMZO in haplotype chicken line G1. (b) AY264 in the outbred group of experimental ducks.

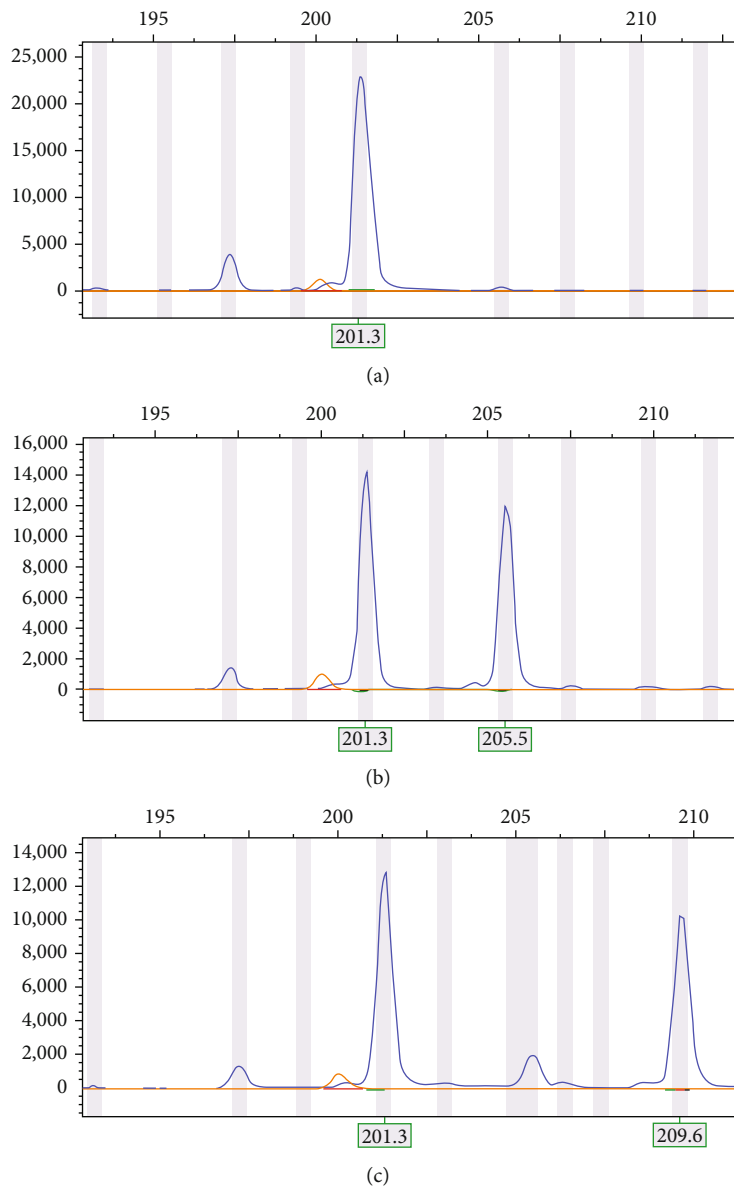


FIGURE 2: Results of UU-Cl μ T47 scan of the experimental pigeons. (a) The STR graph corresponding to the sample of haplotype under primer UU-Cl μ T47 shows homozygote with a wave peak of 201 bp. (b) The STR diagram corresponding to the sample of outbred groups under primer UU-Cl μ T47 shows heterozygote with two wave peaks of 201 bp and 205 bp, respectively. (c) The STR diagram corresponding to the sample of outbred groups under primer UU-Cl μ T47 shows heterozygote with two wave peaks of 201 bp and 209 bp, respectively.

TABLE 1: Number of alleles, optimal amplification conditions, and fragment length of 29 alleles for the laboratory chickens.

Loci	Primer sequence (5'-3')	Temperature(°C)	Allele range	Applicable groups
MCW0029	GTGGACACCCATTTGTACCCTATG CATGCAATTCAGGACCGTGCA	63.8	139-188	Outbred group
ADL0293	GTAATCTAGAAACCCATCT ACATACCGCAGTCTTTGTTC	53.9	106-120	Outbred group
ADL0317	AGTTGGTTTCAGCCATCCAT CCCAGAGCACACTGTCACTG	58.5	177-219	Outbred group
GCT0016	TCCAAGGTTCTCCAGTTC GGCATAAAGGATAGCAACAG	52.2	111-148	Outbred group
ADL0304	GGGAGGAACTCTGGAAATG CCTCATGCTTCGTGCTTTTT	53.9	138-161	Outbred group
LEI0074	GACCTGGTCTGACATGGGTG GTTTGCTGATTAGCCATCGCG	58.5	221-243	Outbred group
ADL328	CACCCATAGCTGTGACTTTG AAAACCGGAATGTGTAACCTG	53.9	107-120	Outbred group
GGANTECI	GCGGGGCCGTTATCAGAGCA AGTGCAGGGCGCTCCTGGT	65.0	139-194	Outbred group
LEI094	CAGGATGGCTGTTATGCTTCCA CACAGTGCAGAGTGGTGCGA	56.0	176-211	Outbred group
MCW0330	TGGACCTCATCAGTCTGACAG AATGTTCTCATAGAGTTCCTGC	58.5	217-287	Outbred group
LEI0141	CGCATTGATGCATAACACATG AAGGCAAACCTCAGCTGGAACG	52.2	221-245	Outbred group
MCW0087	ATTTCTGCAGCCAACCTGGAG CTCAGGCAGTTCTCAAGAACA	58.5	268-289	Outbred group
MCW0347	GCTTCCAGATGAGCTCCATGG CACAGCGCTGCAGCAACTG	52.0	121-149	Outbred group
ADL176	TTGTGGATTCTGGTGGTAGC TTCTCCCGTAACACTCGTCA	58.5	183-200	Outbred group
ADL0201	GCTGAGGATTCAGATAAGAC AATGGCYGACGTTTCACAGC	58.5	111-151	Outbred group
GGNCAMZO	GTCCTAGGTTAGCAGCATG GCTGGATACAGACCTCGATT	56.0	234	Outbred group Haplotype
GGAVIR	AGAGATGGTGCACGCAACCT CGAGCACTTCTGGCAGAGA	60.7	86-89	Outbred group Haplotype
MCW0063	GGCTCCAAAAGCTTGTTCTTAGCT GAAAACCAGTAAAGCTTCTTAC	53.9	116-146	Outbred group Haplotype
ADL185	CATGGCAGCTGACTCCAGAT AGCGTTACCTGTTCTGTTGC	58.5	116-142	Outbred group Haplotype
GGMYC	CGAGGCGCTCTGCGAGTTTA TGGGGACCTCTGGCTCTGAC	62.4	139-151	Outbred group Haplotype
LEI0094	GATCTCACCAGTATGAGCTGC TCTCACACTGTAACACAGTGC	53.9	250-283	Outbred group Haplotype
GGVITC	AGCCATCATTGAGGCATCT GATGTCCTGAGTGATGCTCA	58.5	86	Outbred group Haplotype
ADL0292	CCAAATCAGGCAAACTTCT AAATGGCCTAAGGATGAGGA	58.5	110-136	Outbred group Haplotype
GGVITIIG	GGCAGGTTTCTAATGCCTGA CCCATCGTTCAACTGTATG	56.0	186-189	Outbred group Haplotype

TABLE 1: Continued.

Loci	Primer sequence (5'-3')	Temperature(°C)	Allele range	Applicable groups
ADL166	TGCCAGCCCGTAATCATAGG	58.5	131-154	Outbred group Haplotype
	AAGCACCACGACCCAATCTA			
MCW0014	AAAATATTGGCTCTAGGAACTGTC	58.5	172-195	Outbred group Haplotype
	ACCGGAAATGAAGGTAAGACTAGC			
GGCYMA	AGCGAGGCGCTCTGCGAGTT	64.6	140-153	Outbred group Haplotype
	GGGCACCTCTGGCTCTGACC			
MCW0402	ACTGTGCCTAGGACTAGCTG	56.0	141-229	Outbred group Haplotype
	CCTAAGTCTGGGCTCTTCTG			
STMSGGHU2-1A	CTTAATATGTGTGAGGTGGC	53.9	235-238	Haplotype
	GTTCTCACAATTGCATTAGC			

were screened in the outbred groups and haplotypes of duck, respectively [14, 18, 19]. In the outbred groups of goose and pigeon, 14 and 20 microsatellite loci were chosen [18, 20–23]. Loci in these panels would be candidate for the final microsatellite marker evaluation systems.

3.1.2. STR Scanning Analysis. In order to further complete the microsatellite marker system, we performed STR scanning on the candidate microsatellite DNA loci matched microsatellite criteria and analyzed the length of the amplified product at the peak with GeneMarker software (V1.75). Taking the UU-Cl μ T47 locus as an example, it showed polymorphism in the outbred group of pigeon (Figure 2).

We finally determined that in experimental chickens, 28 loci were selected for genetic monitoring in the outbred groups and 14 loci for haplotypes. All microsatellite DNA loci are shown in Table 1. There are 13 common loci.

In experimental duck populations, we chose 25 loci and 15 loci for genetic monitoring in the outbred duck groups and haplotype groups. There are 12 common loci. Microsatellite loci are shown in Table 2.

14 microsatellite loci with good polymorphism were considered as microsatellite markers in the outbred group of goose. Table 3 demonstrates the number of alleles, optimal amplification conditions, and fragment length of 14 alleles for the outbred experiment geese.

In the outbred group of pigeon, we finally screened out 16 microsatellite loci with good polymorphism, several alleles, and typical stutter peaks. All microsatellite locus information is shown in Table 4.

3.1.3. Analysis of Population Microsatellite Loci. We inputted the results of STR scanning into Popgene 3.2 to analyze experimental chicken in the outbred groups and the haplotypes at 29 loci. In the outbred groups, 28 microsatellite loci show a high degree of polymorphism, and the average number of observed alleles is 4.571. The average number of effective alleles is 3.270, and the average Shannon's information index is 1.198 (Table 5). Furthermore, the average effective heterozygosity is 0.492. The average polymorphism information content (PIC) is 0.610. All these data indicate a good genetic diversity of screening loci in the outbred groups and

large heterozygosity difference among the laboratory experimental chicken populations.

In the other 3 haplotype populations, 14 microsatellite loci showed monomorphism in each population but showed different lengths in different haplotype populations. The average number of observed alleles is 1.571. The average number of effective alleles, the average Shannon's information index, and the average effective heterozygosity are 1.433, 0.316, and 0.207, respectively (Table 6). The specific data of each haplotype population is shown in Supplementary Tables 1–3.

In the outbred group of duck, 25 microsatellite loci show polymorphism. The average number of observed alleles is 7.520, and the average number of effective alleles in the population is 4.162. The average Shannon's information index is 1.574, and the average effective heterozygosity is 0.683. The average PIC is 0.698. These data showed that in the outbred groups, the genetic diversity of microsatellite DNA loci is better, and the genetic diversity of each locus is quite different. The specific results are shown in Table 7.

In 4 haplotype populations, 15 microsatellite loci show monomorphism in each population. The average number of observed alleles is 4.133, the average number of effective alleles is 2.863, and the average Shannon's information index is 1.153, indicating that the genetic diversity of the loci in these haplotype populations is poor; the average effective heterozygosity is 0.500, indicating that the heterozygosity difference is small and the genetic information of the selected loci is relatively single. See Table 8 for more detailed information, and the specific data in each haplotype population is shown in Supplementary Tables 4–7.

In the outbred colony of experimental goose, 14 loci were selected. The average number of observed alleles, the average number of effective alleles, the average Shannon's information index, the average effective heterozygosity, and the PIC are 4.714, 3.038, 1.195, 0.528, and 0.582, respectively. The microsatellite loci have large interindividual differences within the population, and the population has high gene stability (Table 9).

The selected microsatellite loci all show good polymorphism in the experimental outbred pigeon populations. A total of 16 loci were selected. The average number of observed alleles is 7.875. The average effective allele number

TABLE 2: Number of alleles, optimal amplification conditions, and fragment length of 28 alleles for the laboratory ducks.

Loci	Primer sequence(5'-3')	Temperature (°C)	Allele range	Applicable groups
CAUD007	ACTTCTCTGTAGGCATGTCA CACCTGTTGCTCCTGCTGT	60.8	100-190	Outbred group
CAUD004	TCCACTTGGTAGACCTTGAG TGGGATTCAGTGAGAAGCCT	60.8	234-385	Outbred group
CAUD023	CACATTAACACTACATTTTCGGTCT CAGCCAAAGAGTTCAACAGG	51.4	163-234	Outbred group
CAUD027	AGAAGGCAGGCAAATCAGAG TCCACTCATAAAAAACCCACA	66.0	70-180	Outbred group
CAUD001	ACAGCTTCAGCAGACTTAGA GCAGAAAGTGATTAAGGAAG	55.5	150-247	Outbred group
CAUD031	AGCATCTGGACTTTTTCTGGA CACCCCAGGCTCTGAGATAA	51.4	107-187	Outbred group
CAUD032	GAAACCAACTGAAAACGGGC CCTCCTGCGTCCCAATAAG	58.1	96-206	Outbred group
AY314	CTCATTCCAATTCCTCTGTA CAGCATTATTATTCAGAAGG	50.3	112-329	Outbred group
CMO211	GGATGTTGCCCCACATATTT TTGCCTTGTTTATGAGCCATT	55.0	112-205	Outbred group
APH09	GGATGTTGCCCCACATATTT TTGCCTTGTTTATGAGCCATTA	58.0	134-190	Outbred group
APH11	GGACCTCAGGAAAATCAGTGTA GCAGGCAGAGCAGGAAATA	58.5	183-185	Outbred group
APL2	GATTCAACCTTAGCTATCAGTCTCC CGCTCTTGCAAATGTCC	58.5	115-125	Outbred group
CAUD011	TGCTATCCACCCAATAAGTG CAAAGTTAGCTGGTATCTGC	50.3	145-223	Outbred group
CAUD006	ATGGTTCTCTGTAGGCAATC TTCTGCTTGGGCTCTTGA	63.5	183-290	Outbred group Haplotype
CAUD018	TTAGACAAATGAGGAAATAGTA GTCCAAACTAAATGCAGGC	50.3	100-180	Outbred group Haplotype
CAUD010	GGATGTGTTTTTCATTATTGAT AGAGGCATAAATACTCAGTG	50.3	138-200	Outbred group Haplotype
CAUD012	ATTGCCTTTCAGTGGAGTTTC CGGCTCTAAACACATGAATG	63.5	182-286	Outbred group Haplotype
CAUD014	CACAACTGACGGCACAAAGT CTGAGTTTTTCCCGCCTCTA	58.1	136-200	Outbred group Haplotype
CAUD034	TACTGCATATCACTAGAGGA TAGGCATACTCGGGTTTAG	55.5	160-296	Outbred group Haplotype
CAUD035	GTGCCTAACCCCTGATGGATG CTTATCAGATGGGGCTCGGA	63.5	174-282	Outbred group Haplotype
APL579	ATTAGAGCAGGAGTTAGGAGAC GCAAGAAGTGGCTTTTTTC	55.0	116-227	Outbred group Haplotype
AY258	ATGTCTGAGTCCTCGGAGC ACAATAGATTCCAGATGCTGAA	58.1	89-162	Outbred group Haplotype
CMO212	CTCCACTAGAACACAGACATT CATCTTTGGCATTTTGAAG	58.0	186-272	Outbred group Haplotype
CAUD028	TACACCCAAGTTTATTCTGAG ACTCTCCAGGGCACTAGG	55.5	152-226	Outbred group Haplotype

TABLE 2: Continued.

Loci	Primer sequence(5'-3')	Temperature (°C)	Allele range	Applicable groups
CAUD026	ACGTCACATCACCCACAG CTTTCCTCTGGTGAGGTTT	60.8	134-196	Outbred group Haplotype
APH18	TTCTGGCCTGATAGGTATGAG GAATTGGGTGGTTCATACTGT	58.0	178-325	Haplotype
CAUD002	CTTCGGTGCCTGTCTTAGC AGCTGCCTGGAGAAGGTCT	60.8	200-231	Haplotype
CAUD005	CTGGGTTTGGTGGAGCATAA TACTGGCTGCTTCATTGCTG	60.8	184-290	Haplotype

TABLE 3: Number of alleles, optimal amplification conditions, and fragment length of 14 alleles for the outbred colony laboratory geese.

Loci	Primer sequence(5'-3')	Temperature (°C)	Allele range
G-Ans17	ACAAATAACTGGTTCTAAGCAC AGAGGACTTCTATTTCATAAATA	51.0	111-123
G-TTUCG1	CCCTGCTGGTATACCTGA GTGTCTACACAACAGC	53.0	113-115
G-APH13	CAACGAGTGACAATGATAAAA CAATGATCTCACTCCCAATAG	53.0	163-165
G-Ans02	TTCTGTGCAGGGGCGAGTT AGGGAACCGATCACGACATG	58.0	202-230
G-Ans07	GACTGAGGAACATAAATTGACT ACAAAGACTACTACTGCCAAG	62.0	236-246
G-Ans18	GTGTTCTCTGTTTATGATATTAC AACAGAATTTGCTTGAACTGC	56.0	229-237
G-Ans25	CACTTATTAATGGCACTTGAAA GTTCTCTTGTCACAACCTGGA	62.0	261-277
G-Hhiμ1b	ATCAAAGGCACAATGTGAAAT AGTAAGGGGGCTTCCACC	60.0	212-216
G-CKW47	AACTTCTGCACCTAAAACTGTCA TGCTGAGGTAACAGGAATTAATA	56.0	213-215
G-Bcaμ5	AGTGTTTCTTTCATCTCCACAAGC AGACCACAATCGGACCACATATTC	56.0	197-201
G-Bcaμ7	TAGTTTCTATTTGCACCCAATGGAG CGGTCCTGTCCTTGTGCTGTAA	60.0	171-175
G-Bcaμ8	CCCAAGACTCACAAAACCAGAAAT ATGAAAGAAGAGTTAAACGTGTGCAA	58.0	155-159
G-CAUD006	ATGGTTCTCTGTAGGCAATC TTCTGCTTGGGCTCTTGGA	56.0	170-210
G-APH20	ACCAGCCTAGCAAGCACTGT GAGGCTTTAGGAGAGATTGAAAAA	53.0	140-150

is 4.554; the average Shannon's information index and the average effective heterozygosity are 1.559 and 0.649. The average PIC is 0.674 (Table 10).

3.1.4. Population Genetic Structure Analysis. Among the three outbred chicken groups, the mean number of observed alleles, the mean number of effective alleles, the mean Shan-

non's information index, and the mean effective heterozygosity are shown in Table 11. All these data are the highest in the Beijing oil chicken, indicating the best gene diversity.

In the haplotype chicken populations, the highest mean observed number of alleles is observed in G7 groups. Haplotype G7 has the highest mean effective allele number and the highest mean Shannon's information index. The mean

TABLE 4: Number of alleles, optimal amplification conditions, and fragment length of 16 alleles for the outbred colony laboratory pigeons.

Loci	Primer sequence(5' -3')	Temperature (°C)	Allele range
UU-Cl02	TGGGCAAGGTACACTTTTAGGT CTTTATGCTCCCCCTTGAGAT	61.0	158-170
UU-Cl06	TTTGAAAAACATGGATTGTGC AATTTGCAGAGGGTGAGTGG	56.0	140-145
PG5	GTTCTTGGTGTTCATGGATGC AGTTACGAAATGATTGCCAGAAG	59.0	262-266
C26L9(1265223)	CAAAGCTGCTGACGTGAATCAA AGAGACGCTCCATGCAAAAAG	59.0	467-472
UU-Cl14	CAGAACGTTTTGTTCTGTTTGG TCTTGCTGCAGTCTTCATCC	58.0	265-292
C12L1(532572)	GTTGTTTGGCTGAGTGGACG TCAACCAGGGGAATTGGCAG	62.0	126-136
C12L4(906353)	GCTGCTGTCTTCTTCATTGGG TTAAAACCTCCCGTCTCCCTG	60.0	210-250
Cl μ D11	CCAATCCCAAAGAGGATTAT ACTGTCCTATGGCTGAAGTG	58.0	78-98
C26L10(1404758)	GCTGTCAGGTATCAGCCACAA TCAGACCCACGAAAGCTGTAA	59.0	211-226
C26L4(568923)	CAACCCCATGTGGGTGAGAC CACCACCACGTGGGACATC	63.0	357-432
PG4	CCCATCTCCTGCCTGATGC CACAGCAGGATGCTGCCTGC	64.0	136-170
UU-Cl12	CGCCAGACTGTATTGTGAGC AGCATGGCTGTTCTTTGAGG	61.0	231-265
Cl μ T47	ATGTGTGTTTGTGCATGAAG ATGAAAGCCTGTTAGTGGAA	56.0	183-214
Cl μ D32	GAGCCATTTTCAGTGAGTGACA GTTTGCAGGAGCGTGTAGAGAAGT	60.0	136-158
UU-Cl07	GCTGCCTGTTACTACCTGAGC CTGGCCATGAAATGAACTCC	61.0	277-310
C26L1(20390)	AGGAGCCTACACTGGGTTTTTC TGTAGCTCTGCAATCAGCCT	60.0	250-268

effective heterozygosity of haplotype G7 is 0.364. The genetic heterozygosity of the 3 populations is very low, and the consistency is good (Table 12).

In the two outbred groups of duck, the mean number of observed alleles, the mean effective number of alleles, the mean Shannon's index, and the mean effective heterozygosity of outbred group 1 are higher than those of outbred group JD, indicating that outbred group 1 had better diversity. The results are shown in Table 13. Among the 4 haplotype populations, the highest mean number of alleles is observed in haplotype A. Haplotype A has the highest mean Shannon's information index. The highest mean effective heterozygosity in the duck groups is 0.489 in haplotype A (Table 14). The genetic heterozygosity of 4 populations is in good agreement.

In the two outbred groups of goose, the mean number of observed alleles, the mean effective number of alleles, and the mean Shannon's index of Guangdong Wuzong goose are

higher than those of Yangzhou goose, indicating that Guangdong Wuzong goose has a better diversity (Table 15).

The analysis of the two main experimental pigeon populations used for scientific research shows that the mean effective heterozygosity of two populations is 0.647 and 0.651, respectively. The mean number of observed alleles, the mean effective number of alleles, and the mean Shannon's index are higher in white king pigeons than in silver king pigeons. The comparison of the data is shown in Table 16.

4. Discussion

Poultry are widely used and are indispensable supporting conditions for the life sciences and biomedicine industries. Specific pathogen-free (SPF) chicken embryos are used in the manufacture and quality control of biological product [4]; ducks play an important role in the research of avian

TABLE 5: Number of alleles, effective alleles, effective heterozygosity, PIC, and Shannon's index of the outbred colony chicken samples.

Loci	Observed number of alleles	Effective number of alleles	Shannon's information index	Effective heterozygosity	PIC
MCW0029	4	2.931	1.209	0.579	0.603
GGNCAMZO	2	1.069	0.146	0.060	0.062
ADL0293	5	3.200	1.311	0.573	0.634
ADL0317	7	5.236	1.768	0.554	0.783
GGAVIR	3	1.916	0.796	0.456	0.408
ADL0201	5	2.103	1.013	0.429	0.482
GCT0016	5	3.042	1.274	0.337	0.618
ADL0304	6	4.641	1.627	0.666	0.751
MCW0402	8	6.042	1.881	0.702	0.813
MCW0063	7	4.319	1.626	0.568	0.736
ADL185	5	3.204	1.359	0.614	0.647
GGMYC	2	1.800	0.637	0.427	0.346
LEI0094	6	3.674	1.468	0.562	0.683
LEI0074	4	3.707	1.348	0.597	0.681
ADL328	3	2.785	1.058	0.526	0.565
GGVITC	1	1.000	0.000	0.000	1.000
GGANTECL	3	2.897	1.080	0.600	0.580
LEI094	6	4.444	1.579	0.690	0.738
MCW0330	4	3.232	1.269	0.577	0.637
LEI0141	4	3.162	1.229	0.341	0.623
ADL0292	3	2.793	1.061	0.475	0.568
GGVITIIG	2	1.965	0.684	0.460	0.371
MCW0087	8	5.930	1.898	0.544	0.810
MCW0347	3	1.948	0.815	0.447	0.419
ADL176	9	4.846	1.858	0.522	0.773
ADL166	5	3.729	1.380	0.574	0.682
MCW0014	5	4.342	1.543	0.592	0.735
GGCYMA	3	1.603	0.632	0.317	0.322
Mean	4.571	3.270	1.198	0.492	0.610

TABLE 6: Number of alleles, effective alleles, effective heterozygosity, and Shannon's index of the haplotype chicken samples.

Loci	Observed number of alleles	Effective number of alleles	Shannon's information index	Effective heterozygosity
GGNCAMZO	1	1.000	0.000	0.000
GGAVIR	2	1.923	0.673	0.480
MCW0402	1	1.000	0.000	0.000
MCW0063	1	1.000	0.000	0.000
ADL185	3	2.174	0.898	0.540
GGMYC	1	1.000	0.000	0.000
LEI0094	3	2.778	1.055	0.640
GGVITC	1	1.000	0.000	0.000
ADL0292	2	1.471	0.500	0.320
GGVITIIG	2	2.000	0.693	0.500
ADL166	1	1.000	0.000	0.000
MCW0014	1	1.000	0.000	0.000
GGCYMA	1	1.000	0.000	0.000
STMSGGHU2-1A	2	1.724	0.611	0.420
Mean	1.571	1.434	0.316	0.207

TABLE 7: Number of alleles, effective alleles, effective heterozygosity, PIC, and Shannon's index of outbred colony duck samples.

Loci	Observed number of alleles	Effective number of alleles	Shannon's information index	Effective heterozygosity	PIC
CMO211	8	4.628	1.698	0.764	0.752
CAUD011	9	5.024	1.835	0.799	0.775
CAUD027	9	3.698	1.588	0.654	0.696
APH09	8	4.840	1.728	0.756	0.763
AY314	12	7.285	2.165	0.806	0.848
AY258	9	3.503	1.586	0.700	0.684
CAUD018	4	2.941	1.194	0.640	0.596
CAUD031	8	4.459	1.711	0.730	0.746
CAUD026	7	4.674	1.697	0.750	0.757
CAUD023	7	2.725	1.315	0.584	0.591
CMO212	8	4.154	1.642	0.739	0.724
CAUD006	4	3.333	1.280	0.440	0.645
CAUD004	7	5.556	1.834	0.720	0.798
CAUD001	6	5.000	1.696	0.600	0.772
CAUD034	10	3.943	1.742	0.730	0.723
CAUD007	8	3.894	1.639	0.714	0.713
APL579	7	3.068	1.412	0.635	0.636
CAUD010	6	4.655	1.630	0.768	0.753
CAUD028	5	3.549	1.378	0.541	0.668
CAUD012	7	3.122	1.354	0.652	0.630
CAUD035	10	5.768	1.922	0.759	0.804
CAUD014	9	3.600	1.448	0.696	0.672
CAUD032	14	6.159	2.120	0.797	0.821
APH11	2	1.923	0.673	0.479	0.365
APL2	4	2.556	1.067	0.609	0.529
Mean	7.520	4.162	1.574	0.683	0.698

TABLE 8: Number of alleles, effective alleles, effective heterozygosity, and Shannon's index of haplotype duck samples.

Loci	Observed number of alleles	Effective number of alleles	Shannon's information index	Effective heterozygosity
CAUD002	3	2.020	0.857	0.360
CAUD006	4	2.740	1.142	0.540
CAUD018	3	1.802	0.746	0.400
CAUD005	5	3.945	1.490	0.551
APL579	5	2.632	1.205	0.500
APH18	7	4.301	1.655	0.640
CAUD010	3	2.597	1.010	0.420
CAUD028	2	1.980	0.688	0.360
CAUD012	3	2.597	1.010	0.420
CAUD035	4	3.756	1.353	0.605
CAUD014	4	3.509	1.306	0.580
CAUD026	4	2.740	1.142	0.520
CMO212	5	3.774	1.458	0.640
AY258	4	2.353	1.063	0.500
CAUD034	6	2.198	1.164	0.460
Mean	4.133	2.863	1.153	0.500

influenza, fatty liver, duck hepatitis A, and duck hepatitis B [5–7]; goose blood contains a higher concentration of immunoglobulin, which is often used in pharmacology and toxicology research [8]; pigeons belong to the class of birds and are considered as important animal model in avian influenza research [9]. With the increasing demand for experiment poultry, people are paying more attention to the genetic structure analysis and genetic quality control. However, the current methods of genetic structure analysis and genetic quality control for experimental poultry animals are insufficient.

Coat colour gene testing method, biochemical marker gene testing method, immune marker gene testing method, and DNA molecular marker method are popular methods for genetic monitoring. Microsatellite DNA, mitochondrial DNA (mtDNA), restriction fragment length polymorphism (PCR-RFLP), single-stranded conformation polymorphism (PCR-SSCP), and specific gene polymorphisms are commonly used DNA molecular marker methods [24–27]. Among them, microsatellite DNA has become valuable tools for evaluating population genetic diversity due to their unique virtue.

Microsatellite DNA is characterized by short tandem repeats (STRs) of 1 to 6 nucleotides in eukaryotic genome with a random manner [28]. It has rich polymorphism and

TABLE 9: Number of alleles, effective alleles, effective heterozygosity, PIC, and Shannon's index of outbred colony goose samples.

Loci	Observed number of alleles	Effective number of alleles	Shannon's information index	Effective heterozygosity	PIC
G-Ans17	4	1.843	0.775	0.441	0.388
G-TTUCG1	3	2.255	0.943	0.381	0.494
G-APH13	4	1.605	0.752	0.315	0.352
G-Ans02	8	5.389	1.837	0.749	0.790
G-Ans07	4	3.073	1.220	0.634	0.613
G-Ans18	3	2.208	0.922	0.309	0.481
G-Ans25	4	3.333	1.282	0.629	0.647
G-Hhi μ 1b	4	2.965	1.147	0.471	0.594
G-CKW47	4	3.143	1.238	0.573	0.623
G-Bca μ 5	3	2.728	1.051	0.469	0.562
G-Bca μ 7	6	2.731	1.158	0.455	0.562
G-Bca μ 8	7	2.845	1.290	0.635	0.599
G-CAUD006	4	3.704	1.344	0.602	0.680
G-APH20	8	4.713	1.772	0.734	0.761
Mean	4.714	3.038	1.195	0.528	0.582

TABLE 10: Number of alleles, effective alleles, effective heterozygosity, PIC, and Shannon's index of outbred colony pigeon samples.

Loci	Observed number of alleles	Effective number of alleles	Shannon's information index	Effective heterozygosity	PIC
UU-Cl μ 02	5	3.613	1.374	0.694	0.672
UU-Cl μ 06	4	2.921	1.163	0.383	0.593
PG5	2	1.681	0.595	0.397	0.323
C26L9(1265223)	4	2.576	1.076	0.602	0.533
UU-Cl μ 14	10	5.144	1.923	0.787	0.784
C12L1(532572)	4	2.810	1.118	0.487	0.575
C12L4(906353)	11	6.375	2.052	0.766	0.825
Cl μ D11	7	4.541	1.682	0.734	0.750
C26L10(1404758)	11	9.118	2.281	0.860	0.880
C26L4(568923)	13	5.854	2.062	0.807	0.812
PG4	10	6.847	2.017	0.767	0.836
UU-Cl μ 12	8	2.825	1.364	0.623	0.599
Cl μ T47	7	3.492	1.413	0.658	0.666
Cl μ D32	9	6.695	1.991	0.807	0.833
UU-Cl μ 07	5	1.352	0.592	0.252	0.251
C26L1(20390)	16	7.014	2.244	0.759	0.844
Mean	7.875	4.554	1.559	0.649	0.674

TABLE 11: Comparison of mean observed allele number, mean effective allele number, mean Shannon's index, and mean effective heterozygosity among the outbred colonies of chickens.

Colonies	Mean observed number of alleles	Mean effective number of alleles	Mean Shannon's information index	Mean effective heterozygosity
BWEL	2.857	2.024	0.730	0.424
BM	2.857	2.132	0.802	0.485
Beijing oil chicken	4.464	2.821	1.088	0.569

TABLE 12: Comparison of mean observed allele number, mean effective allele number, mean Shannon's index, and mean effective heterozygosity among the haplotype chickens.

Colonies	Mean observed number of alleles	Mean effective number of alleles	Mean Shannon's information index	Mean effective heterozygosity
G1	1.571	1.434	0.316	0.207
G2	1.643	1.409	0.335	0.224
G7	2.000	1.626	0.548	0.364

TABLE 13: Comparison of mean observed allele number, mean effective allele number, mean Shannon's index, and mean effective heterozygosity among the outbred colonies of ducks.

Colonies	Mean observed number of alleles	Mean effective number of alleles	Mean Shannon's information index	Mean effective heterozygosity
1	6.320	3.518	1.410	0.685
JD	5.280	3.466	1.335	0.680

TABLE 14: Comparison of mean observed allele number, mean effective allele number, mean Shannon's index, and mean effective heterozygosity among the haplotype ducks.

Colonies	Mean observed number of alleles	Mean effective number of alleles	Mean Shannon's information index	Mean effective heterozygosity
A	2.400	2.022	0.760	0.489
B	2.333	2.029	0.745	0.484
C	2.400	1.912	0.726	0.459
D	2.333	1.944	0.701	0.442

large genetic information. Microsatellite can be used to distinguish heterozygous from homozygous because of their codominant inheritance feature [29]. In previous studies, microsatellites have been used as biomarkers for monitoring rodent genetic traits [30, 31]. With the deep understanding of microsatellites, it plays a more important role in genetic monitoring for being simple, clear, and stable in operation. In this research, we screened out microsatellite loci with suitable length and high specificity as candidate loci by gel electrophoresis firstly. Then, we performed STR scanning on these candidate loci. Microsatellite loci with good polymorphism, abundant alleles in the outbred groups, and good monomorphism in the haplotype populations were selected to form the microsatellite marker system. We analyzed the average effective allele number, average Shannon's index, average effective heterozygosity, and other analytical indices to estimate genetic variation in different groups.

The mean effective number of alleles is an indicator of genetic variation and mutation drift balance. In our study, Beijing oil chicken has the highest mean effective allele

number of three outbred chicken populations; outbred duck group 1 has higher mean effective allele number than outbred duck group JD. The outbred goose group Guangdong Wuzong and outbred pigeon group white king have the highest mean number of effective alleles in outbred goose populations and outbred pigeon populations, respectively. The higher mean effective number of alleles indicates that the population can maintain the original gene and avoid new variations under the pressures from genetic drift and artificial selection. The results show that Beijing oil chicken, outbred duck group 1, Guangdong Wuzong goose, and white king pigeon are the most stable strains in the outbred group of experiment chicken, duck, goose, and pigeon groups in this research, respectively.

The mean effective heterozygosity of a population is an important indicator of population genetic diversity and can reflect the richness of the detected genes. It is generally believed that when the mean effective heterozygosity of the population is less than 0.5, it indicates that the individual differences in the population are small and the genetic heterozygosity is low, which does not conform to the genetic characteristics of an outbred group animal. When the mean effective heterozygosity of the population is higher than 0.7, its genetic diversity is high [32].

Hence, we found that the mean effective heterozygosity of BWEL, BM, and Beijing oil chicken groups is all greater than 0.5, which conforms to the characteristics of the outbred group. The mean effective heterozygosity of BWEL and BM chicken groups is nearly 0.5. The average effective heterozygosity of G1, G2, and G7 groups is all less than 0.5. It is also consistent with the background that BWEL, BM, and Beijing oil chickens are outbred colonies; Beijing oil chicken has abundant genetic diversity and high selection potential for it has the highest mean effective heterozygosity among the outbred chicken groups in this study. This may be due to the large population. Duck group 1 and JD duck all have a mean effective heterozygosity greater than 0.680 which indicates a high genetic diversity. The mean effective heterozygosity of Guangdong Wuzong goose group, silver king pigeon group, and white king pigeon group is all greater than 0.5 which reflects abundant genetic diversity. The mean effective heterozygosity of three haplotype chicken groups and four haplotype duck groups is 0.207 and 0.500, respectively. The result indicates a good consistency in haplotype chickens and ducks. This may be the result of long-term full-sib and half-sib reproduction. Chickens and ducks are more widely used in biological research, and the breeding standards are stricter, while geese and pigeons are more useful in agriculture. Haplotype chickens have lower mean effective heterozygosity than haplotype duck populations, which is consistent with a longer history of breeding in experimental chickens.

When measuring the degree of gene variation, PIC is often used as a variation index. It is generally believed that when PIC is between 0.25 and 0.5, it is moderately polymorphic, and <0.25 shows a low level of polymorphism, when PIC is greater than 0.5, it means a high level of polymorphism [33]. In our microsatellite marker system, most of the microsatellite sites have a PIC greater than 0.5 that show high

TABLE 15: Comparison of mean observed allele number, mean effective allele number, mean Shannon's index, and mean effective heterozygosity among the outbred colonies of geese.

Colonies	Mean observed number of alleles	Mean effective number of alleles	Mean Shannon's information index	Mean effective heterozygosity
Guangdong Wuzong	4.000	2.769	1.112	0.618
Yangzhou	3.714	2.155	0.802	0.439

TABLE 16: Comparison of mean observed allele number, mean effective allele number, mean Shannon's index, and mean effective heterozygosity among the outbred colonies of pigeons.

Colonies	Mean observed number of alleles	Mean effective number of alleles	Mean Shannon's information index	Mean effective heterozygosity
Silver king	6.125	3.260	1.307	0.647
White king	7.375	4.247	1.435	0.651

polymorphism. All these data prove that our microsatellite marker system provides rich genetic information, which can be used as effective genetic markers. In our study, highly polymorphic microsatellite marker systems showed powerful markers for quantifying genetic variations within and between poultry populations. We will collect more samples to make a more accurate description of genetic structure of the Chinese experimental chickens, ducks, geese, and pigeons in the future [34].

5. Conclusions

In conclusion, we identified appropriate microsatellite marker systems for native experimental chickens, ducks, geese, and pigeons in China. The combination of loci selected in our research provides a good choice for genetic monitoring of the quality and the population genetic diversity of poultry stocks.

Data Availability

All data, models, and code generated or used during the study appear in the submitted article.

Conflicts of Interest

The authors declare that there is no conflict of interest regarding the publication of this paper.

Acknowledgments

We are very grateful to the Institute of Animal Science, Chinese Academy of Agricultural Sciences, Harbin Veterinary Research Institute, Southern Medical University and Yangzhou University for providing animal samples for this study. This work was supported by the Beijing Municipal Science and Technology Projects (No. D181100000518002), Support Project of High-level Teachers in Beijing Municipal Universi-

ties in the Period of 13th Five-year Plan (Grant Number IDHT20170516), and the National Key Research and Development Plan of China (No. 2017YFD0501602).

Supplementary Materials

Supplementary Table 1: number of alleles, effective alleles, effective heterozygosity, and Shannon's index of the G1 haplotype chicken population. Supplementary Table 2: number of alleles, effective alleles, effective heterozygosity, and Shannon's index of the G2 haplotype chicken population. Supplementary Table 3: number of alleles, effective alleles, effective heterozygosity, and Shannon's index of the G7 haplotype chicken population. Supplementary Table 4: number of alleles, effective alleles, effective heterozygosity, and Shannon's index of the A haplotype duck population. Supplementary Table 5: number of alleles, effective alleles, effective heterozygosity, and Shannon's index of the B haplotype duck population. Supplementary Table 6: number of alleles, effective alleles, effective heterozygosity, and Shannon's index of the C haplotype duck population. Supplementary Table 7: number of alleles, effective alleles, effective heterozygosity, and Shannon's index of the D haplotype duck population. (*Supplementary Materials*)


References

- [1] E. P. Neff, "What is a lab animal?," *Lab Anim (NY)*, vol. 47, no. 9, pp. 223–227, 2018.
- [2] M. B. Bello, K. Yusoff, A. Ideris, M. Hair-Bejo, B. P. H. Peeters, and A. R. Omar, "Diagnostic and vaccination approaches for Newcastle disease virus in poultry: the current and emerging perspectives," *BioMed Research International*, vol. 2018, 18 pages, 2018.
- [3] M. L. Dequéant and O. Pourquié, "Chicken genome: new tools and concepts," *Developmental dynamics : an official publication of the American Association of Anatomists*, vol. 232, no. 4, pp. 883–886, 2005.
- [4] H. B. Yin, C. H. Chen, M. J. Darre, A. M. Donoghue, D. J. Donoghue, and K. Venkitanarayanan, "Phytochemicals reduce aflatoxin-induced toxicity in chicken embryos," *Poultry Science*, vol. 96, no. 10, pp. 3725–3732, 2017.
- [5] A. M. Ramey, A. B. Reeves, J. Z. Drexler et al., "Influenza A viruses remain infectious for more than seven months in northern wetlands of North America," *Proceedings of the Royal Society B: Biological Sciences*, vol. 287, no. 1934, p. 20201680, 2020.
- [6] Y. Fu, M. Pan, X. Wang, Y. Xu, H. Yang, and D. Zhang, "Molecular detection and typing of duck hepatitis A virus directly from clinical specimens," *Veterinary Microbiology*, vol. 131, no. 3-4, pp. 247–257, 2008.

- [7] Q. Pan, L. Liu, Y. Wang et al., "The first whole genome sequence and pathogenicity characterization of a fowl adenovirus 4 isolated from ducks associated with inclusion body hepatitis and hydropericardium syndrome," *Avian Pathology*, vol. 46, no. 5, pp. 571–578, 2017.
- [8] T. Huang, K. Wu, X. Yuan et al., "Molecular analysis of the immunoglobulin genes in goose," *Developmental and Comparative Immunology*, vol. 60, pp. 160–166, 2016.
- [9] J. H. Kwon, Y. K. Noh, D. H. Lee et al., "Experimental infection with highly pathogenic H5N8 avian influenza viruses in the mandarin duck (*Aix galericulata*) and domestic pigeon (*Columba livia domestica*)," *Veterinary Microbiology*, vol. 203, pp. 95–102, 2017.
- [10] M. Nunome, K. Kinoshita, S. Ishishita, Y. Ohmori, A. Murai, and Y. Matsuda, "Genetic diversity of 21 experimental chicken lines with diverse origins and genetic backgrounds," *Experimental Animals*, vol. 68, no. 2, pp. 177–193, 2019.
- [11] M. G. Strillacci, M. C. Cozzi, E. Gorla et al., "Genomic and genetic variability of six chicken populations using single nucleotide polymorphism and copy number variants as markers," *Animal : an international journal of animal bioscience*, vol. 11, no. 5, pp. 737–745, 2017.
- [12] H. Khatib, E. Genislaw, L. B. Crittenden, N. Bumstead, and M. Soller, "Sequence-tagged microsatellite sites as markers in chicken reference and resource populations," *Animal Genetics*, vol. 24, no. 5, pp. 355–362, 1993.
- [13] C. Gao, L. Han, J. Han et al., "Establishment of six homozygous MHC-_B haplotype populations associated with susceptibility to Marek's disease in Chinese specific pathogen-free BWEL chickens," *Infection, Genetics and Evolution*, vol. 29, pp. 15–25, 2015.
- [14] D. Seo, M. S. Bhuiyan, H. Sultana, J. M. Heo, and J. H. Lee, "Genetic diversity analysis of south and east Asian duck populations using highly polymorphic microsatellite markers," *Asian-Australasian Journal of Animal Sciences*, vol. 29, no. 4, pp. 471–478, 2016.
- [15] S. A. Stringham, E. E. Mulroy, J. Xing et al., "Divergence, convergence, and the ancestry of feral populations in the domestic rock pigeon," *Current biology : CB*, vol. 22, no. 4, pp. 302–308, 2012.
- [16] J. H. Seo, J. H. Lee, and H. S. Kong, "Assessment of genetic diversity and phylogenetic relationships of Korean native chicken breeds using microsatellite markers," *Asian-Australasian Journal of Animal Sciences*, vol. 30, no. 10, pp. 1365–1371, 2017.
- [17] B. H. Rudresh, H. N. N. Murthy, M. R. Jayashankar, C. S. Nagaraj, A. M. Kotresh, and S. M. Byregowda, "Microsatellite based genetic diversity study in indigenous chicken ecotypes of Karnataka," *Veterinary world*, vol. 8, no. 8, pp. 970–976, 2015.
- [18] Y. Huang, J. Tu, X. Cheng et al., "Characterization of 35 novel microsatellite DNA markers from the duck (*Anas platyrhynchos*) genome and cross-amplification in other birds," *Genetics, selection, evolution : GSE*, vol. 37, no. 5, pp. 455–472, 2005.
- [19] Y. Su, R. Long, G. Chen, X. Wu, K. Xie, and J. Wan, "Genetic analysis of six endangered local duck populations in China based on microsatellite markers," *Journal of Genetics and Genomics*, vol. 34, pp. 1010–1018, 2007.
- [20] J. C.-I. Lee, L.-C. Tsai, Y.-Y. Kuan et al., "Racing pigeon identification using STR and chromo-helicase DNA binding gene markers," *Electrophoresis*, vol. 28, no. 23, pp. 4274–4281, 2007.
- [21] K. Andres and E. Kapkowska, "Applicability of anatin and galiform microsatellite markers to the genetic diversity studies of domestic geese (*Anser anser domesticus*) through the genotyping of the endangered zatorska breed," *BMC Research Notes*, vol. 4, no. 1, pp. 1–10, 2011.
- [22] R. Parada, J. Ksiazkiewicz, M. Kawka, and K. Jaszczak, "Studies on resources of genetic diversity in conservative flocks of geese using microsatellite DNA polymorphic markers," *Molecular Biology Reports*, vol. 39, no. 5, pp. 5291–5297, 2012.
- [23] N. R. Lebas and P. B. Spencer, "Polymorphic microsatellite markers in the ornate dragon lizard, *Ctenophorus ornatus*," *Molecular ecology*, vol. 9, no. 3, pp. 365–366, 2000.
- [24] I. Barbaric, M. Stewart, S. Wells, and T. N. Dear, "A new coat color mouse line for testing germline transmission of embryonic stem cells while retaining an inbred genetic background," *Journal of the American Association for Laboratory Animal Science*, vol. 46, no. 3, pp. 37–40, 2007.
- [25] M. N. Weitzmann, K. J. Woodford, and K. Usdin, "The mouse Ms6-hm hypervariable microsatellite forms a hairpin and two unusual tetraplexes," *The Journal of Biological Chemistry*, vol. 273, no. 46, pp. 30742–30749, 1998.
- [26] G. Bulfield and G. Bantin, "Genetic monitoring of inbred strains of mice using electrophoresis and electrofocusing," *Laboratory Animals*, vol. 15, no. 2, pp. 147–149, 1981.
- [27] J. R. Fahey, H. Katoh, R. Malcolm, and A. V. Perez, "The case for genetic monitoring of mice and rats used in biomedical research," *Mammalian genome : official journal of the International Mammalian Genome Society*, vol. 24, no. 3–4, pp. 89–94, 2013.
- [28] Y. C. Li, A. B. Korol, T. Fahima, A. Beiles, and E. Nevo, "Microsatellites: genomic distribution, putative functions and mutational mechanisms: a review," *Molecular Ecology*, vol. 11, no. 12, pp. 2453–2465, 2002.
- [29] A. Grover and P. C. Sharma, "Development and use of molecular markers: past and present," *Critical Reviews in Biotechnology*, vol. 36, no. 2, pp. 290–302, 2014.
- [30] X. Liu, X. Yu, Y. Xu et al., "Development of an effective microsatellite marker system to determine the genetic structure of *Meriones meridianus* populations," *Experimental Animals*, vol. 69, no. 2, pp. 224–232, 2020.
- [31] X. Y. Du, W. Li, X. Y. Sa et al., "Selection of an effective microsatellite marker system for genetic control and analysis of gerbil populations in China," *Genetics and Molecular Research*, vol. 14, no. 3, pp. 11030–11042, 2015.
- [32] R. Chakraborty, Y. Zhong, M. de Andrade, P. R. Clemens, R. G. Fenwick, and C. T. Caskey, "Linkage disequilibria among (CA)_n polymorphisms in the human dystrophin gene and their implications in carrier detection and prenatal diagnosis in Duchenne and Becker muscular dystrophies," *Genomics*, vol. 21, no. 3, pp. 567–570, 1994.
- [33] T. Vanhala, M. Tuiskula-Haavisto, K. Elo, J. Vilkki, and A. Mäki-Tanila, "Evaluation of genetic variability and genetic distances between eight chicken lines using microsatellite markers," *Poultry Science*, vol. 77, no. 6, pp. 783–790, 1998.
- [34] J. K. Pritchard, M. Stephens, and P. Donnelly, "Inference of population structure using multilocus genotype data," *Genetics*, vol. 155, no. 2, pp. 945–959, 2000.

Research Article

Coadministration of Ketamine and Perampanel Improves Behavioral Function and Reduces Inflammation in Acute Traumatic Brain Injury Mouse Model

Faleh Alqahtani ¹, Mohammed A. Assiri,¹ Mohamed Mohany,¹ Imran Imran ², Sana Javaid,^{2,3} Muhammad Fawad Rasool,⁴ Waleed Shakeel,² Farzane Sivandzade,⁵ Ahmed Z. Alanazi,¹ Salim S. Al-Rejaie ¹, Musaad A. Alshammari,¹ Fawaz Alasmari,¹ Mohammed Mufadhe Alanazi,¹ and Faisal F. Alamri^{6,7}

¹Department of Pharmacology and Toxicology, College of Pharmacy, King Saud University, Riyadh 11451, Saudi Arabia

²Department of Pharmacology, Faculty of Pharmacy, Bahauddin Zakariya University, Multan 60800, Pakistan

³Department of Pharmacy, The Women University, Multan 60000, Pakistan

⁴Department of Pharmacy Practice, Faculty of Pharmacy, Bahauddin Zakariya University, Multan 60800, Pakistan

⁵Department of Pharmaceutical Sciences, Texas Tech University Health Sciences Center, Amarillo, TX 79106, USA

⁶College of Sciences and Health Profession, King Saud bin Abdulaziz University for Health Sciences, Jeddah, Saudi Arabia

⁷King Abdullah International Medical Research Center, Jeddah, Saudi Arabia

Correspondence should be addressed to Faleh Alqahtani; afaleh@ksu.edu.sa and Imran Imran; imran.ch@bzu.edu.pk

Received 13 August 2020; Revised 23 November 2020; Accepted 1 December 2020; Published 12 December 2020

Academic Editor: Monica Fedele

Copyright © 2020 Faleh Alqahtani et al. This is an open access article distributed under the Creative Commons Attribution License, which permits unrestricted use, distribution, and reproduction in any medium, provided the original work is properly cited.

Traumatic brain injury (TBI) is among the most debilitating neurological disorders with inadequate therapeutic options. It affects all age groups globally leading to post-TBI behavioral challenges and life-long disabilities requiring interventions for these health issues. In the current study, C57BL/6J mice were induced with TBI through the weight-drop method, and outcomes of acutely administered ketamine alone and in combination with perampanel were observed. The impact of test drugs was evaluated for post-TBI behavioral changes by employing the open field test (OFT), Y-maze test, and novel object recognition test (NOR). After that, isolated plasma and brain homogenates were analyzed for inflammatory modulators, i.e., NF- κ B and iNOS, through ELISA. Moreover, metabolomic studies were carried out to further authenticate the TBI rescuing potential of drugs. The animals treated with ketamine-perampanel combination demonstrated improved exploratory behavior in OFT ($P < 0.05$), while ketamine alone as well as in combination yielded anxiolytic effect ($P < 0.05-0.001$) in posttraumatic mice. Similarly, the % spontaneous alternation and % discrimination index were increased after the administration of ketamine alone ($P < 0.05$) and ketamine-perampanel combination ($P < 0.01-0.001$) in the Y-maze test and NOR test, respectively. ELISA demonstrated the reduced central and peripheral expression of NF- κ B ($P < 0.05$) and iNOS ($P < 0.01-0.0001$) after ketamine-perampanel polypharmacy. The TBI-imparted alteration in plasma metabolites was restored by drug combination as evidenced by metabolomic studies. The outcomes were fruitful with ketamine, but the combination therapy proved more significant in improving all studied parameters. The benefits of this new investigated polypharmacy might be due to their antigitamatergic, antioxidant, and neuroprotective capacity.

1. Introduction

Traumatic brain injury (TBI) is one of the most common reasons behind neurological impairment that continues to distress the masses of the population worldwide. The Centre

for Disease Control (CDC) reports that the rate of hospital visits and deaths due to TBI has been continuously increasing with time [1]. The affectees belong to different age groups including children (<5 y), adolescents (16-25 y), and elderly (>60 y) due to accidental collision with some object during

falls or traffic-related misfortunes [2]. It can be considered as the “silent epidemic” due to its contribution towards morbidity and mortality worldwide [3]. The brain insult in TBI patients is extensively associated with life-long disabilities as inadequate therapeutic options cannot deal with the array of consequences. Unfortunately, the rehabilitation of such disabled patients places a financial burden on affected families as well as on overall healthcare [4].

Several studies through animal models have demonstrated the deleterious impact of TBI on quality of life due to deteriorated reasoning and learning capabilities [5]. The pathophysiology of TBI can be divided into primary and secondary phases [6]. The primary phase comprises the direct mechanical injury to the brain that damages the cellular membranes, subcellular structures, and blood vessels thus altering cerebral blood flow due to hemorrhage and increased cell death due to ischemia [7]. These events lead to the activation of immune cells residing in the brain, i.e., microglia and astrocytes causing further initiation of inflammation through cytokines and chemotaxis [8].

Nitric oxide (NO) is an inflammatory product that takes part in secondary TBI [9] as well as in the recovery phase [10]. Its detrimental or beneficial role is decided by the site [11], quantity [12], and time [13] of its production. It is synthesized by three isoforms of NOS among which a Ca^{+2} -independent type, inducible nitric oxide synthase (iNOS), is not expressed in the brain under normal circumstances. However, any kind of stimuli, i.e., inflammation, injury, or hypoxia, causes the activation of iNOS in neurons and glial cells. In response to certain proinflammatory cytokines, overexpression of iNOS is seen in vascular smooth muscle cells and stimulated macrophages [14] resulting in increased production of NO which causes increased leukocyte accumulation in the brain from 4 h to 7 days of TBI [15]. Gene expression of iNOS requires activation of the transcriptional factor NF- κ B [16] which plays a role in inflammation and immunity in the CNS. The previously reported studies demonstrate that inhibition of NF- κ B signaling cause reduced inflammation and enhanced neuroprotection in animal models of TBI [17, 18]. Besides these, stimulated microglia cause damage to oligodendrocytes and neurons via expression of iNOS [19]. Various clinical and experimental studies have observed elevated NO levels and overexpression of iNOS in TBI [20]. Furthermore, inhibition of iNOS also resulted in significantly improved clinical outcomes thus suggesting the neuroprotective role of iNOS inhibition after TBI [21].

Another offender of TBI is glutamate, a principal excitatory neurotransmitter in the brain, which [22] plays a crucial role in the pathophysiology of brain trauma during the second phase [23]. Studies have revealed that the raised glutamate levels in humans facing TBI may persist for days or weeks in certain parts of the brain [24]. Increased levels of glutamate after brain trauma cause excitotoxicity resulting in neuronal damage and death and if not regulated can lead to long-term cognitive decline and motor dysfunction [25]. Mostly, the excitatory neurotransmission in the brain is facilitated by AMPA and NMDA receptors and their altered expression is seen in pathological signaling happening during

various disease states including TBI [26]. Hence, targeting these receptors can be a therapeutic option for management of brain trauma. Perampanel, marketed as Fycompa, is a noncompetitive antagonist of AMPA receptor [27] and has demonstrated the neuroprotective role in controlled cortical impact model of TBI due to anti-inflammatory and antioxidant potential [26]. Besides this, antagonism of AMPA receptor has been reported to improve cognition and behaviors in rats with TBI [28].

NMDA receptors have been targeted by numerous anesthetic agents, including ketamine. Antagonism of NMDA receptor by ketamine has also been postulated to exert neuroprotection in TBI [29]. Ketamine is also reported to inhibit NO synthesis thus exerting vasoconstrictive impact resulting in hemodynamic stability [30]. It has also shown to affect hippocampal cell proliferation after TBI leading to neurogenesis which led to better learning and behavior in mice with TBI [31].

In this recent study, we examined the therapeutic outcomes of coadministration of perampanel and ketamine in the management of TBI as it has never been addressed previously. Some behavioral experiments were also employed to examine the role of polypharmacy on the cognitive deficit in the mouse model of weight-drop TBI, whereas their impact on local and systemic inflammation was estimated through their effect on iNOS and NF- κ B levels. The scientific findings were further evaluated through metabolomics of the animal plasma. We hypothesized the beneficial outcomes by combination therapy of perampanel-ketamine on local and systemic inflammation as well as on behavioral adversity seen in TBI.

2. Materials and Methods

2.1. Animal. Healthy male C57BL/6J mice of 8-10 weeks (24-28 g) were utilized in this study. The animals were housed in standardized maintenance conditions, i.e., 12 h L/D cycle, 25°C temperature, and provided with free excess of water and a standard mouse chow. The whole animal study was carried out after ethical permission granted by the Research Ethics Committee (REC), King Saud University, KSA, through reference no. KSU-SE-19-51.

2.2. Animal Grouping and Experimental Design. 44 animals were randomly divided into five groups ($n = 8/9$) comprising TBI animals treated with vehicle only (Group I), TBI animals treated with ketamine only (Group II), TBI animals treated to a combination of ketamine and perampanel treatment (Group III), sham animals were given vehicle only (Group IV), and sham animals treated with ketamine and perampanel (Group V).

On the 1st day, animals were brought to the experimental room and acclimatized to this new environment for a few hours. Later, they were induced with brain injury by the weight drop method followed by group-wise-specific treatments after 30 minutes of the injury.

Animals of the vehicle-treated group were treated with normal saline only while ketamine (40 mg/kg, i.p.) and perampanel (4 mg/kg, p.o.) were given to the aforementioned

groups. The doses of drugs and routes of administration were decided on the basis of previously reported studies related to ketamine [32, 33] and perampanel [34, 35].

On the 2nd day, after 24 h of TBI induction and subsequent treatments, the general locomotor activity was examined through the open field test. Afterward, the Y-maze and novel object recognition tests were performed on the 3rd and 4th day, respectively, to assess their learning and memory. Immediately after the completion of the behavioral test on the 4th day, blood and brain samples were collected from randomly chosen animals. The blood samples were utilized for plasma estimation of NF- κ B and iNOS to check the impact of test drugs on systemic inflammation, while the brain homogenates were prepared to investigate the role of ketamine and perampanel on local inflammatory response after TBI (Figure 1).

2.3. Materials. Perampanel (Fycopma, 8 mg) and ketamine (Tekam, 10 mg/ml) were purchased from Eisai Co., Ltd. and Hikma Pharmaceuticals, respectively. Methoxyamine hydrochloride, pyridine, N,O-Bis(trimethylsilyl)trifluoroacetamide (BSTFA), and chlorotrimethylsilane (TMCS) were purchased from Sigma-Aldrich, St. Louis, MO, USA. Hexane and methanol were purchased from BDH VWR International Ltd. Poole, BH 15 1TD, England. Deionized water was obtained with Milli-RO and Milli-Q Plus instrumentation from Millipore, Billerica, MA, USA.

2.4. Induction of Brain Injury. Inducing brain trauma by the weight-drop method is well known for imitating human closed-head injury [36]. Thus, we employed this model of TBI in which severity of trauma can be controlled by adjusting the mass of weight and height from which it falls. The model utilized a weight-drop device that causes focal blunt trauma to one side of the unprotected skull. This results in damage to BBB and initiation of the neuroinflammatory cascade which collectively yields neurological deficit and behavioral impairment.

Initially, mice were exposed to isoflurane vapors (2-4 minutes) for anesthesia. The head of the animal was positioned on a platform under the device to direct the trauma from the left anterior frontal area at the same distance between the eye and the ear. A metallic mass of 30 g was guided through a hollow tube to fall freely on the targeted point from a height of 80 cm [37].

2.5. Behavioral Studies

2.5.1. Open Field Test. The open field test is widely employed to evaluate the general exploratory activity in mice as they instinctively try to explore the open areas [38]. The test was conducted in a square-shaped (16" \times 16") glass apparatus equipped with infrared sensors and perimeter. Mice were placed in this chamber and were allowed to acclimatize for 20 min to this environment. Afterward, their locomotion was recorded for 10 minutes to evaluate the total distance traveled and their preference for open areas of apparatus was evaluated to estimate the TBI-induced anxiety behavior in mice.

2.6. Behavioral Tests for Memory and Learning

2.6.1. Y-Maze Test. In the Y-maze test, the animal's cognitive capacity is evaluated by monitoring its willingness to visit a new arm of maze and remembering the previously visited arm [39]. The test apparatus comprises three closed arms (35 cm \times 5 cm \times 10 cm) designed closely at 120°. The mice were placed separately in the center of the maze facing one of three arms (A, B, and C) keeping the apparatus cleaned with 70% alcohol after each animal's trial. The individual mouse was allowed to explore the maze for 5 minutes, and the sequence of the arm visits (ABC, BAC, CAB, etc.) was recorded to calculate the % spontaneous alternation behavior. An increased %SAP is an indication of better cognition and memory in rodents.

% spontaneous alternation was calculated by the following formula [40]:

$$\begin{aligned} & \% \text{Spontaneous alternation} (\% \text{SAP}) \\ & = \left[\frac{\text{Number of alternations}}{\text{Total arm entries} - 2} \right] \times 100. \end{aligned} \quad (1)$$

2.6.2. Novel Object Recognition Test. This test is based on characteristics of the rodent to explore new environments and is extensively acknowledged to estimate their cognitive function. The animal with efficient memory recognizes the previously explored familiar object and expresses a spontaneous tendency to discover the new one. The test was conducted in a transparent acrylic glass box (16" \times 16") in which animals were tested individually. Initially, each mouse was given 5 minutes to get familiar with the environment. After that, in the training phase, two geometrically identical objects were placed in the test box and the mouse was allowed to discover them for 10 min by touching and smelling them. Later, one of these two objects was replaced by a novel object of a different shape in test trial. The time spent with novel and familiar objects was recorded for 5 minutes to calculate the discrimination index:

Discrimination index

$$= \left[\frac{\text{Time with novel object} - \text{Time with familiar object}}{\text{Time with novel object} + \text{Time with familiar object}} \right]. \quad (2)$$

2.7. Blood Collection for Plasma Analysis. Soon after completion of the novel object recognition test, the blood of randomly taken animal ($n = 3$ per group) was collected in clean glass tubes through cardiac puncture. The blood samples were centrifuged at 3,000 rpm (800 g) for 10 min to separate the plasma to be analyzed which was stored at -80°C till further analysis [41].

Plasma levels of iNOS and NF- κ B were assessed through the commercially available ELISA kits and developed according to the manufacturer's protocols (iNOS ELISA Kit Cat. No. R6663, TSELISA, Biotang Lab Supplier, USA; NF- κ B ELISA Kit Cat. No. 85-86081-11, Thermo Fisher Scientific,

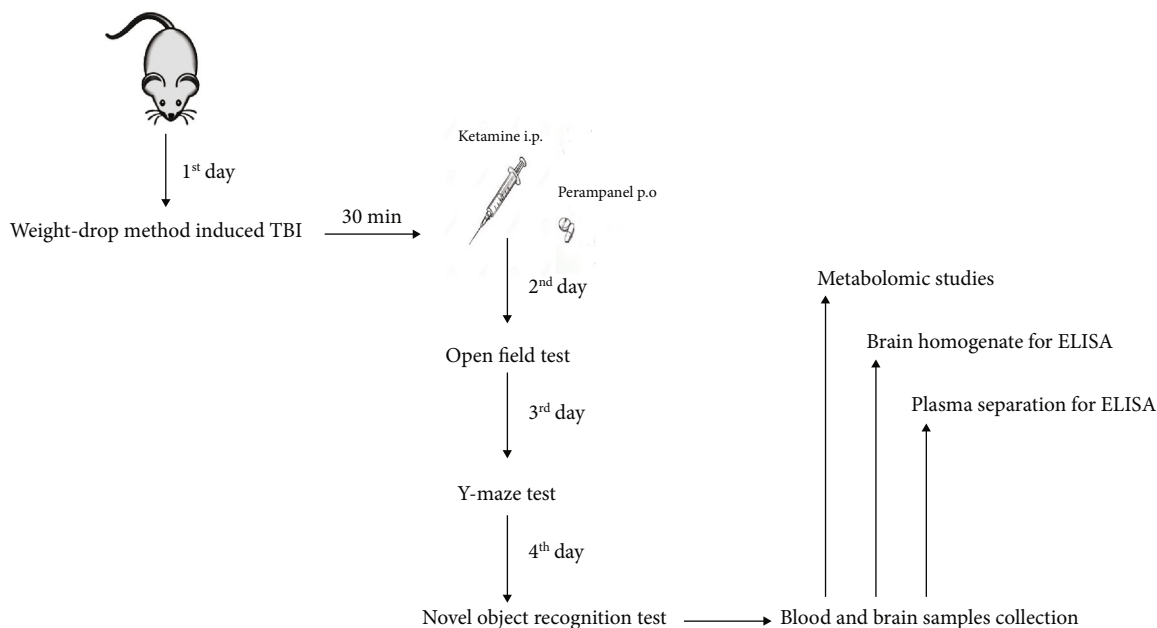


FIGURE 1: Experimental design depicting day-wise behavioral studies with subsequent in vitro analysis.

USA) for assessment of TBI and test treatment on their systemic expression.

2.8. Preparation of Brain Homogenate. After anesthetization with isoflurane, the brains of randomly selected animals ($n = 3$ per group) were dissected out and stored at 8°C in normal saline. 0.5 g of the brain was homogenized in 5 ml of phosphate buffer (pH 7.4) through centrifugation at $12,000\text{ g}$ for 15-20 minutes maintaining the low temperature of the mixture [42]. The resulting homogenized solution was evaluated through ELISA for any fluctuation in brain levels of inflammatory modulators, i.e., $\text{NF-}\kappa\text{B}$ and iNOS, after traumatic brain injury and the impact of test drugs on these TBI-induced consequences.

2.9. Metabolomic Analysis. Metabolomic analysis was done with slight modifications in the method described [43]. The plasma samples were thawed at room temperature and vortex for 2 min. $100\ \mu\text{l}$ of this sample was put in the Eppendorf tube and $300\ \mu\text{l}$ of methanol and $100\ \mu\text{l}$ of Milli-Q water were added. Vortex again for 2 min and centrifuge for $10,000\text{ rpm}$ for 10 min at 4°C . From the supernatant solution, pipette out $200\ \mu\text{l}$ of sample and transfer it to a GC-MS vial. Purge the solution with nitrogen air to completely dry the vial. After this process, methoxylation was carried out at room temperature by adding $100\ \mu\text{l}$ of methoxyamine hydrochloride in pyridine solution (15 mg ml^{-1}). The mixture was vortexed for 10 min and put the sample for half an hour at room temperature. In the second step, the methoxylated sample underwent a derivatization reaction by using $100\ \mu\text{l}$ of BSTFA/TMCS (99/1, v/v) and vortexed again for 10 min and kept for 2 hours at 50°C to complete the derivatizing reaction. $1\ \mu\text{l}$ of the derivatized sample was injected into the system with the split mode (split ratio 1 : 20).

A PerkinElmer model Clarus 600 T combined with a single quadrupole mass spectrometer was used for GC-MS analysis. The chromatographic column was an Elite 5MS column ($30\text{ m} \times 0.25\text{ mm} \times 0.25\ \mu\text{m}$ film thickness), with high-purity helium as the gas carrier, at a flow rate of 1 ml/min . The injector temperature was 280°C and it was equipped with a splitless injector at 20:1. The temperature was set initially to 40°C (held for 2 min), was increased to 150°C at $10^{\circ}\text{C min}^{-1}$ (held for 2 min), and then increased further to 300°C at $10^{\circ}\text{C min}^{-1}$ (held for 2 min). The MS ion source temperature was 220°C , and inlet line temperature was at 240°C . The scan range was set at 40 to 600 mass ranges at 70 eV electron energy and the solvent delay of 7 min. Finally, unknown compounds were identified by comparing the spectra with that of the NIST 2005 (National Institute of Standard and Technology Library) and Wiley 2006 Library. The total time required for analyzing a single sample was 32 minutes.

2.10. Statistical Analysis. Data were analyzed through one-way ANOVA using GraphPad Prism 9 Software Inc. (La Jolla, CA, USA) followed by Sidek's or Dunnett's post hoc test. All arithmetic values were expressed as the mean \pm SD considering $P < 0.05$ as statistically significant. Metabolomic data were analyzed via two-way ANOVA data that were presented as the mean \pm SEM.

3. Results

3.1. Behavioral Analysis

3.1.1. Effect of Administration of Ketamine Alone and in Combination with Perampanel on General Exploration and Anxiety after Traumatic Brain Injury. Animals with traumatic brain injury demonstrated lesser exploration of test apparatus than healthy mice ($P < 0.01$) and to those healthy

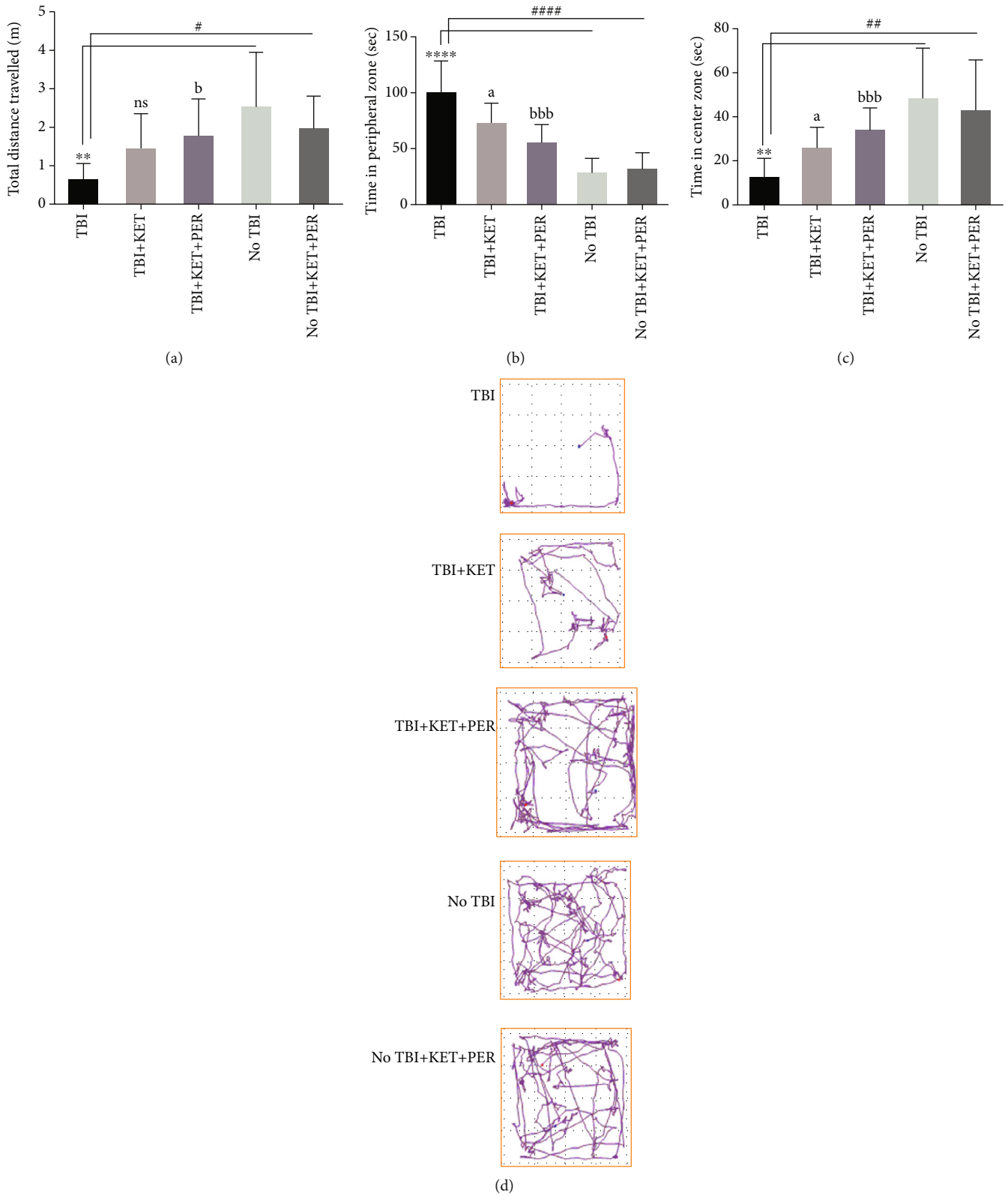


FIGURE 2: Comparison of total distance traveled (a), time spent in peripheral zone (b), time spent in central zone (c), and tracings of general exploratory behavior (d) among different groups in the open field test. ** $P < 0.01$ and **** $P < 0.0001$ show comparisons b/w TBI mice with healthy ones receiving vehicle only. # $P < 0.05$, ## $P < 0.01$, and ### $P < 0.0001$ show comparisons b/w TBI mice with healthy ones exposed to ketamine-perampanel combination. ^a $P < 0.05$ shows comparison b/w TBI mice with the TBI mice treated with ketamine only. ^b $P < 0.05$ and ^{bbb} $P < 0.0001$ show comparisons b/w TBI mice with TBI mice treated with ketamine-perampanel combination. All data are expressed as the mean \pm SD ($n = 8/9$ animals per group).

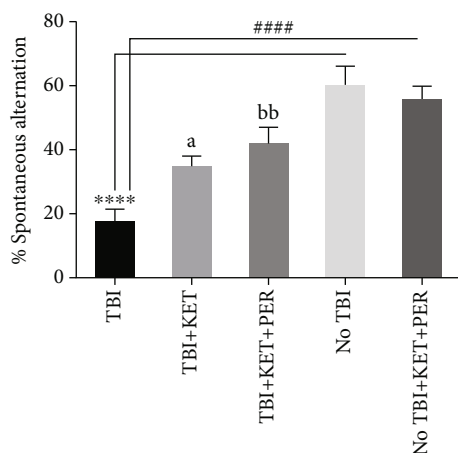


FIGURE 3: Comparison of % spontaneous alternation behavior among different groups in the Y-maze test. **** $P < 0.0001$ shows comparisons b/w TBI mice with healthy ones receiving vehicle only. #### $P < 0.0001$ shows comparisons b/w TBI mice with healthy ones exposed to ketamine-perampanel combination, ^a $P < 0.05$ shows comparison b/w TBI mice with the TBI mice treated with ketamine only. ^{bb} $P < 0.01$ shows comparisons b/w TBI mice with TBI mice treated with ketamine-perampanel combination. All data are expressed as the mean \pm SD ($n = 8/9$ animals per group).

mice treated with KET+PER ($P < 0.05$) revealing the brain trauma-induced motionlessness in animals (Figure 2(d)). However, the administration of KET+PER reversed these outcomes as total distance traveled was notably increased ($P < 0.05$) than TBI mice. However, the administration of ketamine did not yield significant outcomes on exploration (Figure 2(a)).

However, TBI caused animals to act anxiously as they displayed partialities towards marginal areas of the field and spent more time their ($P < 0.0001$) than the central zone ($P < 0.01$). Interestingly, the anxiety was reduced through the administration of ketamine as animals spent more time in the central ($P < 0.05$) and less time in peripheral ($P < 0.05$) zones of test apparatus. The outcomes were even more pronounced on the administration of KET+PER as the animals were unafraid and preferred center zone ($P < 0.001$) over the peripheral zone as compared to TBI mice (Figures 2(b) and 2(c)).

3.1.2. Effect of Administration of Ketamine Alone and in Combination with Perampanel on TBI-Induced Cognitive Deficit in the Y-Maze Test. The Y-maze test was employed to evaluate the influence of investigational drugs on cognitive decline in TBI mice. The mice were not capable enough of recalling the previously visited arm of maze due to neuronal damage resulting from physical injury to the brain. The experimental outcomes demonstrated memory scarcity as evident from reduced alternation behavior ($P < 0.0001$) than both groups of healthy mice. This cognitive deficit was improved when animals were treated with ketamine ($P < 0.05$) and ketamine-perampanel combination ($P < 0.01$) showing that the treatments led to improved spatial remembrance as they

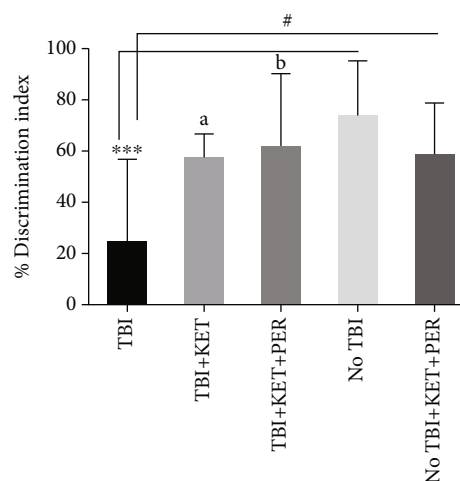


FIGURE 4: Comparison of % discrimination index among different groups in the novel object recognition test. *** $P < 0.001$ shows comparisons b/w TBI mice with healthy ones receiving vehicle only. # $P < 0.05$ shows comparisons b/w TBI mice with healthy ones exposed to ketamine-perampanel. ^a $P < 0.05$ shows comparison b/w TBI mice with the TBI mice treated with ketamine only. ^b $P < 0.05$ shows comparisons b/w TBI mice with TBI mice treated with ketamine-perampanel combination. All data are expressed as the mean \pm SD ($n = 8/9$ animals per group).

significantly reversed the intellectual impairment in mice resulting from TBI (Figure 3).

3.1.3. Effect of Administration of Ketamine Alone and in Combination with Perampanel on TBI-Induced Cognitive Deficit in the Novel Object Recognition Test. This test was used to evaluate the memory of mice exposed to brain trauma and the impact of investigational treatments on their behavior. The mice with TBI revealed poor intellect as they could not retain the memory of the familiar object and exhibited lower discrimination index as compared to vehicle-treated ($P < 0.001$) and ketamine-perampanel-treated ($P < 0.05$) healthy mice. This cognitive deficit was significantly improved on exposure to ketamine ($P < 0.05$) and ketamine-perampanel combination ($P < 0.05$) as animals retained the familiarity of previously explored objects and preferred the novel one (Figure 4).

3.2. Effect of Administration of Ketamine Alone and in Combination with Perampanel on Plasma Levels of NF- κ B and iNOS after Traumatic Brain Injury. Plasma levels of NF- κ B were estimated to check the impact of test drugs on this proinflammatory mediator as it acts as a cofactor in transcription and signaling pathways in systemic inflammation after some injury. In the current study, ELISA exposed the elevated levels of NF- κ B after TBI as compared to healthy animals ($P < 0.01$) and to those healthy mice treated with ketamine-perampanel combination ($P < 0.01$). These TBI-elevated plasma concentrations of NF- κ B were reduced significantly in mice treated with ketamine ($P < 0.05$) and with ketamine-perampanel combination ($P < 0.05$) (Figure 5(a)). Similarly, plasma levels of iNOS were also increased in TBI mice ($P < 0.0001$) as brain injury is also known to increase

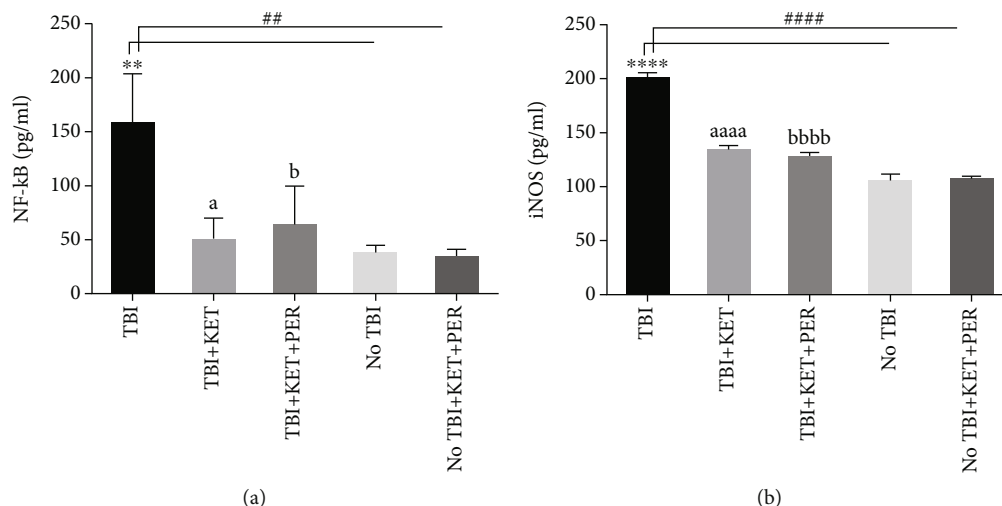


FIGURE 5: Comparison of plasma levels of NF-κB (a) and iNOS (b) among differently treated groups through ELISA. $**P < 0.01$ and $****P < 0.0001$ show comparisons b/w TBI mice with healthy ones receiving vehicle only. $##P < 0.01$ and $####P < 0.0001$ show comparisons b/w TBI mice with healthy ones exposed to ketamine-perampanel. $^aP < 0.05$ and $^{aaaa}P < 0.0001$ show comparison b/w TBI mice with the TBI mice treated with ketamine only. $^bP < 0.05$ and $^{bbbb}P < 0.0001$ show comparisons b/w TBI mice with TBI mice treated with ketamine-perampanel combination. All data are expressed as the mean \pm SD ($n = 3$ animals per group).

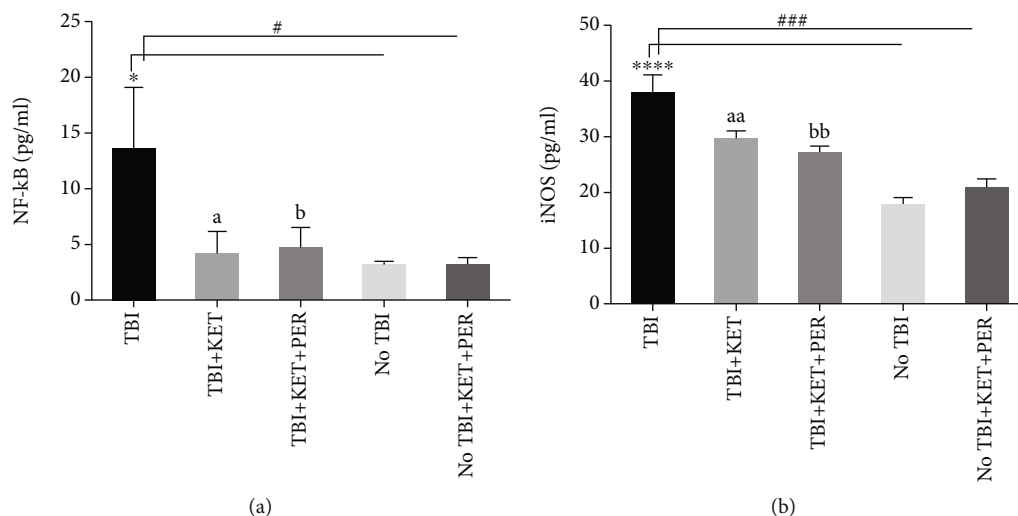


FIGURE 6: Evaluation of concentration of NF-κB (a) and iNOS (b) in the brains of differently treated groups after traumatic brain injury. $*P < 0.05$ and $****P < 0.0001$ show comparisons b/w TBI mice with healthy ones receiving vehicle only. $^#P < 0.05$ and $^{###}P < 0.001$ show comparisons b/w TBI mice with healthy ones exposed to ketamine-perampanel. $^aP < 0.05$ and $^{aa}P < 0.01$ show comparison b/w TBI mice with the TBI mice treated with ketamine only. $^bP < 0.05$ and $^{bb}P < 0.01$ show comparisons b/w TBI mice with TBI mice treated with ketamine-perampanel combination. All data are expressed as the mean \pm SD ($n = 3$ animals per group).

the inflammatory NO in distant organs as well as to yield further complications after initial injury. However, the administration of ketamine reversed ($P < 0.001$) these detrimental outcomes of TBI (Figure 5(b)) and the parallel result was seen in animals treated with ketamine-perampanel combination ($P < 0.0001$).

3.3. Effect of Administration of Ketamine Alone and in Combination with Perampanel on Concentration of NF-κB and iNOS in the Brain after Traumatic Brain Injury. ELISA revealed the raised levels of NF-κB in the brain after a trau-

matic injury as compared to healthy brains ($P < 0.05$), and these detrimental outcomes were resolved after treatment with ketamine alone ($P < 0.05$) and in combination with perampanel ($P < 0.05$) (Figure 6(a)).

Likewise, iNOS expression was also enhanced in the brains of the TBI group as compared to the brains dissected from healthy mice receiving no treatment ($P < 0.0001$) and receiving ketamine-perampanel ($P < 0.001$). This elevated expression of iNOS was normalized when TBI mice were treated with ketamine ($P < 0.01$) and ketamine-perampanel combination ($P < 0.01$) (Figure 6(b)).

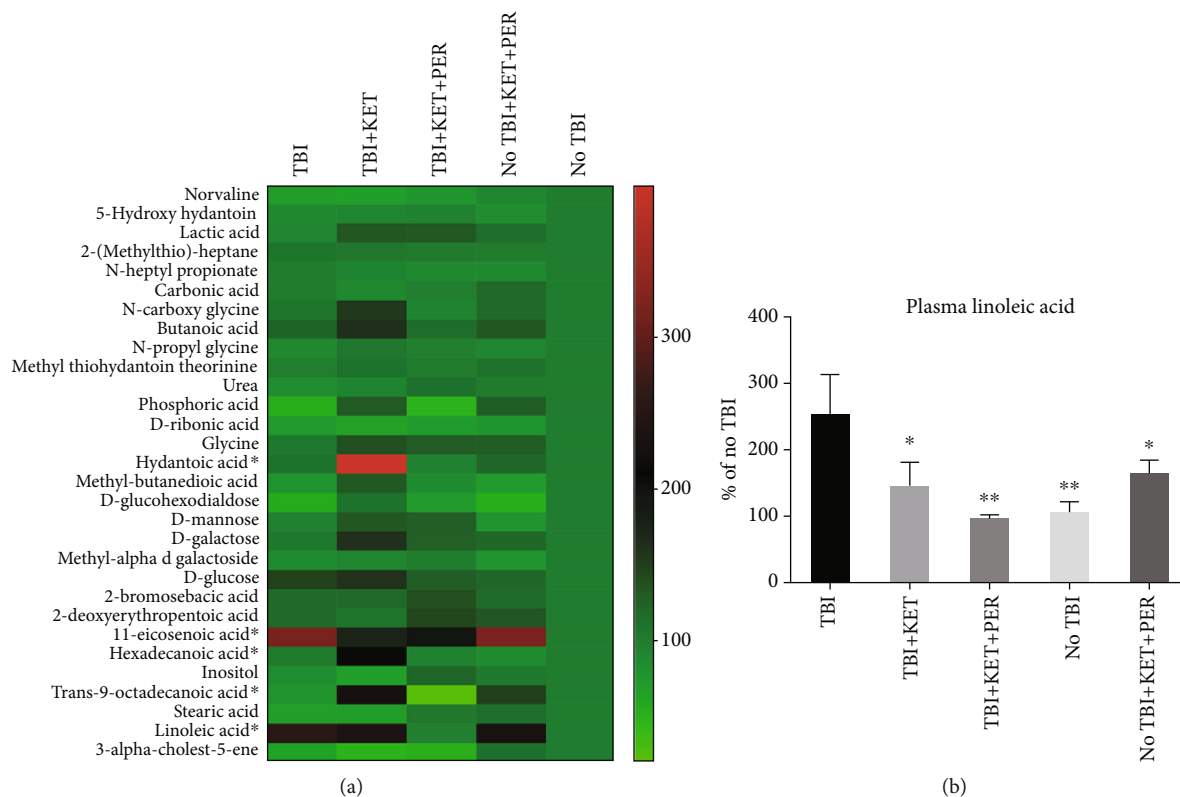


FIGURE 7: Plasma metabolomic analysis. A heat map shows thirty identified plasma metabolites (a) and differences in plasma concentrations of linoleic acid (b). The statistically significant changed metabolites were labeled bold on the heat map (a). All data are expressed as the mean \pm SEM ($n = 3-4$). Outcomes of all groups were compared with the No TBI group which is assumed 100%, and comparative statistical significance * $P < 0.05$ was compared with the TBI group. Two-way ANOVA analysis of normalized values (as percentage of the No TBI group). * $P < 0.05$ and ** $P < 0.01$ (Supplementary Raw Data).

3.4. Outcomes of Administration Combination Therapy on with Perampanel on Metabolomics. The plasma metabolomic profile was assessed to further explore the effect of our treatment on TBI. Thirty metabolites were found (Figure 7(a)), which are linked to various pathways including galactose metabolism, biosynthesis of unsaturated fatty acids, amino sugar, and nucleotide sugar metabolism. To assess the differences between our groups, two-way ANOVA was performed to statistically identify the differences between our groups. Among these thirty, five metabolites were significantly changed among groups including hydantoic acid, 11-eicosenoic acid, hexadecanoic acid, trans-9-octadecanoic acid, and linoleic acid revealing uniqueness in its metabolomic profile of each group. However, linoleic acid was the one that got significantly increased after TBI and this outcome was prominently neutralized by combination therapy (Figure 7(b)) suggesting its role in the findings of our study.

4. Discussion

Traumatic brain injury affects millions of people every year through continual disabilities and mortalities in almost all age groups from all over the world [44]. Epidemiological estimations predict that TBI-resulted ceaseless debilitation rate will leave the other ailment-imparted incapacities behind in the coming decade [45]. Unfortunately, the current advancement in trauma research through the collaboration of multi-

disciplinary professionals is still insufficient to handle this challenge and TBI continues to be a major burden on global health and patient's income.

After any physical damage to the brain, the gradual pathophysiological fluctuations take place continuously resulting in reduced blood flow and oxygenation of brain tissues leading to BBB damage and edema [46]. The second phase of damage causes more worsening of neurological function and may start after minutes or weeks to primary injury. Various pathways that play a role in this biphasic damage are the excessive release of glutamate, generation of free radicals due to mitochondrial dysfunction, and neuroinflammation due to local and systemic immunooactivation [47].

The amino acid glutamate is released at up to half of synapses in the brain and is known as the main excitatory neurotransmitter in the CNS which can act as excitotoxin as of NMDA and AMPA receptors can result into neuronal damage. Currently, glutamatergic storming is accepted to play a critical role in grading the severity of TBI [23]. Ketamine attenuates this excitotoxicity by exhibiting the noncompetitively antagonizing NMDA receptor. Furthermore, it also improves cerebral vascular flow at subanesthetic doses and addresses the root cause of excitotoxicity [48]. Ketamine also causes inhibition of neurotoxic NR2B-comprising NMDA receptors and this plays a friendly role in neuronal regeneration [49]. On the other side, perampanel rescues the tissue from damage by antagonizing the AMPA-induced increases

in intracellular Ca^{2+} which plays a role in glutamatergic storming [50]. It also plays anti-inflammatory action by suppressing the expression of $\text{TNF-}\alpha$ and $\text{IL-1}\beta$ (proinflammatory cytokines) and enhancing the expression IL-10 and $\text{TGF-}\beta 1$ (anti-inflammatory cytokines) [26]. These might be the mechanisms through which the ketamine and perampanel reversed the deteriorating effects of TBI.

The brain is highly susceptible to oxidative stress due to its high content of polyunsaturated lipids. As physical trauma results in impaired circulation and oxygenation of the brain, there is an increased generation of ROS including nitric oxide and superoxide [51]. Peroxynitrite is another strong oxidant generated due to the reaction of nitric acid with superoxide and causes further impairment in cerebral vascular function after TBI [52]. This process depletes the natural antioxidants and peroxidation of lipid membrane and disruption of mitochondrial electron transport system results in necrosis and apoptosis. The Nrf2 pathway has been known as a cellular defense mechanism against oxidative stress that works by upregulating the phase II enzymes [53]. Ketamine administration after TBI exerts a neuroprotective role by combating the oxidative stress through a significant increase in Nrf2 expression [33]. Additionally, a study has reported the beneficial effect of perampanel through inhibition of lipid peroxidation and preservation of endogenous antioxidant reservoirs that work to inhibit TBI-induced oxidative stress [26].

Local tissue injury can provoke the inflammation through iNOS expression in cells of vascular smooth muscles [54] as well as in brain immune cells and endothelial cells at BBB [55]. The macrophages expressing iNOS can play a role in the activation of inflammatory events leading to dysfunction of the blood-brain barrier, and these consequences contribute to the second phase of TBI [56]. The regulation of iNOS takes place at the transcriptional level, and the promoter region of iNOS gene contains various binding sites for transcriptional factors including $\text{NF-}\kappa\text{B}$ [57]. In our study, treatment of TBI mice with ketamine and ketamine-perampanel combination demonstrated a significant reduction in local and systemic expression of $\text{NF-}\kappa\text{B}$ and iNOS. This might be due to the antioxidant potential of ketamine [33] and perampanel [26] as oxidative stress plays a crucial role in the activation of $\text{NF-}\kappa\text{B}$ in different cell types [57].

Though a range of behavioral changes is seen as post-TBI difficulties, impaired cognition and deteriorated learning are commonest consequences [58]. In the present study, the TBI mice exhibited impaired memory by demonstrating reduced alternation behavior in the Y-maze and poor object identification in the novel object recognition test. However, these outcomes were improved by ketamine and ketamine-perampanel combination. Similarly, the animal testing through the open field test revealed that TBI mice stayed stationary and anxious with less exploration of field and avoidance of open areas of apparatus. Treatment with ketamine-perampanel combination improved the TBI-deteriorated behavior, and animals showed improved learning and fearlessness.

Various studies have reported the association of increased ROS and anxiety [59, 60]. Oxidative stress also

results in cognitive decline as seen in the normal aging process too [61]. Ketamine and perampanel drugs impart an inhibitory effect on $\text{NF-}\kappa\text{B}$ leading to reduced iNOS expression [62]. These antioxidant influences of test drugs can be the mechanism through which they improved outcomes in the behavioral tests. Besides this, ketamine is known to alter hippocampal cell proliferation as NMDARs play a role in modulating neurogenesis after TBI [31]. Additionally, perampanel is also reported to exert the cognition-boosting effect by reduced neuronal apoptosis [26].

Linoleic acid is one of the major polyunsaturated fatty acids (PUFA) in mammals which acts as a substrate for lipoxygenase [63], and the lipid mediators produced are reported to implicate BBB damage, activation of inflammatory reactions, and dysregulated cerebral flow [64]. It can be nonenzymatically autoxidized to its hydroperoxides that work as a source of massive oxidation damaging reactions in the biological systems [65]. GC/MS-based nontargeted metabolomics conducted on separated plasma revealed the elevated level of linoleic acid after acute TBI as previously reported as well [43]. Linoleic acid is the part of membrane phospholipids [66] and its elevated levels were reduced by ketamine-perampanel combination illustrating their role to reduce the damage to the cellular membrane either through combating the excitotoxicity or exerting an antioxidant effect.

5. Conclusion

In the present study, the administration of a subanesthetic dose of ketamine alone and in combination with perampanel showed retrieval from a post-TBI behavioral deficit in C57BL/6J mice. The TBI-resulted overexpression of local and systemic inflammatory modulators, $\text{NF-}\kappa\text{B}$ and iNOS, was positively regulated by test drug combination as well as ketamine alone. Furthermore, metabolomic studies also supported the neuroprotective impact of therapy as the reversal of metabolic changes was observed. These beneficial outcomes might go through antagonizing the glutamatergic storming or through suppressing the local as well as systemic expression of $\text{NF-}\kappa\text{B}$ and iNOS. The study unveiled the rescuing effect of the NMDA receptor antagonist, ketamine, on TBI, and the outcomes were even much improved by combining it with the AMPA receptor antagonist, perampanel. This newly investigated polypharmacy could be used as a therapeutic approach in the management of traumatic brain injury.

Data Availability

The raw data used to support the findings of this study are available from the corresponding author upon request.

Conflicts of Interest

The authors declare that they have no conflict of interests.

Acknowledgments

Thanks to the two B. Pharm students (Azzam Saleh AlZogaibi and Nawaf Abdulaziz Alrashed) affiliated to the College of Pharmacy at King Saud University, Riyadh, Saudi Arabia) for their help as caretakers subsequent to TBI induction. We are thankful to Dr. Syed Rizwan Ahamad from the Central Laboratory, College of Pharmacy, King Saud University, Riyadh, Saudi Arabia, for his help in processing the samples for metabolic results. We are thankful to Mr. Waqar Ahmad and Mr. Muhammad Suhaib Afzal from the Department of Pharmacology, Bahauddin Zakariya University, Multan, for analyzing the behavioral videos on ANY-maze behavioral tracking software. The authors extend their appreciation to the Deanship of Scientific Research at King Saud University for funding this work through research group No. RG-1441-340.

References

- [1] É. Jean-Louis, "Traumatic brain injury," *L'Aide-Soignante*, vol. 30, no. 173, pp. 31-32, 2016.
- [2] Centers for Disease Control and Prevention, *TBI: Get the Facts Concussion Traumatic Brain Injury CDC Injury Center*, U.S. Department of Health & Human Services, 2019, https://www.cdc.gov/traumaticbraininjury/get_the_facts.html.
- [3] M. C. Dewan, A. Rattani, S. Gupta et al., "Estimating the global incidence of traumatic brain injury," *Journal of Neurosurgery*, vol. 130, no. 4, pp. 1080-1097, 2019.
- [4] GBD 2016 Traumatic Brain Injury and Spinal Cord Injury Collaborators, "Global, regional, and national burden of traumatic brain injury and spinal cord injury, 1990-2016: a systematic analysis for the Global Burden of Disease Study 2016," *The Lancet Neurology*, vol. 18, no. 1, pp. 56-87, 2019.
- [5] H. Dawish, A. Mahmood, T. Schallert, M. Chopp, and B. Therrien, "Mild traumatic brain injury (MTBI) leads to spatial learning deficits," *Brain Injury*, vol. 26, no. 2, pp. 151-165, 2012.
- [6] J. C. Huffman, M. M. Brennan, F. A. Smith, and T. A. Stern, "Patients with neurologic conditions I. Seizure disorders (including nonepileptic seizures), cerebrovascular disease, and traumatic brain injury," in *Massachusetts General Hospital Handbook of General Hospital Psychiatry*, pp. 237-253, Mosby, 2010.
- [7] P. Kaur and S. Sharma, "Recent advances in pathophysiology of traumatic brain injury," *Current Neuropharmacology*, vol. 16, no. 8, pp. 1224-1238, 2018.
- [8] M. L. Kelso and H. E. Gendelman, "Bridge between neuroimmunity and traumatic brain injury," *Current Pharmaceutical Design*, vol. 20, no. 26, pp. 4284-4298, 2014.
- [9] G. C. Brown, "Nitric oxide inhibition of cytochrome oxidase and mitochondrial respiration: implications for inflammatory, neurodegenerative and ischaemic pathologies," *Molecular and Cellular Biochemistry*, vol. 174, no. 1/2, pp. 189-192, 1997.
- [10] C. Hölscher, "Nitric oxide, the enigmatic neuronal messenger: its role in synaptic plasticity," *Trends in Neurosciences*, vol. 20, no. 7, pp. 298-303, 1997.
- [11] D. S. Bredt, P. M. Hwang, and S. H. Snyder, "Localization of nitric oxide synthase indicating a neural role for nitric oxide," *Nature*, vol. 347, no. 6295, pp. 768-770, 1990.
- [12] M. Ding, J. L. Wong, N. E. Rogers, L. J. Ignarro, and R. R. Voskuhl, "Gender differences of inducible nitric oxide production in SJL/J mice with experimental autoimmune encephalomyelitis," *Journal of Neuroimmunology*, vol. 77, no. 1, pp. 99-106, 1997.
- [13] C. Iadecola, F. Zhang, S. Xu, R. Casey, and M. E. Ross, "Inducible nitric oxide synthase gene expression in brain following cerebral ischemia," *Journal of Cerebral Blood Flow and Metabolism*, vol. 15, no. 3, pp. 378-384, 1995.
- [14] A. H. Ding, C. F. Nathan, and D. J. Stuehr, "Release of reactive nitrogen intermediates and reactive oxygen intermediates from mouse peritoneal macrophages. Comparison of activating cytokines and evidence for independent production," *Journal of Immunology*, vol. 141, no. 7, pp. 2407-2412, 1988.
- [15] R. S. B. Clark, J. K. Schiding, S. L. Kaczorowski, D. W. Marion, and P. M. Kochanek, "Neutrophil accumulation after traumatic brain injury in rats: comparison of weight drop and controlled cortical impact models," *Journal of Neurotrauma*, vol. 11, no. 5, pp. 499-506, 1994.
- [16] R. S. B. Clark, P. M. Kochanek, M. A. Schwarz et al., "Inducible nitric oxide synthase expression in cerebrovascular smooth muscle and neutrophils after traumatic brain injury in immature rats," *Pediatric Research*, vol. 39, no. 5, pp. 784-790, 1996.
- [17] R. Fusco, E. Gugliandolo, R. Siracusa et al., "Formyl peptide receptor 1 signaling in acute inflammation and neural differentiation induced by traumatic brain injury," *Biology*, vol. 9, no. 9, p. 238, 2020.
- [18] E. Gugliandolo, R. D'Amico, M. Cordaro et al., "Neuroprotective effect of artesunate in experimental model of traumatic brain injury," *Frontiers in Neurology*, vol. 9, p. 590, 2018.
- [19] J. E. Merrill, L. J. Ignarro, M. P. Sherman, J. Melinek, and T. E. Lane, "Microglial cell cytotoxicity of oligodendrocytes is mediated through nitric oxide," *Journal of Immunology*, vol. 151, no. 4, pp. 2132-2141, 1993.
- [20] C. Gahm, S. Holmin, P. N. Wiklund, L. Brundin, and T. Mathiesen, "Neuroprotection by selective inhibition of inducible nitric oxide synthase after experimental brain contusion," *Journal of Neurotrauma*, vol. 23, no. 9, pp. 1343-1354, 2006.
- [21] J. F. Stover, A. Belli, H. Boret et al., "Nitric oxide synthase inhibition with the antipterin VAS203 improves outcome in moderate and severe traumatic brain injury: a placebo-controlled randomized phase IIa trial (NOSTRA)," *Journal of Neurotrauma*, vol. 31, no. 19, pp. 1599-1606, 2014.
- [22] B. S. Meldrum, "Glutamate as a neurotransmitter in the brain: review of physiology and pathology," *The Journal of Nutrition*, vol. 130, no. 4, pp. 1007S-1015S, 2000.
- [23] C. R. Dorsett, J. L. McGuire, E. A. K. Depasquale, A. E. Gardner, C. L. Floyd, and R. E. McCullumsmith, "Glutamate neurotransmission in rodent models of traumatic brain injury," *Journal of Neurotrauma*, vol. 34, no. 2, pp. 263-272, 2017.
- [24] Z. Hong, Z. Xinding, Z. Tianlin, and C. Liren, "Excitatory amino acids in cerebrospinal fluid of patients with acute head injuries," *Clinical Chemistry*, vol. 47, no. 8, pp. 1458-1462, 2001.
- [25] R. M. Guerriero, C. C. Giza, and A. Rotenberg, "Glutamate and GABA imbalance following traumatic brain injury," *Current Neurology and Neuroscience Reports*, vol. 15, no. 5, p. 27, 2015.
- [26] T. Chen, S. H. Dai, Z. Q. Jiang et al., "The AMPAR antagonist perampamil attenuates traumatic brain injury through antioxidant and anti-inflammatory activity," *Cellular and Molecular Neurobiology*, vol. 37, no. 1, pp. 43-52, 2017.

- [27] C. Y. Chen, L. Matt, J. W. Hell, and M. A. Rogawski, "Perampanel inhibition of AMPA receptor currents in cultured hippocampal neurons," *PLoS One*, vol. 9, no. 9, p. e108021, 2014.
- [28] V. Aida, T. L. Niedzielko, J. P. Szaflarski, and C. L. Floyd, "Acute administration of perampanel, an AMPA receptor antagonist, reduces cognitive impairments after traumatic brain injury in rats," *Experimental Neurology*, vol. 327, p. 113222, 2020.
- [29] L. Yurkewicz, J. Weaver, M. R. Bullock, and L. F. Marshall, "The effect of the selective NMDA receptor antagonist traxoprodil in the treatment of traumatic brain injury," *Journal of Neurotrauma*, vol. 22, no. 12, pp. 1428–1443, 2005.
- [30] E. Visser and S. A. Schug, "The role of ketamine in pain management," *Biomedicine and Pharmacotherapy*, vol. 60, no. 7, pp. 341–348, 2006.
- [31] A. J. Peters, L. E. Villasana, and E. Schnell, "Ketamine alters hippocampal cell proliferation and improves learning in mice after traumatic brain injury," *Anesthesiology*, vol. 129, no. 2, pp. 278–295, 2018.
- [32] Y. Li, R. Shen, G. Wen et al., "Effects of ketamine on levels of inflammatory cytokines IL-6, IL-1 β , and TNF- α in the hippocampus of mice following acute or chronic administration," *Frontiers in Pharmacology*, vol. 8, p. 139, 2017.
- [33] J. Liang, S. Wu, W. Xie, and H. He, "Ketamine ameliorates oxidative stress-induced apoptosis in experimental traumatic brain injury via the Nrf2 pathway," *Drug Design, Development and Therapy*, vol. 12, pp. 845–853, 2018.
- [34] M. Akamatsu, T. Yamashita, N. Hirose, S. Teramoto, and S. Kwak, "The AMPA receptor antagonist perampanel robustly rescues amyotrophic lateral sclerosis (ALS) pathology in sporadic ALS model mice," *Scientific Reports*, vol. 6, no. 1, 2016.
- [35] N. Bektas, R. Arslan, and F. Alyu, "The anxiolytic effect of perampanel and possible mechanisms mediating its anxiolytic effect in mice," *Life Sciences*, vol. 261, article 118359, 2020.
- [36] Y. Xiong, A. Mahmood, and M. Chopp, "Animal models of traumatic brain injury," *Nature Reviews Neuroscience*, vol. 14, no. 2, pp. 128–142, 2013.
- [37] F. Sivandzade, F. Alqahtani, A. Sifat, and L. Cucullo, "The cerebrovascular and neurological impact of chronic smoking on post-traumatic brain injury outcome and recovery: an in vivo study," *Journal of Neuroinflammation*, vol. 17, no. 1, p. 133, 2020.
- [38] M. L. Seibenhener and M. C. Wooten, "Use of the open field maze to measure locomotor and anxiety-like behavior in mice," *Journal of Visualized Experiments*, vol. 96, no. 96, 2015.
- [39] S. Alzarea and S. Rahman, "Alpha-7 nicotinic receptor allosteric modulator PNU120596 prevents lipopolysaccharide-induced anxiety, cognitive deficit and depression-like behaviors in mice," *Behavioural Brain Research*, vol. 366, pp. 19–28, 2019.
- [40] C. J. Miedel, J. M. Patton, A. N. Miedel, E. S. Miedel, and J. M. Levenson, "Assessment of spontaneous alternation, novel object recognition and limb clasp in transgenic mouse models of amyloid- β and tau neuropathology," *Journal of Visualized Experiments*, vol. 2017, no. 123, p. 55523, 2017.
- [41] M. Mohany, A. Z. Alanazi, F. Alqahtani, O. M. Belali, M. M. Ahmed, and S. S. Al-Rejaie, "LCZ696 mitigates diabetic-induced nephropathy through inhibiting oxidative stress, NF-KB mediated inflammation and glomerulosclerosis in rats," *PeerJ*, vol. 8, article e9196, 2020.
- [42] S. Haider, F. Naqvi, Z. Batool et al., "Pretreatment with curcumin attenuates anxiety while strengthens memory performance after one short stress experience in male rats," *Brain Research Bulletin*, vol. 115, pp. 1–8, 2015.
- [43] F. Zheng, Z. A. Xia, Y. F. Zeng et al., "Plasma metabolomics profiles in rats with acute traumatic brain injury," *PLoS One*, vol. 12, no. 8, p. e0182025, 2017.
- [44] A. I. Maas, D. K. Menon, P. D. Adelson et al., "Traumatic brain injury: integrated approaches to improve prevention, clinical care, and research," *The Lancet Neurology*, vol. 16, no. 12, pp. 987–1048, 2017.
- [45] V. PietroDi, K. M. Yakoub, G. Caruso et al., "Antioxidant therapies in traumatic brain injury," *Antioxidants*, vol. 9, no. 3, p. 260, 2020.
- [46] A. W. Unterberg, J. Stover, B. Kress, and K. L. Kiening, "Edema and brain trauma," *Neuroscience*, vol. 129, no. 4, pp. 1019–1027, 2004.
- [47] H. Z. Toklu and N. Tümer, "Oxidative stress, brain edema, blood-brain barrier permeability, and autonomic dysfunction from traumatic brain injury," in *Brain Neurotrauma: Molecular, Neuropsychological, and Rehabilitation Aspects*, pp. 43–48, CRC Press/Taylor & Francis, 2015.
- [48] J. D. Bell, "In vogue," *Anesthesia & Analgesia*, vol. 124, no. 4, pp. 1237–1243, 2017.
- [49] O. H. Miller, L. Yang, C. C. Wang et al., "GluN2B-containing NMDA receptors regulate depression-like behavior and are critical for the rapid antidepressant actions of ketamine," *eLife*, vol. 3, 2014.
- [50] S. Suda and K. Kimura, "Therapeutic potential of AMPA receptor antagonist perampanel against cerebral ischemia: beyond epileptic disorder," *Neural Regeneration Research*, vol. 14, no. 9, pp. 1525–1526, 2019.
- [51] C. Cornelius, R. Crupi, V. Calabrese et al., "Traumatic brain injury: oxidative stress and neuroprotection," *Antioxidants and Redox Signaling*, vol. 19, no. 8, pp. 836–853, 2013.
- [52] D. S. Dewitt and D. S. Prough, "Blast-induced brain injury and posttraumatic hypotension and hypoxemia," *Journal of Neurotrauma*, vol. 26, no. 6, pp. 877–887, 2009.
- [53] Y. Nakagami, "Nrf2 is an attractive therapeutic target for retinal diseases," *Oxidative Medicine and Cellular Longevity*, vol. 2016, Article ID 7469326, 8 pages, 2016.
- [54] M. Jaramillo, D. C. Gowda, D. Radzioch, and M. Olivier, "Hemozoin increases IFN- γ -inducible macrophage nitric oxide generation through extracellular signal-regulated kinase- and NF-KB-dependent pathways," *The Journal of Immunology*, vol. 171, no. 8, pp. 4243–4253, 2003.
- [55] D. O. Willenborg, M. Staykova, S. Fordham, N. O'Brien, and D. Linares, "The contribution of nitric oxide and interferon gamma to the regulation of the neuro-inflammation in experimental autoimmune encephalomyelitis," *Journal of Neuroimmunology*, vol. 191, no. 1–2, pp. 16–25, 2007.
- [56] D. Cederberg and P. Siesjö, "What has inflammation to do with traumatic brain injury?," *Child's Nervous System*, vol. 26, no. 2, pp. 221–226, 2010.
- [57] M. Hecker, C. Preiß, P. Klemm, and R. Busse, "Inhibition by antioxidants of nitric oxide synthase expression in murine macrophages: role of nuclear factor kB and interferon regulatory factor 1," *British Journal of Pharmacology*, vol. 118, no. 8, pp. 2178–2184, 1996.
- [58] M. D. Whiting, A. I. Baranova, and R. J. Hamm, "Cognitive impairment following traumatic brain injury," in *Animal*

Models of Cognitive Impairment, pp. 301–314, CRC Press, 2006.

- [59] A. d. G. Fedoce, F. Ferreira, R. G. Bota, V. Bonet-Costa, P. Y. Sun, and K. J. A. Davies, “The role of oxidative stress in anxiety disorder: cause or consequence?,” *Free Radical Research*, vol. 52, no. 7, pp. 737–750, 2018.
- [60] H. Rammal, J. Bouayed, C. Younos, and R. Soulimani, “Evidence that oxidative stress is linked to anxiety-related behaviour in mice,” *Brain, Behavior, and Immunity*, vol. 22, no. 8, pp. 1156–1159, 2008.
- [61] M. N. M. LimaDe, M. Polydoro, D. C. Laranja et al., “Recognition memory impairment and brain oxidative stress induced by postnatal iron administration,” *European Journal of Neuroscience*, vol. 21, no. 9, pp. 2521–2528, 2005.
- [62] B. Wang and S. Han, “Inhibition of inducible nitric oxide synthase attenuates deficits in synaptic plasticity and brain functions following traumatic brain injury,” *Cerebellum*, vol. 17, no. 4, pp. 477–484, 2018.
- [63] L. Tao, “Oxidation of polyunsaturated fatty acids and its impact on food quality and human health,” *Advances in Food Technology and Nutritional Sciences-Open Journal*, vol. 1, no. 6, pp. 135–142, 2015.
- [64] T. S. Anthonymuthu, E. M. Kenny, and H. Bayır, “Therapies targeting lipid peroxidation in traumatic brain injury,” *Brain Research*, vol. 1640, Part A, pp. 57–76, 2016.
- [65] G. Spiteller, “Peroxidation of linoleic acid and its relation to aging and age dependent diseases,” *Mechanisms of Ageing and Development*, vol. 122, no. 7, pp. 617–657, 2001.
- [66] J. Whelan and K. Fritsche, “Linoleic acid,” *Advances in Nutrition*, vol. 4, no. 3, pp. 311–312, 2013.

Research Article

Effect of Selenium on Expression of Apoptosis-Related Genes in Cryomedia of Mice Ovary after Vitrification

Reza Nori-Garavand,^{1,2} Maryam Hormozi,^{2,3} Leila Narimani,^{1,2} Nasim Beigi Boroujeni,² Asghar Rajabzadeh,^{1,2} Leila Zarei,^{1,2} Masoud Beigi Boroujeni,⁴ and Mandana Beigi Boroujeni ^{1,2}

¹Department of Anatomical Sciences, Lorestan University of Medical Sciences, Khorramabad, Iran

²Razi Herbal Medicines Research Center, Lorestan University of Medical Sciences, Khorramabad, Iran

³Department of Biochemistry, Lorestan University of Medical Sciences, Khorramabad, Iran

⁴Department of Biochemistry, Branch of Tehran-Shargh, Payame Noor University, Tehran, Iran

Correspondence should be addressed to Mandana Beigi Boroujeni; mandana.beigi@lums.ac.ir

Received 11 July 2020; Revised 15 August 2020; Accepted 14 September 2020; Published 23 September 2020

Academic Editor: Monica Fedele

Copyright © 2020 Reza Nori-Garavand et al. This is an open access article distributed under the Creative Commons Attribution License, which permits unrestricted use, distribution, and reproduction in any medium, provided the original work is properly cited.

Introduction. Freezing of ovarian tissue is used for preservation of fertility. The freezing-thawing process is accompanied by oxidative stress and induction of apoptosis. Apoptosis is a complex process that has been studied in animal models. The present study was aimed at investigating the effect of selenium on suppression of apoptosis during vitrification-thawing process of mice ovary via studying expression of apoptosis-related genes, and also, we aimed to design statistical models for the roles of single genes and gene-gene interactions in suppression of apoptosis. **Methods.** A total of 10 right ovary samples from 10 mice were randomly divided into two groups of selenium treatment (at dose 5 µg/ml sodium selenite, through adding to the media) and control group. Vitrification-thawing process was done according to the existed protocols. Real-time PCR was used for gene expression study. The apoptosis gene profile included *P53*, *Bax*, *Fas*, and *Bcl-2*. General linear model was applied to study single gene associations and gene-gene interactions. **Results.** From the studied genes, *P53* showed a significant downregulation in the selenium group in comparison to the control group ($\Delta\Delta CT = 1.96$; $P = 0.013$; relative expression (RE) = 0.28). *Bcl-2* showed a significant upregulation in the selenium group in comparison to the control group ($\Delta\Delta CT = -2.49$; $P < 0.001$; RE = 3.49). No significant result was found for other genes. According to the multiple models, *Bcl-2* showed a protective single gene association (beta = -0.33; $P = 0.032$), and *Fas* * *Bcl-2* interaction was significantly positive (beta = 0.19; $P = 0.036$). **Conclusion.** Addition of selenium to cryomedia of vitrification-thawing process could reduce the apoptosis induced by freezing-thawing stress in mice ovary via downregulation of *P53* and upregulation of *Bcl-2* at transcription level. Multivariable statistical models should be performed in future researches to study biological systems.

1. Introduction

1.1. Background. Some women need to preserve their fertility for their future life. The most important reason for the necessity of fertility preservation is cancer [1]. During chemotherapy and radiotherapy, ovaries may be affected by chemical and physical cytotoxic agents [2]. To solve this problem, freezing of ovarian samples was suggested [3]. Other than ovarian samples, sperms and spermatogonial stem cells are also frozen. There are usually two freezing methods consist

of slow freezing (conventional cryopreservation) and rapid freezing (vitrification or rapid cryopreservation). Freezing-thawing process is associated with oxidative stress and cell damage. Therefore, using additive antioxidants in cellular or tissue preservation media has been suggested [4].

Selenium is a biological trace element plays a key role in human metabolism. Selenium is used for synthesis of selenoproteins in the liver. This element performs its function as a component of antioxidant enzymes [5]. Other than nutritional values, selenium has an important role in human

immune system [6]. Because of the antioxidant effects of selenium, it is widely used in the studies of the animal models of oxidative stress [7].

Apoptosis is a kind of programmed cell death which is usually a physiological phenomenon. However, if the micro-environment of the cells is not suitable, a pathologic apoptosis may occur [8]. Freezing-thawing damage is an example of this unsuitable environmental condition [9]. So far, many animal studies have been designed to model induction of apoptosis. For instance, chemotherapeutic agents are used for induction of apoptosis in animal models [10]. In a rabbit osteoarthritis model, transection of anterior cruciate ligament was applied for induction of apoptosis in chondrocytes [11]. Other than *in vivo* studies, animal cells and tissues are used *in vitro* for apoptosis modeling. Freezing-thawing process is a common method for induction of apoptosis in a practical condition [12, 13]. Nevertheless, the exact mechanism of apoptosis induction and apoptosis suppression by antioxidants is not completely understood.

1.2. Objectives. Since there was a gap in evidence on the role of supplementation of nutritional elements to cryomedia of ovarian freezing-thawing process, this study was aimed at evaluating the role of selenium supplementation on reduction of apoptosis after vitrification of mice ovarian tissue through study of apoptosis-related genes including *P53*, *Bax*, *Bcl-2*, and *Fas*. In addition, a statistical modeling was designed to study the roles of single genes and gene-gene interactions in suppression of apoptosis. Our aims were both basic and practical.

2. Material and Methods

2.1. Study Design. An experimental study was conducted with *in vitro* design. This study consisted of cellular media processing and gene expression assay.

2.2. Animals and Study Groups. A total of 10 balb/c mice aged 6-8 weeks were bought from an animal laboratory of Lorestan University of Medical Sciences, Khorramabad, Lorestan Province, West of Iran. After approving the study protocol by the ethics committee of Lorestan University of Medical Sciences (registration number: IR.LUMS.REC.1397.195), the animals were imported to the study according to ethical guidelines for working with laboratory animal. All the animals were kept at standard condition of light, temperature, moisture, and nutrition. Pseudopregnancy was induced using a vaginal swab. The animals were sacrificed with cervical dislocation. The corpses were kept in supine position and fixed, and the abdominal hair was shaved. In a sterile condition, midline excision was conducted from xiphoid to pubis, and then, peritoneum was excised, and abdominal viscera were removed. The right ovaries were removed by surgical pans and knife for the study. The extra tissues around the ovaries were removed under a stereomicroscope. The ovarian particles were kept in Dulbecco's modified eagle medium (DMEM) culture environment with 10% fetal bovine serum (FBS). The samples were randomly divided into two groups: selenium group and control group.

2.3. Sample Processing. Ethylene glycol ficoll sucrose (EGFS) media was used for vitrification process according to a protocol mentioned by Chang et al. [14]. EGFS solution was prepared in a DMEM solvent containing of 40% ethylene glycol, 30% ficoll 70, and 0.5 mole sucrose. For the selenium group, 5 $\mu\text{g/ml}$ sodium selenite was added to EGFS solution [15]. Then, the EGFS was filtered with a 0.45 μm millipore filter and kept at -20°C . After preparation of the solutions EGFS and EGFS+Se, the ovarian samples were added to the solutions, and after dehydration, they were put in the cryovials. The dehydration process took about 5 minutes. The cryovials were put on nitrogen vapor for 30 seconds, and then, they were put at temperature -196°C in liquid nitrogen. For thawing process (rapid method), serial concentrations of sucrose solution were used as 1, 0.5, and 0.25 mole per one liter of DMEM, and the forth step was pure DMEM. The hydration process took about 5 minutes. After hydration process, the ovarian samples were kept in DMEM with 10% FBS, under CO_2 incubator at temperature 37°C for 24 hours. During this period, the samples were washed for some times. Finally, the ovarian samples were subjected for RNA extraction and gene expression study.

2.4. Molecular Assay. Total RNA was extracted using a column-based RNA extraction kit (Yektatajhez Azma, Iran). About 20-30 mg of each ovarian tissue was used. The extracted RNA was preserved in an RNase free elution solution. A NanoDrop spectrophotometer was used to read the concentrations. Then, the extracted RNA was kept at -70°C . cDNA was synthesized with oligo dT primers using cDNA synthesis kit (Sina Clone, Iran). Primers were designed with help of NCBI database (Table 1). GAPDH was used as internal control. Gene expression was studied via real-time polymerase chain reaction (real-time PCR). SYBR green master mix was used for amplification of the genes. The amplification process was observed and documented in Rotor Gene program. Each gene of each sample was run for 3 times, and then, the best results were chosen for analysis according to the melting curves and reaction efficiencies.

2.5. Data Analysis. Amounts of CTs were calculated based on takeoff and amplification cycles at the exponential phase. Reaction efficiencies were obtained from REST2009 program. ΔCT amounts were calculated via CT of target gene minus CT of reference gene. $\Delta\Delta\text{CT}$ amounts were also calculated in which one ΔCT was for the treated group and the other ΔCT was for the control group. Relative expression (RE) was calculated with Pfaffl's efficiency calibrated method in which each ΔCT was defined as CT of sample minus CT of control for each gene (equation (1)) [16]. RE was also calculated for comparison of apoptosis stimulating genes with *Bcl-2* apoptosis inhibitory gene. For statistical analysis, independent *t*-test was used for comparison of $-\Delta\text{CT}$ s between the groups, and one sample *t*-test was used for comparison of $-\Delta\Delta\text{CT}$ s with zero (as the null hypothesis). In order to adjust the associations of the target genes and their interactions with *Bcl-2* gene, a general linear model was used, and beta coefficient with 95% confidence interval (CI) was reported. All the analyses were done before computing RE.

TABLE 1: Primer sequences for amplification of cDNA.

Gene	Primer sequence (5'-3')	Product length (bp)
GAPDH	Forward: CAATGTGTCCGTCGTGGATCT Reverse: GTCCTCAGTGTAGCCCAAGATG	208
P53	Forward: GTTTCCTCTTGGGCTTAGGG Reverse: CTTCTGTACGGCGGTCTCTC	255
Bax	Forward: CGAGCTGATCAGAACCATCA Reverse: GAAAAATGCCTTCCCTTC	277
Fas	Forward: GAGAATTGCTGAAGACATGACAATCC Reverse: GTAGTTTTCACTCCAGACATTGTCC	314
Bcl-2	Forward: TAAGCTGTCACAGAGGGGCT Reverse: TGAAGAGTTCCTCCACCACC	344

Heat map was used to cluster the individual sample data. All the mathematical and statistical process was performed in the R 3.6.3 software (R foundation for statistical computing, Austria) [17].

$$RE = \frac{(E_{\text{target}})^{-\Delta CT_{\text{(sample-control)}}}}{(E_{\text{reference}})^{-\Delta CT_{\text{(sample-control)}}}}, \quad (1)$$

where $E = 2^{\text{Efficiency (\%)}}$.

3. Results

After extraction of RNA, the concentration of RNA was obtained at range 69.60-79.40 ng/ μ l. Using 1 μ l of cDNA and 1 μ l of 10 pmol primers resulted in successful amplification with one melting peak at a suitable temperature. From the repetitive reactions, those with better reaction efficiencies were selected. REs were calculated based on $\Delta CT_{\text{(sample-control)}}$ amounts adjusted with the efficiencies while statistical analyses (and calculation of P values) were done based on $\Delta CT_{\text{(target-reference)}}$ and $\Delta\Delta CT$ amounts (Tables 2 and 3). Our sample size had about 79% power to detect at least two amplification cycle differences with standard deviation of one cycle at the point of 5% type one error.

Among the four target genes, *P53* showed a significant downregulation ($P = 0.013$; $RE = 0.28$), and *Bcl-2* showed a significant upregulation ($P < 0.001$; $RE = 3.49$) in the treated group. The results of *Bax* and *Fas* were nonsignificant and inconclusive (Table 2) (Figures 1 and 2). In order to assay overall status of apoptosis with a gene expression approach, expression of target genes per *Bcl-2* was studied. All the target genes showed downregulation in comparison to *Bcl-2* antiapoptotic gene that the most downregulation was for *P53* ($RE = 0.08$) followed by *Bax* ($RE = 0.25$) and *Fas* ($RE = 0.30$) (Table 3) (Figure 3). Clustering of the individual samples showed similar results in the samples, except for sample 5 of the selenium group which was clustered in the cluster of the control group. Clustering of the genes showed that in condition of apoptosis, *Bcl-2* had more expression followed by *P53*, *Fas*, and *Bax*, of course without considering better efficiency of *P53* in our study (Figure 4).

The general linear model was used to reach a per se association of each gene without the confounding effect of other

genes. Accordingly, each unit of increase in ΔCT (i.e., down-regulation up to two folds) for *Bcl-2* was independently associated with about 33% reduction in the probability of being in the selenium-treated group ($\beta = -0.33$; $P = 0.032$). No significant association was found for other genes (Table 4, model 1) (Figure 5, model 1). Since *Bcl-2* had a better per se association and also was the only antiapoptotic gene, its interactions with the other target genes were also imported to the model. Accordingly, *Fas* * *Bcl-2* interaction was positive ($\beta = 0.19$; $P = 0.036$). No significant result was obtained for interactions *Bax* * *Bcl-2* and *P53* * *Bcl-2*. Interestingly, among the single genes, the association of *Fas* became significant ($\beta = -0.81$; $P = 0.045$), and *Bcl-2* lost its significance (Table 4, model 2) (Figure 5, model 2). Further addition of other possible interactions to the model resulted in loss of significance or software error due to low number of observations (data not shown).

4. Discussion

4.1. Interpretation. The aim of this study was to investigate mRNA expression profile of apoptosis-related genes in an animal tissue model of apoptosis induction by vitrification. This study consisted of the profile response to selenium administration as an antioxidant and investigation of gene-gene interactions in the mentioned profile. The practical aim was to reach a model for fertility preservation in conditions of different human pathologies such as cancers in young women.

Among the investigated genes, changes in the expression of *P53* and *Bcl-2* were statistically significant. Other than statistical analysis based on the number of PCR cycles (i.e., ΔCT and $\Delta\Delta CT$), efficiency calibrated method approved the associations of *P53* and *Bcl-2* (95% CIs of their REs had a remarkable distance from $RE = 1$ as a null hypothesis). In addition, proportions of *P53/Bcl-2*, *Bax/Bcl-2*, and *Fas/Bcl-2* mRNA expression were downregulated in the treated group as a manifestation of the general status of apoptosis at transcription level. It demonstrated that in biological systems, proportions of the levels of biomarkers might be more important than the pure levels to perform their biological functions.

Multivariable and multivariate analyses are a way for a better discovery and interpretation of biological systems. According to the heat map, the individual samples were

TABLE 2: Expressions of the target genes (selenium group vs. control group).

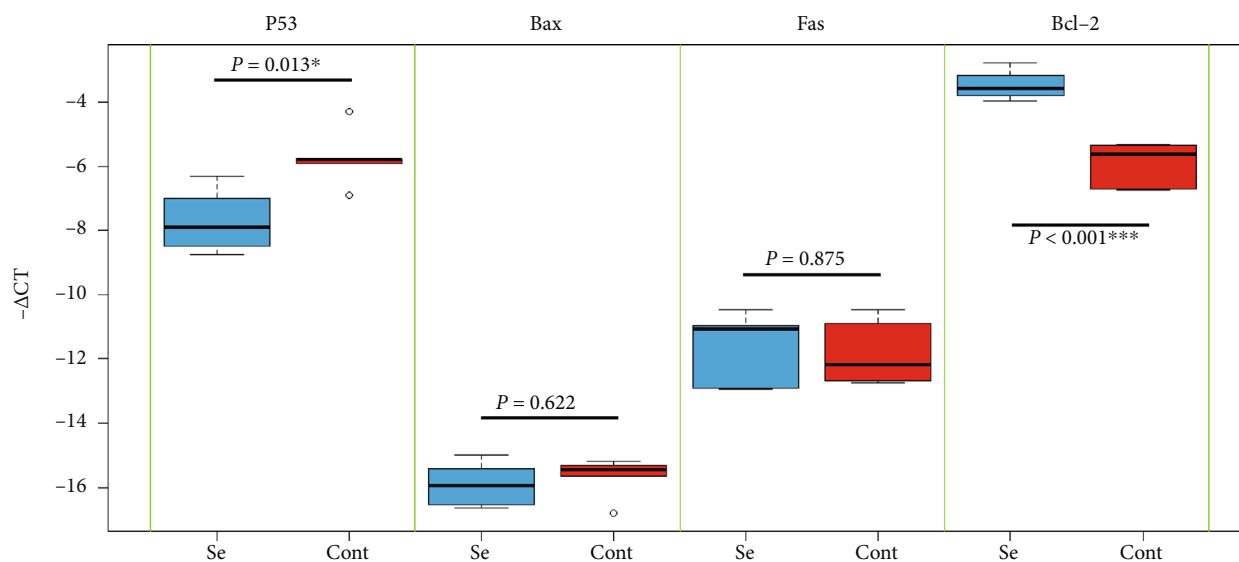
Gene	$\Delta\Delta CT$ (95% CI)	One sample P	Two sample P	Efficiency	RE (95% CI)
GAPDH	Reference			0.702	
P53	1.96 (0.69, 3.22)	0.013*	0.013*	0.921	0.28 (0.16, 0.47)
Bax	0.22 (-0.66, 1.11)	0.530	0.622	0.728	0.88 (0.78, 1.00)
Fas	-0.11 (-1.56, 1.33)	0.838	0.875	0.707	1.06 (0.68, 1.63)
Bcl-2	-2.49 (-3.09, -1.89)	<0.001***	<0.001***	0.734	3.49 (3.22, 3.78)

*Significant at 0.05. ***Significant at 0.001. CIs of RE were computed using RE formula on lower and upper bounds of ΔCT (sample-control for each gene separately).

TABLE 3: Expression of the target genes/Bcl-2 (selenium group vs. control group).

Gene	$\Delta\Delta CT$ (95% CI)	One sample P	Efficiency	RE (95% CI)
GAPDH	Reference		0.702	
Bcl-2	Reference		0.734	
P53	4.45 (2.78, 6.11)	0.002**	0.921	0.08 (0.05, 0.12)
Bax	2.71 (1.97, 3.44)	<0.001***	0.728	0.25 (0.24, 0.26)
Fas	2.37 (0.61, 4.14)	0.020*	0.707	0.30 (0.21, 0.43)

*Significant at 0.05. **Significant at 0.01. ***Significant at 0.001.

FIGURE 1: Gene expression comparison in selenium (Se) and control (Cont) groups (independent t -test).

clustered in their real groups except one sample of the selenium group that was clustered as the final branch of the control group. The clustering of the genes demonstrated that even in condition of apoptosis *Bcl-2* had further expression and in response to antiapoptotic agents its interval with apoptotic genes is increased. According to the general linear models, only *Bcl-2* had an independent association with the groups of study (in favor of being in the control group, i.e., antiapoptotic effect). After adjusting the model with the interactions of *Bcl-2*, the only significant associations were for *Fas* (in favor of being in the control group, i.e., antiapoptotic effect) and *Fas * Bcl-2* interaction (positive interaction, i.e., they help each other for upregulation). It showed that

either *Fas* had a secret effect on upregulation of *Bcl-2*, or its secret upregulation was due to a compensatory effect in response to *Bcl-2* upregulation. It was worth noting that the interaction *P53 * Bcl-2* did not have significant interaction in spite of their significant ratio of expression.

P53 is a tumor suppressor gene involved in both intrinsic and extrinsic pathways of apoptosis. Therefore, downregulation of *P53* is associated with reduction in apoptosis [18, 19]. *Bcl-2* is an antiapoptotic protein, and therefore, upregulation of *Bcl-2* is associated with suppression of apoptosis [20]. Proportion of *Bax/Bcl-2* is a widely used marker to study apoptosis. Downregulation of this proportion at transcriptome level may indicate downregulation of apoptosis. Das et al. (2007)

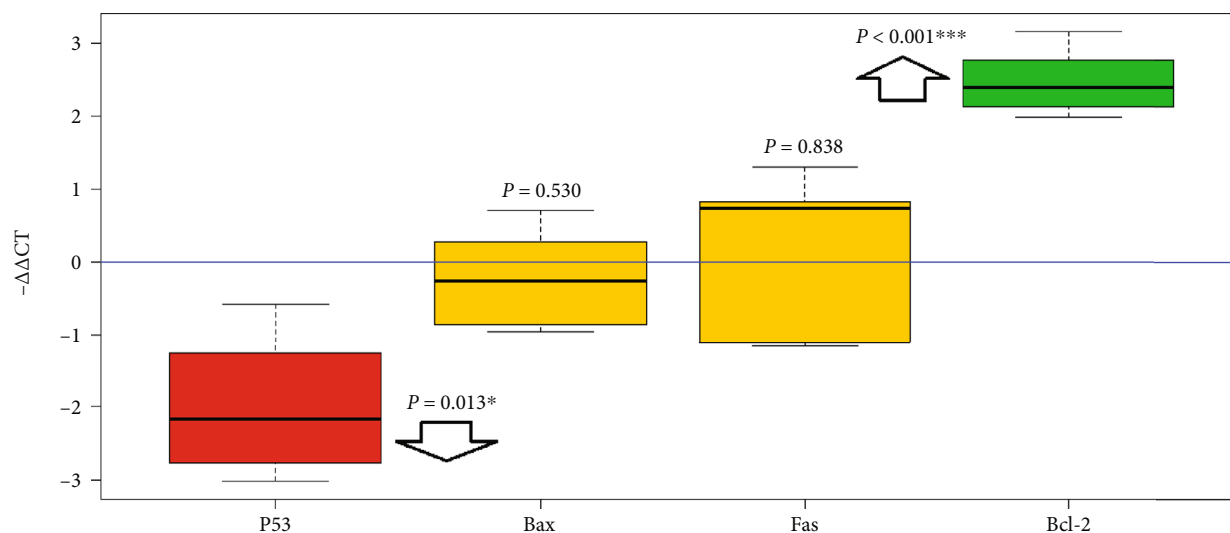


FIGURE 2: Gene expression of the target genes if the treated group calibrated with the control group (one sample *t*-test).

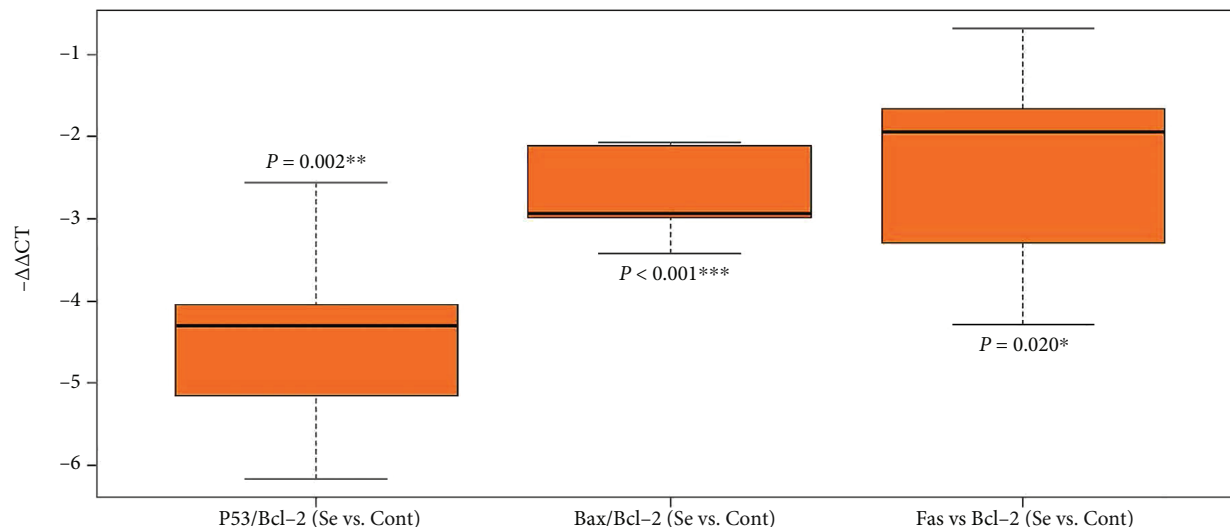


FIGURE 3: Gene expression of the target genes per expression Bcl-2 in the treated group calibrated with the control group (one sample *t*-test).

and Ghiasi et al. (2016) used this ratio via real-time PCR to detect apoptosis [21, 22]. However, in our study, the mRNA ratio *P53/Bcl-2* was more dominant, and the significant interaction was for *Fas * Bcl-2*.

In general, our study showed an antiapoptotic effect for selenium. The antiapoptotic effect of selenium may be resulted from its antioxidant effects [23]. A controversial hypothesis is that anticancer effect of selenium is through induction of apoptosis [6]. In fact, selenium participates in DNA repair, and it is resulted from helping antioxidant enzymes [24].

4.2. Previous Literature. Agrawal et al. (2006) reported that during freezing-thawing process reactive oxygen species (ROS) were increased and induced apoptosis [25]. It has been shown that the effect of ROS on induction of apoptosis is mainly through activation of *P53* [26]. Since in the present study *P53* was downregulated, it seems that protective effect

of selenium may be due to its antioxidant effects. Rimón et al. (2005) believed that apoptosis is the final response of cell to inappropriate conditions, and therefore, apoptosis study is a suitable tool in stressful conditions of freezing protocols [27].

A lot of researches have been performed on freezing media of ovary and sperm samples. Slaweta et al. (1988) had studied the relationship between selenium content of bull semen with sperm motility after freezing-thawing damage. They found that lower selenium content was associated with lower sperm motility [28]. Dorostkar et al. (2012) studied the effect of selenium additive on sperm characteristics in water buffaloes before and after freezing, and they reached a better sperm quality [29]. Rezaeian et al. (2016) studied the effects of selenium (at dose 5 μg/ml) on human sperm parameters after freezing-thawing process. They found a better sperm quality and suggested selenium supplementation for use in laboratories of infertility clinics [15]. Although

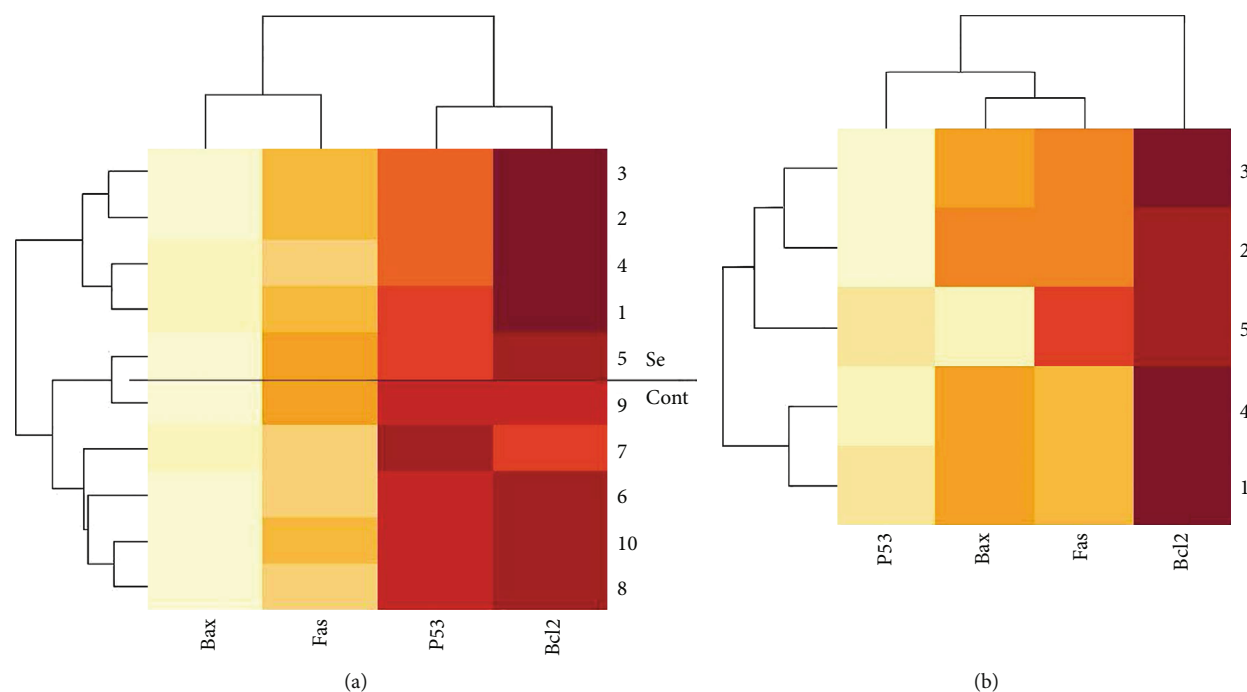


FIGURE 4: Clustering gene expression in individual samples. (a) $-\Delta CTs$ in selenium (Se) and control (Cont) groups. (b) $-\Delta\Delta CTs$ in each treated sample.

TABLE 4: General linear model for multiple adjustment of the associations of the genes with being the treated group.

Model/covariate	Beta coefficient (95%, CI)	Wald test P	Residual SE	R -squared
Model 1				
P53	0.01 (-0.28, 0.31)	0.913		
Bax	0.06 (-0.29, 0.42)	0.672		
Fas	0.06 (-0.20, 0.31)	0.598	0.268	0.856
Bcl-2	-0.33 (-0.62, -0.04)	0.032*		
Intercept	0.32 (-6.37, 7.01)			
Model 2				
P53	0.10 (-0.60, 0.79)	0.601		
Bax	0.64 (-0.92, 2.21)	0.218		
Fas	-0.81 (-1.58, -0.05)	0.045*		
Bcl-2	-0.91 (-6.80, 4.96)	0.570	0.111	0.990
Fas*Bcl-2	0.19 (0.03, 0.34)	0.036*		
P53*Bcl-2	-0.01 (-0.14, 0.11)	0.646		
Bax*Bcl-2	-0.10 (-0.45, 0.25)	0.342		
Intercept	1.10 (-23.37, 25.57)			

*Significant at 0.05 (it is also the interaction sign in the first column). SE: standard error.

there were many studies on the role of selenium in male reproduction system, there was not a study on the role of selenium supplementation in freezing-thawing process of ovary samples via studying apoptosis-related genes. It was the novelty of our study in comparison to the literature. Bozkurt et al. (2012) had found a protective effect for selenium on ischemia reperfusion injury in rat ovary via studying oxidative stress indices [30]. Brito et al. (2013) showed protective effects of selenium in combination with vitamin E on

ovarian samples of monkey via investigating expression of superoxide dismutase 1 gene [31]. In general, protective effect of selenium has been observed in many studies like our study.

4.3. Limitations. Lack of study at proteomic level was the most important limitation of our study. Also, frozen oocytes should be studied in future. Although our sample size had an approximately suitable power for univariable analyses like

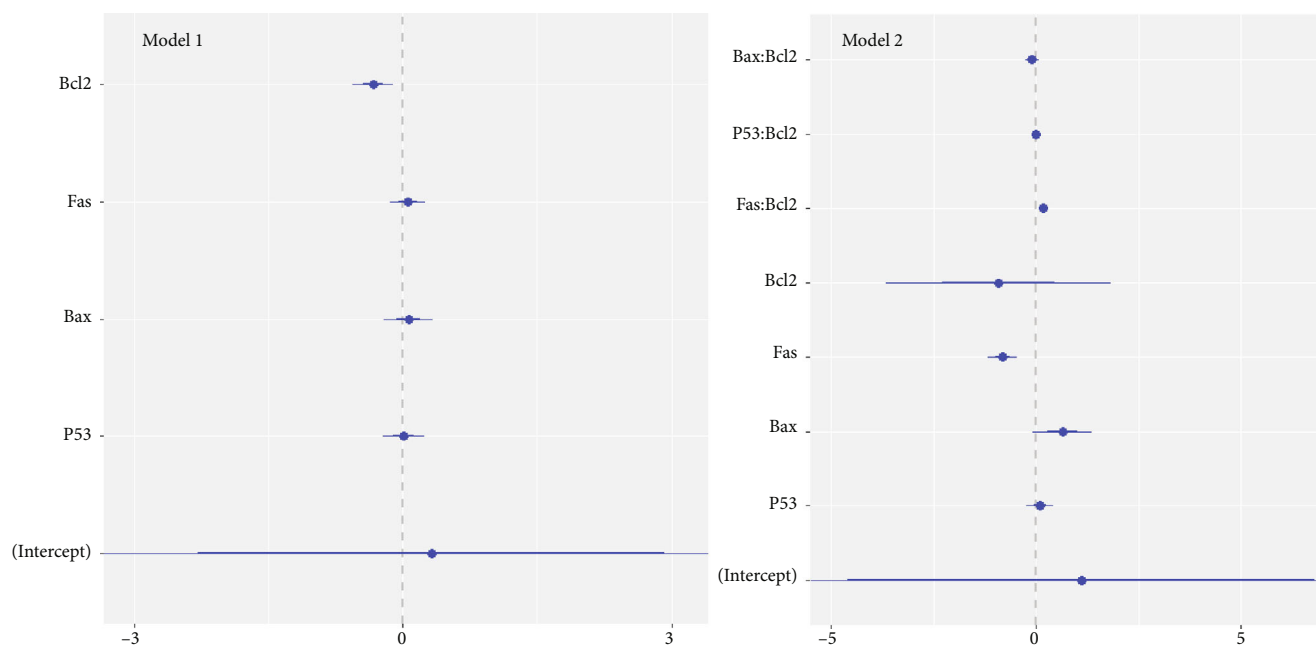


FIGURE 5: Coefficient plot of general linear model for $+\Delta CTs$ of the genes. Model 1: multiple adjusted model. Model 2: multiple adjusted model with interaction of target genes with Bcl-2.

other animal studies, our multiple models needed further observations to study all the possible interactions with enough power. However, our models were fit (low residual standard error) for individual predictions.

5. Conclusion

Addition of selenium at dose $5 \mu g/ml$ of sodium selenite to cryomeidia of vitrification-thawing process could reduce the apoptosis induced by freezing-thawing stress in mice ovary. This effect was thrown downregulation of P53 and upregulation of Bcl-2 at transcription level. According to the multiple models, Bcl-2 showed a protective single gene association, and Fas * Bcl-2 interaction was significantly positive. This study can be performed on human ovary samples in the patients who are candidate for wedge sample or whole ovary freezing regarding ethical and legal issues. Multivariable statistical models should be performed in future researches to study biological systems.

Data Availability

The data (raw amounts of CTs of the real-time PCR) used to support the findings of this study are available from the corresponding author upon request.

Ethical Approval

The ethics committee of Lorestan University of Medical Sciences (# IR.LUMS.REC.1397.195) approved the protocol of the study. The animals were imported to the study according to ethical guidelines for working with laboratory animal.

Conflicts of Interest

The authors declare no conflict of interest.

Authors' Contributions

All the authors had equal contribution and approved the final manuscript.

Acknowledgments

This study was MSc thesis of R Nori-Garavand under supervision of M Beigi Broujeni. We kindly acknowledge Razi Herbal Medicines Research Center of LUMS for giving the props of study.

References

- [1] J. Donnez and M.-M. Dolmans, "Fertility preservation in women," *New England Journal of Medicine*, vol. 377, no. 17, pp. 1657–1665, 2017.
- [2] M. Lambertini, L. del Mastro, M. C. Pescio et al., "Cancer and fertility preservation: international recommendations from an expert meeting," *BMC Medicine*, vol. 14, no. 1, p. 1, 2016.
- [3] S. Silber, "Ovarian tissue cryopreservation and transplantation: scientific implications," *Journal of Assisted Reproduction and Genetics*, vol. 33, no. 12, pp. 1595–1603, 2016.
- [4] M. Gholami, S. A. Y. Ahmadi, A. Abaszadeh, and A. Khaki, "Protective effects of melatonin and ghrelin on spermatogenesis: a narrative review of the literature," *International Journal of Reproductive Biomedicine*, vol. 15, no. 5, pp. 265–272, 2017.
- [5] R. F. Burk, "Selenium, an antioxidant nutrient," *Nutrition in Clinical Care*, vol. 5, no. 2, pp. 75–79, 2002.
- [6] J. C. Avery and P. R. Hoffmann, "Selenium, selenoproteins, and immunity," *Nutrients*, vol. 10, no. 9, article 1203, 2018.

- [7] H. Ahmadvand, E. Babaenezhad, H. Nayeri, and Z. Zarei Nezhad, "Selenium effects on antioxidant and inflammatory indices in renal ischemia-reperfusion injury in rats," *Journal of Renal Injury Prevention*, vol. 8, no. 2, pp. 71–77, 2019.
- [8] D. R. Green, *Apoptosis: Physiology and Pathology*, Cambridge University Press, 2011.
- [9] N. Zribi, N. F. Chakroun, F. Ben Abdallah et al., "Effect of freezing–thawing process and quercetin on human sperm survival and DNA integrity," *Cryobiology*, vol. 65, no. 3, pp. 326–331, 2012.
- [10] K. J. Yagle, J. F. Eary, J. F. Tait et al., "Evaluation of 18F-annexin V as a PET imaging agent in an animal model of apoptosis," *Journal of Nuclear Medicine*, vol. 46, no. 4, pp. 658–666, 2005.
- [11] A. Kourtis, P. G. Adamopoulos, A. Papalois, D. C. Iliopoulos, G. C. Babis, and A. Scorilas, "Quantitative analysis and study of the mRNA expression levels of apoptotic genes BCL2, BAX and BCL2L12 in the articular cartilage of an animal model of osteoarthritis," *Annals of Translational Medicine*, vol. 6, no. 12, p. 243, 2018.
- [12] E. Labrune, P. Jaeger, C. Santamaria et al., "Cellular and molecular impact of vitrification versus slow freezing on ovarian tissue," *Tissue Engineering Part C: Methods*, vol. 26, no. 5, pp. 276–285, 2020.
- [13] M. B. Boroujeni, F. Peidayesh, A. Pirnia, N. B. Boroujeni, S. A. Y. Ahmadi, and M. Gholami, "Effect of selenium on freezing–thawing damage of mice spermatogonial stem cell: a model to preserve fertility in childhood cancers," *Stem Cell Investigation*, vol. 6, p. 36, 2019.
- [14] H. J. Chang, J. H. Moon, J. R. Lee, B. C. Jee, C. S. Suh, and S. H. Kim, "Optimal condition of vitrification method for cryopreservation of human ovarian cortical tissues," *Journal of Obstetrics and Gynaecology Research*, vol. 37, no. 8, pp. 1092–1101, 2011.
- [15] Z. Rezaeian, H. Yazdekhashti, S. Nasri, Z. Rajabi, P. Fallahi, and F. Amidi, "Effect of selenium on human sperm parameters after freezing and thawing procedures," *Asian Pacific Journal of Reproduction*, vol. 5, no. 6, pp. 462–466, 2016.
- [16] J. S. Yuan, A. Reed, F. Chen, and C. N. Stewart Jr., "Statistical analysis of real-time PCR data," *BMC Bioinformatics*, vol. 7, no. 1, 2006.
- [17] R Core Team, *R: a language and environment for statistical computing*, R Foundation for Statistical Computing, Vienna, Austria, 2020.
- [18] S. Krautwald, E. Ziegler, L. Rölver et al., "Effective blockage of both the extrinsic and intrinsic pathways of apoptosis in mice by TAT-crmA," *Journal of Biological Chemistry*, vol. 285, no. 26, pp. 19997–20005, 2010.
- [19] J. D. Amaral, J. M. Xavier, C. J. Steer, and C. M. Rodrigues, "The role of p53 in apoptosis," *Discovery Medicine*, vol. 9, no. 45, pp. 145–152, 2010.
- [20] K. Fuenzalida, R. Quintanilla, P. Ramos et al., "Peroxisome proliferator-activated receptor γ up-regulates the Bcl-2 anti-apoptotic protein in neurons and induces mitochondrial stabilization and protection against oxidative stress and apoptosis," *Journal of Biological Chemistry*, vol. 282, no. 51, pp. 37006–37015, 2007.
- [21] A. Das, N. L. Banik, and S. K. Ray, "Differentiation decreased telomerase activity in rat glioblastoma C6 cells and increased sensitivity to IFN- γ and taxol for apoptosis," *Neurochemical Research*, vol. 32, no. 12, pp. 2167–2183, 2007.
- [22] P. Ghiasi, S. Hosseinkhani, H. Ansari, N. Aghdami, and H. Baharvand, "Comparison of BAX and Bcl-2 expression during human embryonic stem cell differentiation into cardiomyocytes and doxorubicin-induced apoptosis," *Biomacromolecular Journal*, vol. 2, no. 2, pp. 162–168, 2016.
- [23] A. Valadbeygi, T. Naji, A. Pirnia, and M. Gholami, "Supplementation freeze-thawed media with selenium protect adipose-derived mesenchymal stem cells from freeze-thawed induced injury," *Cryobiology*, vol. 73, no. 2, pp. 135–139, 2016.
- [24] S. Bera, V. D. Rosa, W. Rachidi, and A. M. Diamond, "Does a role for selenium in DNA damage repair explain apparent controversies in its use in chemoprevention?," *Mutagenesis*, vol. 28, no. 2, pp. 127–134, 2013.
- [25] A. Agarwal, S. Gupta, and S. Sikka, "The role of free radicals and antioxidants in reproduction," *Current Opinion in Obstetrics and Gynecology*, vol. 18, no. 3, pp. 325–332, 2006.
- [26] B. Y. Sheikh, M. M. R. Sarker, M. N. A. Kamarudin, and G. Mohan, "Antiproliferative and apoptosis inducing effects of citral via p53 and ROS-induced mitochondrial-mediated apoptosis in human colorectal HCT116 and HT29 cell lines," *Biomedicine & Pharmacotherapy*, vol. 96, pp. 834–846, 2017.
- [27] E. Rimón, T. Cohen, A. Dantes et al., "Apoptosis in cryopreserved human ovarian tissue obtained from cancer patients: a tool for evaluating cryopreservation utility," *International Journal of Oncology*, vol. 27, no. 2, pp. 345–353, 2005.
- [28] R. Slaweta, W. Wařowicz, and T. Laskowska, "Selenium content, glutathione peroxidase activity, and lipid peroxide level in fresh bull semen and its relationship to motility of spermatozoa after freezing–thawing," *Journal of Veterinary Medicine Series A*, vol. 35, no. 1–10, pp. 455–460, 1988.
- [29] K. Dorostkar, S. M. Alavi-Shoushtari, and A. Mokarizadeh, "Effects of in vitro selenium addition to the semen extender on the spermatozoa characteristics before and after freezing in water buffaloes (*Bubalus bubalis*)," in *Veterinary research forum*, Faculty of Veterinary Medicine, Urmia University, Urmia, Iran, 2012.
- [30] S. Bozkurt, D. C. Arikan, E. B. Kurutas et al., "Selenium has a protective effect on ischemia/reperfusion injury in a rat ovary model: biochemical and histopathologic evaluation," *Journal of Pediatric Surgery*, vol. 47, no. 9, pp. 1735–1741, 2012.
- [31] D. C. Brito, A. B. Brito, S. R. R. A. Scalerio et al., "Vitamin E-analog Trolox prevents endoplasmic reticulum stress in frozen–thawed ovarian tissue of capuchin monkey (*Sapajus apella*)," *Cell and Tissue Research*, vol. 355, no. 2, pp. 471–480, 2014.

Research Article

A Modified Murine Calvarial Osteolysis Model Exposed to Ti Particles in Aseptic Loosening

Zhantao Deng ¹, Shuai Wang ^{1,2}, Mengyuan Li ¹, Guangtao Fu, ¹ Chang Liu ²,
Shuxian Li ^{1,2}, Jiewen Jin ³, Feng-Juan Lyu ², Yuanchen Ma ¹ and Qiuqian Zheng ¹

¹Department of Orthopedics, Guangdong Provincial People's Hospital, Guangdong Academy of Medical Sciences, Guangzhou 510080, China

²South China University of Technology-The University of Western Australia Joint Center for Regenerative Medicine Research, School of Medicine, South China University of Technology, Guangzhou 510641, China

³Department of Endocrinology, The First Affiliated Hospital, Sun Yat-sen University, Guangzhou 510080, China

Correspondence should be addressed to Yuanchen Ma; myc998@qq.com and Qiuqian Zheng; zhengqiuqian@gdph.org.cn

Received 15 May 2020; Accepted 7 August 2020; Published 25 August 2020

Guest Editor: Andrea Vecchione

Copyright © 2020 Zhantao Deng et al. This is an open access article distributed under the Creative Commons Attribution License, which permits unrestricted use, distribution, and reproduction in any medium, provided the original work is properly cited.

Aim. To investigate the different effects on osteolysis between commercial pure Ti particles and TiAl6V4 particles obtained from prosthesis of patients with aseptic loosening. **Method.** Scanning electron microscope, energy dispersive X-ray spectrometry, and X-ray diffraction were used for the size test, chemical composition test, and phase analysis of two kinds of Ti particles. Microcomputed tomography (micro-CT) and 3-dimensional reconstruction analysis were applied to analyze the bone loss quantitatively and radiologically. Hematoxylin-eosin (HE) staining and tartrate-resistant acid phosphatase (TRAP) staining were used to assess the histologic difference. **Result.** TiAl6V4 particles were constituted by FeO, Al₄₅V₇, and Al₃Ti while pure Ti particles were constituted by Ti, Ti₃O, and C₄H₇NO₃. Similar particle size of nanoscale was detected of two Ti particles. A TiAl6V4 osteolysis model had more severe bone loss when scanned with micro-CT and assessed by quantitative analysis. TiAl6V4 also presented deeper and wider calvarial bone loss in HE staining and more activated osteoclasts in TRAP staining. **Conclusion.** A mouse calvarial model is the most effective animal model for the primary *in vivo* research of aseptic loosening. Compared with commercial Ti particles, TiAl6V4 particles derived from prosthesis of an aseptic loosening patient had more severe bone loss and more activated osteoclast, which was more consistent with pathogenesis of aseptic loosening *in vivo*, had high success rate of establishment of a model, and was more desired in animal modeling.

1. Introduction

Total joint replacement (TJR) is a highly successful procedure to manage the pain and disability resulted from osteoarthritis and fractures, and there are about 1.5 million TJR procedures performed worldwide each year [1]. Aseptic loosening is the most common long-term cause of TJR failure, but the underlying mechanism is still unclear [2]. The release of biomaterial wear particles from prosthesis, which caused inflammatory response in bone microenvironment, is a recognized pathogenesis [3]. Since it takes long time of follow-up to detect aseptic loosening in clinical cases, more studies focus on cellular and tissue mechanisms, in which valid *in vivo* models are urgently needed.

A series of animal models have been used for studying the biology of aseptic osteolysis, including sheep, dogs, and rabbits [4]. However, a mouse model is most widely used, owing to its low cost of maintenance and diverse options in immune and genetic features [5]. Three mouse models are now available, including the air pouch model, the calvarial model, and intramedullary implant models [5]. Due to the ability to test the host response in an orthotopic bone site, the rapidity in developing osteolysis, the availability of quantified images of bone loss, and the relatively low cost, the calvarial model is the most widely used for the study of particle-induced osteolysis [5].

Titanium (Ti), chrome-cobalt (Cr-Co), and polymethyl-methacrylate (PMMA) particles are most commonly used

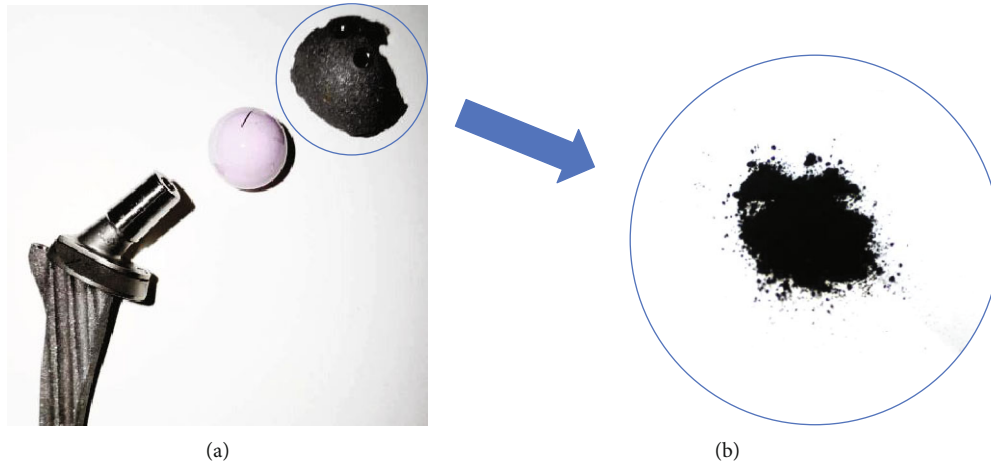


FIGURE 1: The prosthesis of patients with aseptic loosening (a) and TiAl6V4 particles (b) obtained from it.

in the studies of aseptic loosening [6]. Those particles are usually commercially available, which are different from the wear particles released from prosthesis in patients with aseptic loosening. Therefore, we compared the different effects on osteolysis between commercial pure Ti particles and TiAl6V4 particles obtained from the prosthesis of patients with aseptic loosening in the present study.

2. Methods

2.1. Preparation of Particles. TiAl6V4 particles were obtained from the prosthesis of patients with aseptic loosening. The TiAl6V4 prosthesis was placed in a fabricated high-vacuum three-electrode direct current under 10^{-3} Pa vacuum, 0.04 MPa argon and hydrogen 3:2 (v/v), and 650 A cathode current (Figure 1) [7]. The pure Ti particles were commercially available from the LINK Company. The particles were suspended in phosphate-buffered saline (PBS) at a concentration of 50 mg/mL as a stock solution.

2.2. Scanning Electron Microscope and Chemical Composition Test. The TiAl6V4 and pure Ti particles were first put into a vacuum drying oven (DZF-6012) at 133 Pa and 80°C for 12 h. After dehydration, the particle samples were adhered on the conductive adhesive, which were pasted on the tin plate. The samples were scanned by a field emission scanning electron microscope (Carl Zeiss AG, Merlin, Germany), and the images were obtained by assorted software. Chemical composition of tested particles was characterized by assorted dispersive X-ray spectrometry.

2.3. X-Ray Diffraction. The TiAl6V4 and pure Ti particles were sent to the Medical Device Research and Testing Center of South China University of Technology for phase analysis via X-ray diffraction (Malvern Panalytical, Empyrean, UK).

2.4. Murine Calvarial Osteolysis Model. The murine calvarial osteolysis model is widely used to study the pathogenesis of aseptic loosening. Six-week-old C57BL/J6 mice (6 mice for each group) were first anesthetized and placed in a prone position. Then, the skin of the cranium was incised along

the line between the two eyes and ears, and the cranial periosteum was removed by sharp dissection. 50 μ L of metal particle (TiAl6V4 and pure Ti) suspension (50 mg/mL, in PBS) was embedded in the middle of the calvarias. 50 μ L of PBS was applied as a sham group. After 2 weeks, all the mice were sacrificed, and the calvarias were harvested for further experiments. The research protocol was approved by the ethics committee of Guangdong Provincial People's Hospital, China.

2.5. Microcomputed Tomography (micro-CT) and 3-Dimensional Reconstruction Analysis. The calvarial caps of PIO murine models were analyzed by micro-CT scanning (SkyScan, Belgium) as previously reported [8]. 550 mA and 45 kV of X-ray energy and 18 mm resolution were set in the scanning. Quantitative analysis was performed in region around the midline after 3-dimensional reconstruction by assorted software. The analysis parameters included bone mineral density (BMD), bone volume/total volume (BV/TV), total porosity percentage, trabecular number (Tb.N), trabecular thickness (Tb.Th), and trabecular separation/spacing (Tb.Sp).

2.6. Histologic Staining. The calvarias of PIO murine models were first decalcified in 15% EDTA-PBS solution and then embedded in paraffin and sliced in the midline area where particle deposits. Hematoxylin-eosin (HE) staining (Beyotime, C0105, China) was used to observe overall pathological characteristics. Tartrate-resistant acid phosphatase (TRAP) staining (Sigma, 387A, USA) was used to detect osteoclasts activation. All the histologic staining was photographed with a light microscope (Nikon, C2+, Tokyo, Japan).

2.7. Statistical Analysis. All the data was analyzed by the SPSS22.0 software (SPSS, Chicago, IL) and were presented as the mean \pm standard error of the means. The differences between different groups were analyzed by the Brown-Forsythe test. $P < 0.05$ was considered as a significant difference.

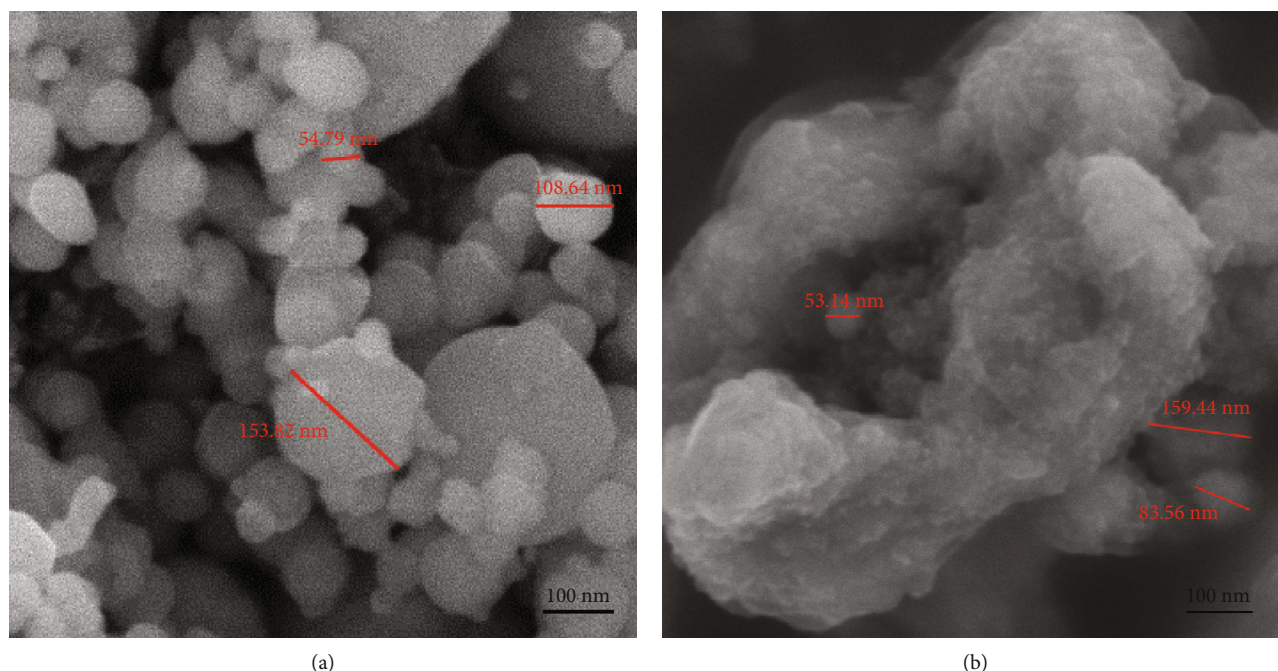


FIGURE 2: Scanning electron microscope of two Ti particles: (a) TiAl6V4 particles and (b) pure Ti particles.

TABLE 1: Chemical composition of TiAl6V4 and pure Ti particles.

Element	TiAl6V4		Pure Ti	
	Normalized mass (%)	Atomic percent (%)	Normalized mass (%)	Atomic percent (%)
Ti	28.70	9.78	67.52	37.64
C	57.84	78.57	10.39	23.11
N	-	-	10.97	20.90
O	10.22	10.42	10.83	18.07
Si	0.03	0.02	0.29	0.27
Al	0.73	0.44	-	-
V	1.92	0.62	-	-
Co	0.55	0.15	-	-

3. Results

3.1. The Difference of Physical Characteristics between TiAl6V4 and Pure Ti Particles. The size of metal particles appeared ranging between 54.79 nm and 153.82 nm for TiAl6V4 particles and 53.14 nm to 159.44 nm for pure Ti particles from scanning electron microscope images (Figure 2). The chemical compositions of TiAl6V4 and pure Ti particles are shown in Table 1. When analyzed with X-ray diffraction, the main phases of TiAl6V4 particles were constituted by FeO, Al₄₅V₇, and Al₃Ti while pure Ti particles were constituted by Ti, Ti₃O, and C₄H₇NO₃ (Figure 3).

3.2. Radiologic Difference between Two Ti Particle-Induced Calvarial Osteolysis Models. As shown from both 3-dimensional reconstruction images and representative coronal photographs at the cross-section of micro-CT scanning, significant bone loss was observed in both the TiAl6V4 and pure Ti groups when compared with the sham group (Figure 4). However, the TiAl6V4 group had more severe

bone loss compared with the pure Ti group. Further quantitative analysis also revealed significant reduction of BMD, BV/TV, and Tb.Th and increase of total porosity and Tb.Sp in the TiAl6V4 group when compared with the pure Ti group (Figure 5).

3.3. Histologic Characteristics of Two Ti Particle-Induced Calvarial Osteolyses. To further investigate the histologic difference of two osteolysis models, HE staining was applied. As shown in Figure 6, the TiAl6V4 particle-induced osteolysis model exhibited deeper and wider calvarial bone loss when compared with the pure Ti model. Furthermore, the osteoclasts were more activated in the TiAl6V4 group when staining with TRAP (Figure 7).

4. Discussion

The data from the present study revealed that compared with the commercial pure Ti osteolysis model, the TiAl6V4 osteolysis model had more severe bone loss when scanned with

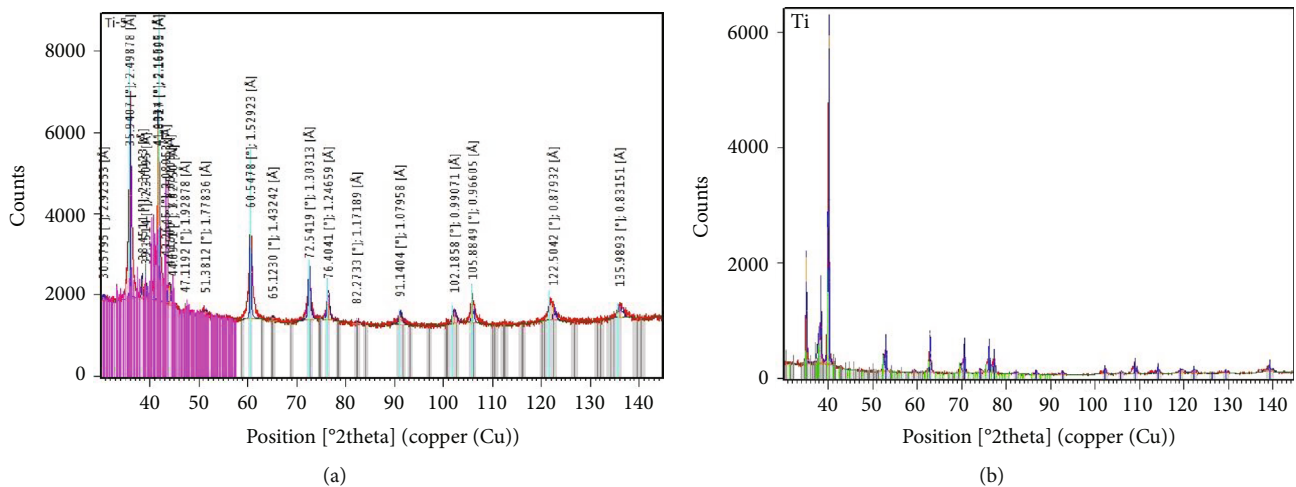


FIGURE 3: X-ray diffraction of two Ti particles: (a) TiAl6V4 particles and (b) pure Ti particles.

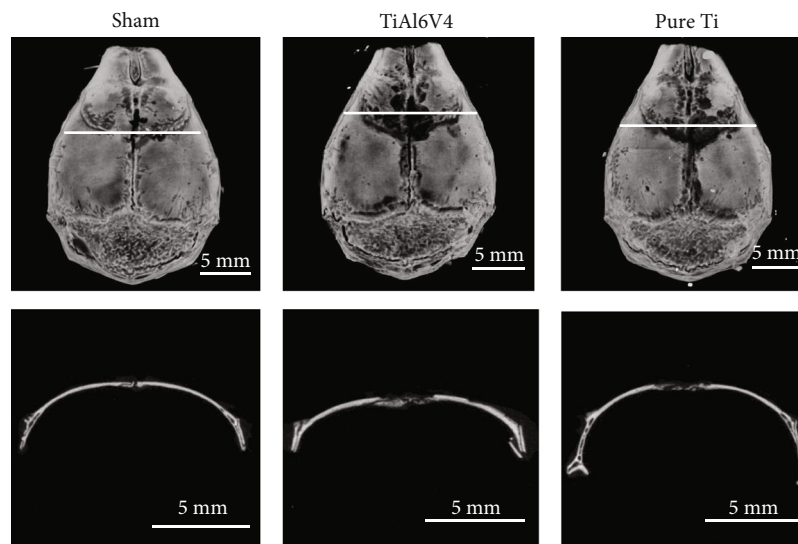


FIGURE 4: Microcomputed tomography with 3-dimensional reconstruction of calvarial caps from the murine osteolysis model induced by PBS (sham), TiAl6V4, and pure Ti particles. Three-dimensional reconstruction images appear in the first row, and the white horizontal line indicates the location of cross-sectional image in the second row.

micro-CT and significant reduction of BMD, BV/TV, and Tb.Th and increase of total porosity and Tb.Sp after further quantitative analysis. Regarding histologic characteristics, TiAl6V4 also presented deeper and wider calvarial bone loss in HE staining and more activated osteoclasts in TRAP staining.

Wear particle-induced aseptic loosening is considered the main cause of long-term failure in TJR, which leads to surgical revision and huge economic burden in public health. In this regard, thorough understanding of pathophysiology of aseptic loosening is vital for therapeutic development, and appropriate animal models are essential for the researches. A series of animals have been used for this purpose, including dogs, sheep, rabbits, and mice. In a large animal model (including dogs and sheep), total hip arthroplasty is usually applied, and different kinds of alloy

femoral component are implanted. The animals were allowed full ambulation postoperatively and sacrificed after 26-52 weeks [9, 10]. For the rabbit model, both total hip arthroplasty and drug test chamber, which are implanted at the level of the cortex in the proximal medial tibial metaphysis and connected with a diffusion pump, were used [11]. By simulating the TJR procedure on animal models, the behavior of the implant in the host is able to be understood globally. However, since the high cost of maintenance, long term in modelling, and difficulties in therapeutic interventions, they are not the most used animal models for primary *in vivo* research [5]. A mouse model, owing to its low cost of maintenance, short term in modelling, and the facility to reach sufficient numbers of subjects to strengthen statistical results, is the most effective alternative [12].

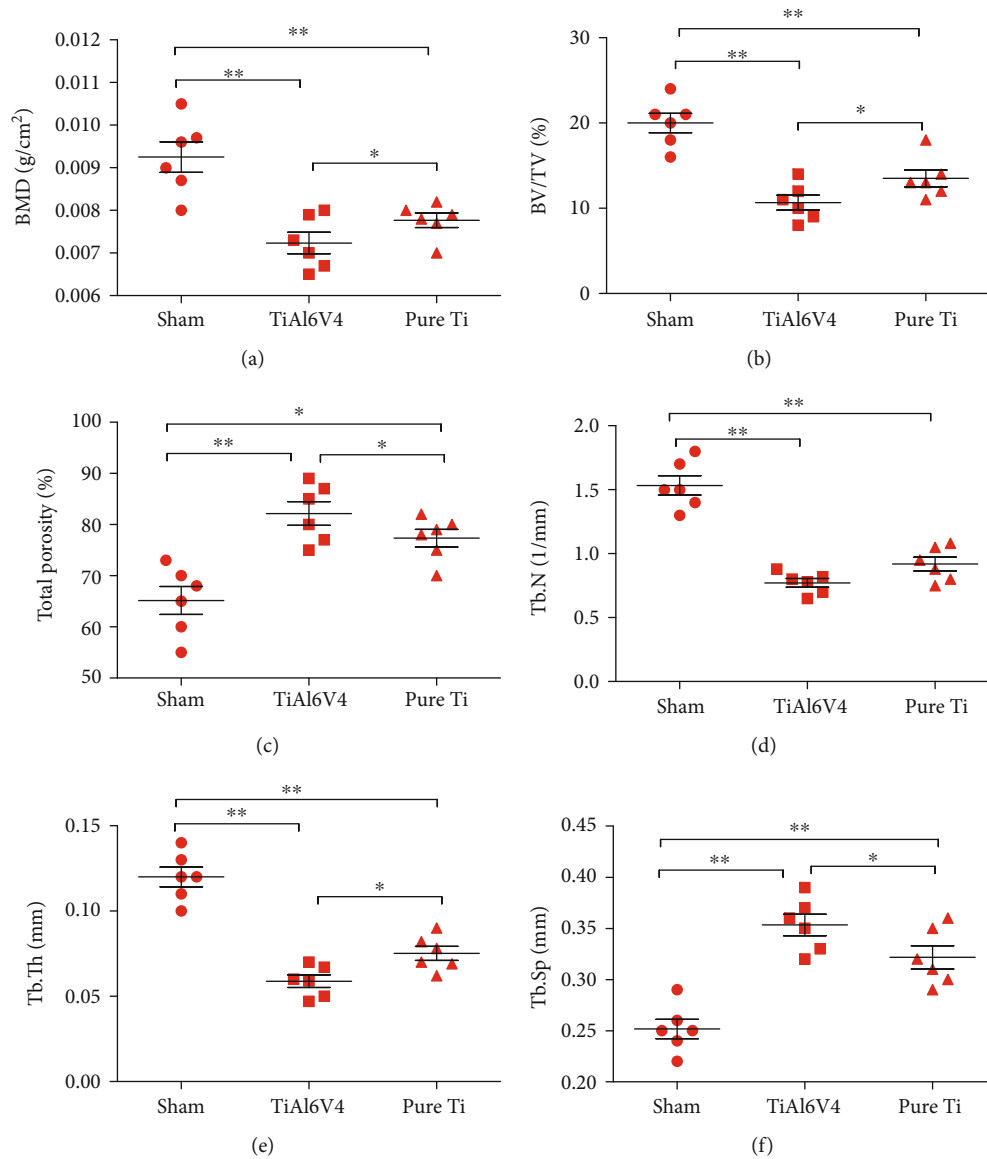


FIGURE 5: Quantitative analysis of osteolysis in calvarial caps from murine osteolysis model induced by PBS (sham), TiAl6V4, and pure Ti particles: (a) bone mineral density (BMD); (b) bone volume/total volume (BV/TV); (c) total porosity percentage; (d) trabecular number (Tb.N); (e) trabecular thickness (Tb.Th); (f) trabecular separation/spacing (Tb.Sp).

Two main mouse methods are mostly used for wear particle-induced osteolysis, namely, air pouch and calvarial models. In the air pouch model, subcutaneous space, which is called as the air pouch, is first established. Then, wear particles (including metal and polymeric biomaterial) are introduced in the air pouch, as well as implantation of the bone tissue [13]. This model is mainly served as an initial proof of concept in the targeting of anti-inflammatory or antiresorptive events related to particle-induced osteolysis [5]. However, since the bone implantation is nonvascular and has no biological activity, it is difficult to assess the direct interactions between particles and the bone tissue. The calvarial osteolysis model has several superiorities over the air pouch model. First, the calvarium is vascular, and the particles are exposed to the calvaria directly, which makes it possible to assess interactions between wear particles and bone

homeostasis [14, 15]. Second, micro-CT or histologic staining can be used to quantitatively assess the bone loss, both radiologically and biologically [16]. Third, transgenic and gene knockout mice can be used to investigate the relationship between wear particles and bone loss [17, 18].

Previous studies often focus on the methods of modeling; the sources of wear particles are seldom investigated. In the present study, we explored the difference of different sources of particles, including commercially purchased and derived from prosthesis of aseptic loosening. Our data shown that the TiAl6V4 model had deeper and wider calvarial bone loss and more activated osteoclast when compared with 0the commercial pure Ti model, in spite of similar particle size of nanoscale. The TiAl6V4 particles derived from Ti prosthesis of aseptic loosening patient had more complicated components when compared with commercial one, which may

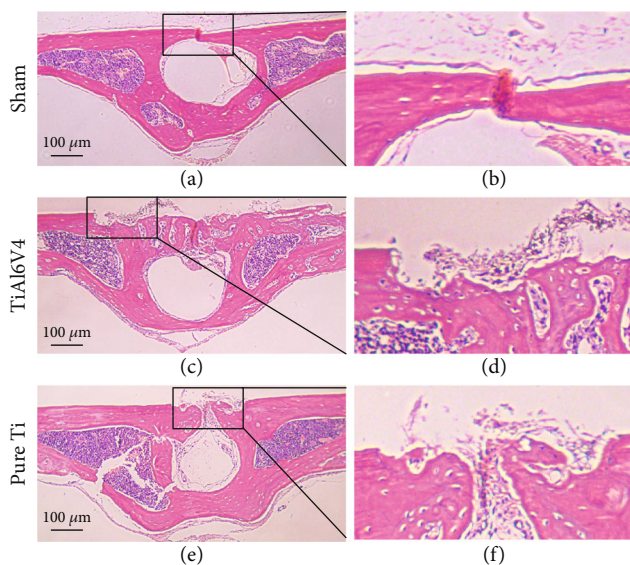


FIGURE 6: Representative images of HE staining of the calvaria from murine osteolysis model induced by PBS (sham), TiAl6V4, and pure Ti particles. The images in black box in (a, c, e) are enlarged and presented in (b, d, f).

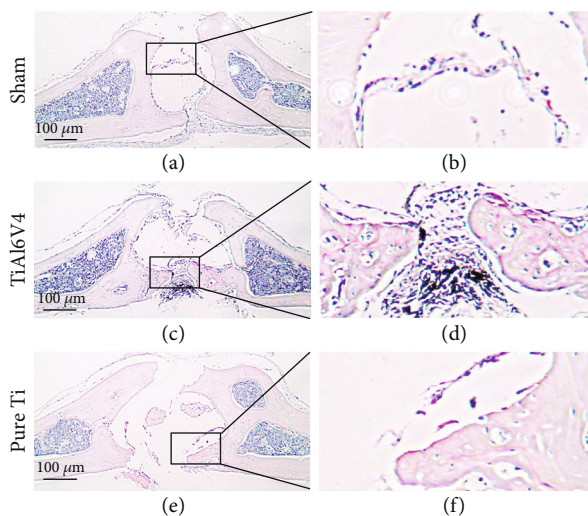


FIGURE 7: Representative images of TRAP staining of the calvaria from murine osteolysis model induced by PBS (sham), TiAl6V4, and pure Ti particles. The activated osteoclasts are stained as red. The images in black box in (a, c, e) are enlarged and presented in (b, d, f).

account for the different biological response of calvarial osteolysis model in part. Aluminum had toxicity on bone metabolism, including collagen synthesis and matrix mineralization [19]. The application of aluminum also reduced elastic modulus and stress, indicators of bone material intrinsic properties [20]. The exposure of metal ions (including titanium, aluminum, and vanadium) led to a reduction in cell viability, higher rates of early apoptosis, and upregulated expression of inflammatory cytokines and RANKL in osteoblasts [21]. Our previous study used TiAl6V4 and Cr-Co particles derived from the prosthesis of aseptic loosening patient for the osteolysis model and found novel mechanisms and

potential treatment of aseptic loosening, such as Sirtuin 1-mediated protein acetylation [8, 22], autophagy [16], and hydrogen sulfide [23]. The biological responses of different sources of wear particles need further investigation.

In conclusion, aseptic loosening is the most common long-term cause of TJR failure, in which cellular and tissue mechanisms are not clear and valid *in vivo* models are urgently needed. A mouse calvarial model is the most effective animal model for the primary *in vivo* research of aseptic loosening. Compared with commercial Ti particles, TiAl6V4 particles derived from prosthesis of an aseptic loosening patient had more severe bone loss and more activated osteoclast, which was more consistent with pathogenesis of aseptic loosening *in vivo*, had high success rate of establishment of model, and was more desired in animal modeling.

Data Availability

All data, models, and code generated or used during the study appear in the submitted article.

Conflicts of Interest

The authors declare that there are no conflicts of interest regarding the publication of this paper.

Acknowledgments

This work was supported by the National Natural Science Foundation of China Youth Science Foundation (81802222), the Natural Science Foundation of Guangdong Province (2018A030310694), the Basic and Applied Basic Research Foundation of Guangdong Province (2020A1515010268), the Guangdong Medical Science and Technology Research Foundation (2018114214430383), the Foundation of Traditional Chinese Medicine of Guangdong Province (20191004), the Scientific Foundation of Guangdong Provincial People's Hospital (2017bp01), the Outstanding Young Talents Foundation of Guangdong Provincial People's Hospital (KJ012019091) and Program of Science and Technology of Guangzhou (201904010424), and the China Postdoctoral Science Foundation (2018M640871).

References

- [1] J. A. Singh, M. B. Vessely, W. S. Harmsen et al., "A population-based study of trends in the use of total hip and total knee arthroplasty, 1969-2008," *Mayo Clinic Proceedings*, vol. 85, no. 10, pp. 898-904, 2010.
- [2] J. J. Cherian, J. J. Jauregui, S. Banerjee, T. Pierce, and M. A. Mont, "What host factors affect aseptic loosening after THA and TKA?," *Clinical Orthopaedics and Related Research*, vol. 473, no. 8, pp. 2700-2709, 2015.
- [3] O. Camuzard, V. Breuil, G. F. Carle, and V. Pierrefite-Carle, "Autophagy involvement in aseptic loosening of arthroplasty components," *The Journal of Bone and Joint Surgery. American Volume*, vol. 101, no. 5, pp. 466-472, 2019.
- [4] P. H. Wooley and E. M. Schwarz, "Aseptic loosening," *Gene Therapy*, vol. 11, no. 4, pp. 402-407, 2004.

- [5] L. A. Cordova, V. Stresing, B. Gobin et al., "Orthopaedic implant failure: aseptic implant loosening—the contribution and future challenges of mouse models in translational research," *Clinical Science (London, England)*, vol. 127, no. 5, pp. 277–293, 2014.
- [6] J. J. Jacobs, N. J. Hallab, R. M. Urban, and M. A. Wimmer, "Wear Particles," *The Journal of Bone and Joint Surgery-American Volume*, vol. 88, pp. 99–102, 2006.
- [7] H. Jiang, Y. Wang, Z. Deng et al., "Construction and Evaluation of a Murine Calvarial Osteolysis Model by Exposure to CoCrMo Particles in Aseptic Loosening," *Journal of Visualized Experiments*, no. 132, 2018.
- [8] Z. Deng, Z. Wang, J. Jin et al., "SIRT1 protects osteoblasts against particle-induced inflammatory responses and apoptosis in aseptic prosthesis loosening," *Acta Biomaterialia*, vol. 49, pp. 541–554, 2017.
- [9] L. M. Wise, S. D. Waldman, M. Kasra et al., "Effect of zoledronate on bone quality in the treatment of aseptic loosening of hip arthroplasty in the dog," *Calcified Tissue International*, vol. 77, no. 6, pp. 367–375, 2005.
- [10] M. J. Coathup, J. Blackburn, A. E. Goodship, J. L. Cunningham, T. Smith, and G. W. Blunn, "Role of hydroxyapatite coating in resisting wear particle migration and osteolysis around acetabular components," *Biomaterials*, vol. 26, no. 19, pp. 4161–4169, 2005.
- [11] S. B. Goodman, Y. Song, J. Y. Yoo et al., "Local infusion of FGF-2 enhances bone ingrowth in rabbit chambers in the presence of polyethylene particles," *Journal of Biomedical Materials Research. Part A*, vol. 65A, no. 4, pp. 454–461, 2003.
- [12] T. Ma, Z. Huang, P. G. Ren et al., "An in vivo murine model of continuous intramedullary infusion of polyethylene particles," *Biomaterials*, vol. 29, no. 27, pp. 3738–3742, 2008.
- [13] S. Y. Yang, L. Mayton, B. Wu, J. J. Goater, E. M. Schwarz, and P. H. Wooley, "Adeno-associated virus-mediated osteoprotegerin gene transfer protects against particulate polyethylene-induced osteolysis in a murine model," *Arthritis and Rheumatism*, vol. 46, no. 9, pp. 2514–2523, 2002.
- [14] N. Liu, J. Meng, Z. Wang, G. Zhou, T. Shi, and J. Zhao, "Autophagy mediated TiAl 6 V 4 particle-induced peri-implant osteolysis by promoting expression of TNF- α ," *Biochemical and Biophysical Research Communications*, vol. 473, no. 1, pp. 133–139, 2016.
- [15] Z. Wang, N. Liu, T. Shi et al., "ER stress mediates TiAl6V4 particle-induced peri-implant osteolysis by promoting RANKL expression in fibroblasts," *PLoS One*, vol. 10, no. 9, article e0137774, 2015.
- [16] Z. Wang, Z. Deng, J. Gan et al., "TiAl 6 V 4 particles promote osteoclast formation via autophagy-mediated downregulation of interferon-beta in osteocytes," *Acta Biomaterialia*, vol. 48, pp. 489–498, 2017.
- [17] S. Chen, G. Jin, K.-M. Huang et al., "Lycorine suppresses RANKL-induced osteoclastogenesis in vitro and prevents ovariectomy-induced osteoporosis and titanium particle-induced osteolysis in vivo," *Scientific Reports*, vol. 5, no. 1, 2015.
- [18] C. Neuerburg, C. Wedemeyer, J. Goedel et al., "The role of calcitonin receptor signalling in polyethylene particle-induced osteolysis," *Acta Biomaterialia*, vol. 14, pp. 125–132, 2015.
- [19] W. G. Goodman, "Bone disease and aluminum: pathogenic considerations," *American Journal of Kidney Diseases*, vol. 6, no. 5, pp. 330–335, 1985.
- [20] M. del Pilar Martínez, C. Bozzini, M. I. Olivera, G. Dmytrenko, and M. I. Conti, "Aluminum bone toxicity in immature rats exposed to simulated high altitude," *Journal of Bone and Mineral Metabolism*, vol. 29, no. 5, pp. 526–534, 2011.
- [21] G. O. Alrabeah, P. Brett, J. C. Knowles, and H. Petridis, "The effect of metal ions released from different dental implant-abutment couples on osteoblast function and secretion of bone resorbing mediators," *Journal of Dentistry*, vol. 66, pp. 91–101, 2017.
- [22] Z. Deng, J. Jin, Z. Wang, Y. Wang, Q. Gao, and J. Zhao, "The metal nanoparticle-induced inflammatory response is regulated by SIRT1 through NF-kappaB deacetylation in aseptic loosening," *International Journal of Nanomedicine*, vol. - Volume 12, pp. 3617–3636, 2017.
- [23] L. Liu, M. Zhou, R. Zhu et al., "Hydrogen sulfide protects against particle-induced inflammatory response and osteolysis via SIRT1 pathway in prosthesis loosening," *The FASEB Journal*, vol. 34, no. 3, pp. 3743–3754, 2020.

Research Article

Impact of Acute Pancreatic Injury on Sphingolipid Metabolism in the Salivary Glands

Małgorzata Żendzian-Piotrowska,¹ Dominika M. Ziembicka,² Bartłomiej Łukaszuk³ and Krzysztof Kurek⁴

¹Department of Hygiene, Epidemiology and Ergonomics, Medical University of Białystok, Poland

²Department of Public Health, Medical University of Białystok, Poland

³Department of Physiology, Medical University of Białystok, Poland

⁴Department of Gastroenterology and Internal Medicine, Medical University of Białystok, Poland

Correspondence should be addressed to Krzysztof Kurek; krzysztof.kurek@umb.edu.pl

Received 27 April 2020; Accepted 22 July 2020; Published 5 August 2020

Academic Editor: Monica Fedele

Copyright © 2020 Małgorzata Żendzian-Piotrowska et al. This is an open access article distributed under the Creative Commons Attribution License, which permits unrestricted use, distribution, and reproduction in any medium, provided the original work is properly cited.

Acute pancreatic injury can be related to both parenchymal (responsible for exocrine functions) and islet (mainly β -cells, responsible for endocrine functions) damage. During embryonic development, both the salivary glands and the pancreas originate from the foregut, which explains many of the observed histological and functional similarities between these two organs. The relationship between several diseases of the pancreas and salivary glands, resulting from morphological and functional similarities, is well established. Sphingolipids constitute a class of biologically active molecules involved in numerous physiological and pathological processes, including acute pancreatitis (AP) and diabetes mellitus. However, the effect of AP on sphingolipid metabolism in the salivary glands remains uncertain. In the presented study, we examined the effect of AP and type 1 diabetes mellitus on sphingolipid metabolism in the salivary glands of rats. We demonstrated that acute pancreatic injury, related to both exocrine and endocrine functions, affects the metabolism of sphingolipids in the parotid, but not submandibular, salivary glands.

1. Introduction

The salivary glands of mammals are exocrine glands, the main function of which is saliva production. Both in humans and rodents, three pairs of macroscopic glands—parotid, submandibular, and sublingual—have been described [1]. Interestingly, during embryonic development, both the salivary glands and the pancreas originate from the foregut, which explains many of the observed histological and functional similarities between these two organs [2, 3]. The secretory end pieces of the salivary glands as well as the pancreas are the acini which produce and secrete saliva or pancreatic juice and bicarbonates into the ductal system of each gland [4]. The second resemblance between the described organs is the secretion of the digestive enzyme α -amylase in both

the pancreas and the salivary glands [5]. In addition to exocrine function, the pancreas also serves as an endocrine gland, stabilizing the blood glucose level by the release of insulin, a hormone produced by beta-cells (β -cells) in the islets of Langerhans.

Acute pancreatic injury can be related to both parenchymal (responsible for exocrine functions) and islet (mainly β -cells, responsible for endocrine functions) damage. In the presence of the former, the disease called acute pancreatitis (AP) is one of the most common gastrointestinal disorders. The reported annual incidence of AP ranges from 4.9 to 35 cases per 100,000 people [6]. Pancreatic inflammation activates a cytokine cascade, which often leads to the development of systemic inflammatory response syndrome (SIRS) [7]. A prolonged duration of SIRS increases the risk of

multiorgan dysfunction syndrome (MODS), a condition associated with a high mortality rate of up to 39% [8].

It has been observed that AP tends to coincide with type 1 diabetes mellitus (T1DM). It was estimated that up to 40–60% of patients with severe AP develop T1DM [9]. On the other hand, the risk of AP increases in only 1% of T1DM patients [9]. The presented data indicate a strong relationship between AP and T1DM considering the common pathogenesis of these diseases. However, the pathogenesis of AP and T1DM has not been thoroughly explained. It is believed that one of its possible factors may be alterations in sphingolipid metabolism, which has been recently proven in both human and animal models [10, 11].

Sphingolipids (Figure 1) constitute a class of biologically active molecules with a well-established involvement in numerous physiological and pathological processes [12, 13]. Ceramide, which is a central molecule and the main messenger of the sphingomyelin signaling pathway, is a lipid particle able to stimulate and regulate the activities of numerous enzymes [13–15]. To name just a few, (1) an overaccretion of ceramide has been shown to activate PP2A (protein phosphatase 2A), which impairs the insulin signaling pathway by dephosphorylation of threonine and serine molecules in PKB (protein kinase B) [16, 17], and (2) it is postulated that ceramide activates JNKs (c-Jun N-terminal kinases) and IKK (inducer of κ kinase), i.e., the enzymes playing a pivotal role in response to stress stimuli and development of inflammation [18].

Intracellular ceramide primarily originates from the de novo synthesis pathway or follows hydrolysis of sphingomyelin [19]. The activation of the sphingomyelin signaling pathway was proven to be involved in the regulation of cell differentiation, proliferation, or even necrosis as well as programmed cell death (apoptosis) [17, 20]. On the other hand, ceramide downstream metabolite sphingosine-1-phosphate (S1P) presents the antagonizing effect on ceramide, forcing it to inhibit cell proliferation, apoptosis, and angiogenesis [14].

Recently, several studies concerning salivary gland lipid metabolism in the course of metabolic diseases have been performed. First of all, Matczuk et al. [21] observed that insulin resistance resulting from a chronic high-fat diet evokes the accumulation of triacylglycerides accompanied by a reduced phospholipid level in the salivary glands of rats [21]. Similar disturbances in lipid metabolism in the salivary glands of rats were observed in the course of streptozotocin-induced diabetes [22]. It was evidenced that the aforementioned changes led directly to salivary gland atrophy and progressive malfunction of the organ. Finally, in the study published by Garbowska et al. [23], activation of the sphingomyelin signaling pathway was observed in the salivary glands of rats in the course of type 1 diabetes induced by streptozotocin. The authors cited above also demonstrated inhibited sphingomyelin signal transduction in the salivary glands of rats subjected to chronic high-fat diet feeding [23]. However, the effect of AP on sphingolipid metabolism in the salivary glands remains unclear. To fulfill this gap of knowledge, we conducted an animal study on cerulein-induced AP and streptozotocin-induced type 1 diabetes to assess the

sphingolipid metabolism in the parotid and submandibular salivary glands.

2. Materials and Methods

2.1. Protocol of the Experiment. The implemented experimental procedures were approved by the Local Ethical Committee for Animal Experiments of the Medical University of Białystok. The studies were performed on the male Wistar rats obtained from a licensed breeder (age = 6 weeks, weight = 190 – 240 g). The rats were obtained from the MUB's Center for Experimental Medicine—certified by the Polish official agencies (https://www.umb.edu.pl/o_uczelni/centrum_medycyny_doswiadczalnej). The rodents were provided with the following conditions: stable temperature (21–22°C) and humidity and a 12/12 h light-dark cycle. All rats had unrestricted access to food and water. At the beginning of the experiment, the animals were randomly divided into 3 study groups:

- (1) Control (C) ($n = 10$)
- (2) Acute pancreatitis (AP) ($n = 10$)
- (3) Streptozotocin-induced diabetes (T1DM) ($n = 10$)

The rats assigned to the AP (acute pancreatic) group received cerulein (Sigma-Aldrich) at a dose of 50 $\mu\text{g}/\text{kg}$ of body weight, diluted in 1 mL of saline solution and administered in two intraperitoneal injections with 1-hour interval in accordance with the previously described method [11]. The occurrence of AP was then confirmed by assessing serum amylase and lipase activities 24 hours after the cerulein injections.

The animals from the T1DM (type 1 diabetes mellitus) group received streptozotocin (Sigma-Aldrich) dissolved in citrate buffer, pH 5.4, at a dose of 60 mg/kg of body weight, administered in an intraperitoneal injection according to the previously described method [15]. The injection was performed upon an overnight fasting 2 days prior to the planned final day of the experiment. The development of type 1 diabetes was then confirmed by measuring fasting glucose level 48 hours after streptozotocin administration.

The animals assigned to group C received intraperitoneally 1 mL of saline solution serving as a placebo.

At the end of the study (48 hours after the cerulein or streptozotocin injection), all rats were anesthetized after overnight fasting by an intraperitoneal pentobarbital injection at a dose of 80 mg/kg body weight and then sacrificed. The samples of both the parotid (PSG) and submandibular (SMSG) salivary glands were excised, immediately frozen between aluminum clamps, precooled in liquid nitrogen, and stored at -80°C until further assays. Blood samples taken from the abdominal aorta were stored at -80°C until further analyses.

2.2. Serum Analyses. The activities of serum amylase and lipase as well as the concentration of serum C-reactive protein (CRP) were measured using commercially available laboratory kits (Abbott, USA). The serum glucose level was

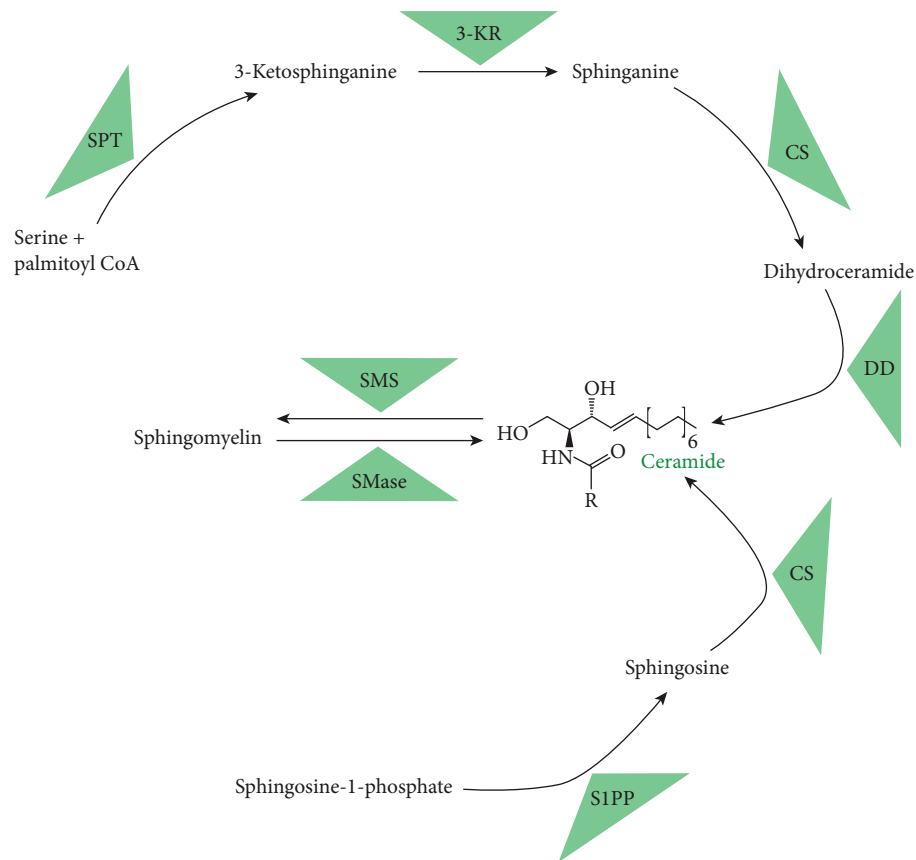


FIGURE 1: Schematic representation of the sphingomyelin signaling pathway. SPT: serine palmitoyl transferase; 3-KR: 3-ketosphinganine reductase; CS: ceramide synthase; DD: dihydroceramide desaturase; S1PP: sphingosine-1-phosphate phosphatase; SMS: sphingomyelin synthase; SMase: sphingomyelinase.

evaluated with Accu-Chek blood glucose meter (Bayer, Germany). Serum insulin concentration was measured using the chemiluminescence method with a commercial kit (Abbott, USA).

2.3. Concentration of Sphingomyelin (SM) in the Salivary Glands. At the beginning of the procedure, tissue samples were pulverized in a precooled aluminum mortar and transferred to tubes containing a solution of methanol and antioxidant (0.01% butylated hydroxytoluene). Then, lipid fractions were isolated in accordance with the method described in the work by Łukaszuk et al. [24]. Sphingomyelin was extracted using thin-layer chromatography (TLC). The gel bands were scraped off the plates upon examining their reference to the standards and transferred into tubes containing pentadecanoic acid used as an internal standard. After transmethylation, fatty acid components of sphingomyelin were analyzed using gas-liquid chromatography (GLC). The Hewlett-Packard 5890 Series II system equipped with a double flame-ionization detector and Agilent CP-Sil 88 capillary column was implemented. Total sphingomyelin concentration was expressed as the sum of individual fatty acid species (in nM/g of the tissue).

2.4. Concentration of Ceramide (Cer) in the Salivary Glands. Ceramide content in the salivary glands was assessed using

the method described by Garbowska et al. [23]. Briefly, a small portion of the chloroform phase was transferred to a fresh tube containing C17 sphingosine (Avanti Polar Lipids, UK) used as an internal standard. The organic phase containing ceramide was then hydrolyzed at 90°C for 60 minutes in the solution of 1M KOH in 90% methanol. The obtained sphingosine was subsequently analyzed using the high-performance liquid chromatography (HPLC) technique. N-Palmitoylsphingosine (Avanti Polar Lipids, UK) was applied as a standard for the preparation of the calibration curve. The assessed amount of ceramide was adjusted with respect to the level of free sphingosine in the sample.

2.5. Concentrations of Sphinganine (SFA), Sphinganine-1-Phosphate (SFA1P), Sphingosine (SFO), and Sphingosine-1-Phosphate (S1P) in the Salivary Glands. The concentrations of the abovementioned sphingolipids were measured in accordance with the method described by Min et al. [25]. At the beginning of the procedure, prior to the homogenization and ultrasonication of the samples, internal standards (C17 sphingosine and C17 sphingosine-1-phosphate) (Avanti Polar Lipids, UK) were added. Sphingoid bases were converted to their o-phthalaldehyde derivatives and then examined with a HPLC system (ProStar, Varian, Inc., USA) equipped with a fluorescence detector and reversed-phase C18 column (Varian, Inc., OmniSpher 5, 4.6 × 150 mm).

2.6. Statistical Analysis. The results were presented as mean \pm standard deviation (SD). Statistical differences between the groups ($n = 10$) were assessed using ANOVA with a subsequent post hoc test (Tukey HSD). Statistical significance was assumed at the level $p < 0.05$.

3. Results

3.1. Activities of Serum Amylase and Lipase: Concentrations of Serum C-Reactive Protein, Glucose, and Insulin (Table 1). Rats from group AP were characterized by significantly intensified activities of amylase and lipase compared to both groups C (+1.47 fold and +5.67 fold, respectively, $p < 0.05$) and T1DM (+1.64 fold and ~5 fold, respectively, $p < 0.05$). In group AP, serum CRP content was elevated in comparison with groups C (+10 fold, $p < 0.05$) and T1DM (+7.26 fold, $p < 0.05$). Furthermore, we noticed a significant increase in serum glucose in the T1DM group compared to both groups C (+4.1 fold, $p < 0.05$) and AP (+3.55 fold, $p < 0.05$). On the other hand, markedly decreased serum insulin concentration (below the detection level) was observed in T1DM rats compared to both groups C ($p < 0.05$) and AP ($p < 0.05$).

3.2. Concentration of Sphingomyelin in the Salivary Glands (Tables 2 and 3). In both the submandibular and parotid salivary glands, there were no differences in SM content between groups C and AP. However, a significant decrease in SM was noticed in group T1DM compared to C (-28% and -26% for submandibular and parotid salivary glands, respectively, $p < 0.05$) as well as in T1DM compared to AP (-29% and -24% for the submandibular and parotid salivary glands, respectively, $p < 0.05$).

3.3. Concentration of Ceramide in the Salivary Glands (Tables 2 and 3). In the SMSG, no significant differences in ceramide concentrations between any of the examined groups were observed. However, T1DM rats were characterized by a dramatic reduction in ceramide content in PSG compared to both groups C (-84%, $p < 0.05$) and AP (-89%, $p < 0.05$).

3.4. Concentration of Sphingosine in the Salivary Glands (Tables 2 and 3). There were no significant differences in SFO contents in SMSG of groups C and AP. However, in T1DM rats, we noted an increased SFO level in comparison with group C (+33%, $p < 0.05$). In PSG, the concentrations of SFO were considerably elevated in both groups AP (+26%, $p < 0.05$) and T1DM (+23%, $p < 0.05$) compared to group C.

3.5. Concentration of Sphinganine in the Salivary Glands (Tables 2 and 3). In the SMSG, there were no differences in sphinganine concentration between groups C and AP. However, we noticed a significant reduction in SFA content in SMSG of T1DM rats compared to group C (-48%, $p < 0.05$). In PSG, we observed a considerable increase of SFA content in both groups AP (+62%, $p < 0.05$) and T1DM (+138%, $p < 0.05$) compared to group C.

TABLE 1: Effect of acute pancreatic injury on changes in amylase and lipase activities, C-reactive protein, glucose, and insulin concentrations in serum (mean \pm SD).

Parameter	C	AP	DMt1
Amylase (IU)	1148 \pm 73	2831 \pm 387*	1072 \pm 54
Lipase (IU)	98 \pm 17	654 \pm 275*	110 \pm 29
CRP (mg/L)	7.6 \pm 3.2	84.3 \pm 18.2*	10.2 \pm 4.8
Glucose (mg/dL)	103.2 \pm 17	115.4 \pm 28	525 \pm 46*#
Insulin level (μ U/mL)	4.8 \pm 1.2	4.4 \pm 2.6	nd

C: control; AP: cerulein-induced acute pancreatitis; DMt1: streptozotocin-induced diabetes mellitus type 1. * $p < 0.05$ compared with the C group, # $p < 0.05$ compared with the AP group. CRP: C-reactive protein; nd: non detected.

3.6. Concentration of Sphingosine-1-Phosphate in the Salivary Glands (Tables 2 and 3). No differences in S1P concentration in SMSG between groups C and AP were observed. However, rats from the T1DM group were characterized by a significant reduction in the S1P level compared to both groups C (-43%, $p < 0.05$) and AP (-30%, $p < 0.05$). In PSG of T1DM rats, the concentration of S1P was considerably elevated compared to both groups C (+53%, $p < 0.05$) and AP (+24%, $p < 0.05$). In PSG, S1P content was markedly decreased in AP rats (-47%, $p < 0.05$) compared to group C.

3.7. Concentration of Sphinganine-1-Phosphate in the Salivary Glands (Tables 2 and 3). There were no differences in SFA1P content in SMSG between groups C and AP. However, in T1DM rats, we observed a significantly reduced level of SFA1P compared to both groups C (-38%, $p < 0.05$) and AP (-50%, $p < 0.05$). On the other hand, SFA1P concentration in PSG was markedly elevated in both AP (+70%, $p < 0.05$) and T1DM (+30%, $p < 0.05$) groups compared to group C.

4. Discussion

Our study investigates the relationship between the salivary gland sphingolipid signaling pathway in acute pancreatitis and streptozotocin-induced experimental diabetes. The pancreas and salivary glands have a similar anatomical structure as a consequence of their analogous embryonic development. It has been demonstrated that both the pancreas and the salivary glands are formed as a result of a controlled sequence of epithelial-mesenchymal mutual interactions. Moreover, both these types of glands serve a comparable function: they produce fluid rich in bicarbonates containing digestive enzymes and other ingredients to be delivered into the gut [26].

The relationship between several pancreatic and salivary gland diseases, resulting from morphological and functional similarities between these organs, is well established. First, it was demonstrated by Kamisawa et al. [26] that chronic pancreatitis of various etiologies frequently impairs the secretory function of the salivary glands, resulting in hyposalivation [26]. What is more, autoimmune diseases, such as autoimmune pancreatitis or IgG4-related disease, lead to progressive fibrosis and functional disturbances in both the

TABLE 2: Effect of acute pancreatic injury on sphingolipid concentration in the submandibular salivary gland (mean \pm SD) (pmol/mg, except for sphingomyelin which is expressed in nmol/g).

	C	AP	DMt1
SM	1528.85 \pm 71.489	1556.69 \pm 123.471	1108.07 \pm 82.822*#
CER	227.85 \pm 53.82	210.61 \pm 35.967	239.05 \pm 90.151
SFO	3.8 \pm 0.44	4.42 \pm 1.145	5.06 \pm 1.385*
SFA	0.31 \pm 0.037	0.32 \pm 0.073	0.16 \pm 0.038*#
S1P	0.28 \pm 0.117	0.23 \pm 0.065	0.16 \pm 0.038*#
SFA1P	0.26 \pm 0.042	0.32 \pm 0.091	0.16 \pm 0.046*#

C: control; AP: cerulein-induced acute pancreatitis; DMt1: streptozotocin-induced diabetes mellitus; *: vs. C ($p < 0.05$); #: vs. AP ($p < 0.05$). SM: sphingomyelin; CER: ceramide; SFO: sphingosine; SFA: sphinganine; S1P: sphingosine-1-phosphate; SFA1P: sphinganine-1-phosphate.

pancreas and the salivary glands [27]. In addition, Gokel et al. [28] found that toxic organophosphates induce not only acute pancreatitis (AP) but also parotitis—a state of inflammation affecting the parotid salivary glands [28]. It is worth mentioning at this point that viral infections, especially measles, which typically induce an inflammatory state in the salivary glands, can also affect the pancreas, leading to severe AP with a potentially fatal course [29]. On the other hand, in a study by Benini et al. [30] on lactoferrin concentration in saliva, no difference was observed in the saliva lactoferrin level between healthy subjects and patients with pancreatic cancer or chronic pancreatitis [30].

The relationship between acute pancreatitis and alterations in sphingolipid metabolism has attracted much attention in the recent decade. In the first study concerning the subject, Li et al. [31] observed the activation of sphingosine-1-kinase (SPHK1) enzymatic activity with concomitant increased S1P concentration in blood cells (neutrocytes, monocytes, and lymphocytes) obtained from the peripheral blood of patients with a severe form of AP. Furthermore, the authors demonstrated a positive correlation between S1P level and AP severity. Finally, they revealed reduced expression of SPHK1 to its baseline level during AP restoration, which suggests that S1P concentration could act as a marker of the disease activity [31]. These observations were recently confirmed in a study published by Konończuk et al. Briefly, in the rodent model of AP, it was noted that S1P concentration in pancreatic tissue samples was considerably elevated compared to the control group [11]. A similar increment was observed in the centrifuged plasma of patients with a severe form of AP [10]. Interestingly, S1P synthetic analogue, fingolimod, may represent a novel therapeutic strategy in preventing AP and its complications [32, 33]. However, the question whether AP leads to disturbances in the metabolism of sphingolipids in the salivary glands, which are morphologically and functionally similar to the pancreas, remains unanswered.

In the presented study, we used a widely accepted animal model of cerulein-induced AP in order to examine sphingolipid metabolism in the salivary glands in the course of the disease. Cerulein is a cholecystokinin analogue that triggers

AP via premature activation of trypsinogen within acinar cells, leading to excessive stimulation of pancreatic exocrine secretion [34]. In addition, there are no published data suggesting that cerulein stimulates the secretion of salivary amylase. Rats from our experiment were characterized by a significant increase in both amylase and lipase activities. These observations confirmed the development of AP and are consistent with the previously published results [35]. Furthermore, we noticed a considerable increase in CRP blood content in rats with cerulein-induced AP, which also confirms the previously published data. Increased CRP concentration is considered one of AP markers; it is therefore not surprising that in our experiment, we observed significantly elevated CRP concentration, as also evidenced by other researchers [36].

The most important and novel findings of our study were the observed changes in sphingolipid metabolism in the salivary glands in the course of AP and streptozotocin-induced diabetes. We narrowed our interests to two major types of salivary glands: the parotid and submandibular ones, which contribute up to 85% of unstimulated saliva flow (65% and 20% from the submandibular and parotid salivary glands, respectively) [37]. Surprisingly, we found no changes in the levels of particular sphingolipids in SMSG in the course of acute pancreatitis. In PSG, however, we observed significantly elevated levels of ceramide de novo synthesis precursors, sphinganine, and sphinganine-1-phosphate. The level of sphingosine, a downstream metabolite of ceramide, was also increased. On the other hand, S1P content remained decreased, which seems to contradict the elevated S1P level observed in the pancreatic tissue samples in the course of AP [11]. Finally, we demonstrated some changes in the content of particular sphingolipids in the salivary glands in the course of type 1 diabetes. In the sole paper on the aforementioned subject, Garbowska et al. [23] showed diversity in sphingolipid metabolism depending on the type of salivary gland [23]. Briefly, the cited authors showed increased S1P and SFA1P levels in streptozotocin-treated rats vs. control animals in the submandibular glands, while in the presented study, we found a decrease of the said sphingolipid particles. The same changes were noted in the parotid glands in which a significant upregulation of S1P, SFA, and SFO was observed, while in the study by Garbowska et al. [23], no changes were reported. Furthermore, we demonstrated considerably elevated levels of downstream metabolites of ceramide as well as SFO and S1P in PSG and decreased S1P content in SMSG. The parotid and submandibular glands represent two different types of metabolism: oxidative (PSG) and glycolytic (SMSG) [38]. The latter appears important given a different response pattern observed in some different tissues like skeletal muscles [12] and the salivary glands [22] in diabetic animals and at least partially explains the aforementioned differences.

Thus, we were the first to explore and describe the notion that acute pancreatic injury, both related to exocrine and endocrine functions, affects sphingolipid metabolism in the parotid, but not submandibular, salivary glands. This is in contrast to streptozotocin-induced diabetes, which could be associated with changes in the sphingolipid composition in

TABLE 3: Effect of acute pancreatic injury on sphingolipid concentration in the parotid salivary gland (mean \pm SD) (pmol/mg, except for sphingomyelin which is expressed in nmol/g).

	C	AP	DMt1
SM	1510.02 \pm 236.537	1482.35 \pm 197.289	1119.82 \pm 212.009*#
CER	411.89 \pm 105.358	361.01 \pm 68.006	67.05 \pm 10.754*#
SFO	3.67 \pm 0.354	4.64 \pm 0.743*	4.52 \pm 0.531*
SFA	0.13 \pm 0.033	0.21 \pm 0.037*	0.31 \pm 0.065*#
S1P	0.17 \pm 0.071	0.09 \pm 0.046*	0.26 \pm 0.074*#
SFA1P	0.1 \pm 0.012	0.17 \pm 0.051*	0.13 \pm 0.023*

C: control; AP: cerulein-induced acute pancreatitis; DMt1: streptozotocin-induced diabetes mellitus; *: vs. C ($p < 0.05$); #: vs. AP ($p < 0.05$). SM: sphingomyelin; CER: ceramide; SFO: sphingosine; SFA: sphinganine; S1P: sphingosino-1-phosphate; SFA1P: sphinganine-1-phosphate.

both analyzed salivary gland types. Nevertheless, it should be highlighted that alterations in the concentration of particular sphingolipids in the salivary glands differ from those observed in pancreatic tissue samples. While some previously published reports proved several changes in sphingolipid metabolism in peripheral blood in the course of AP in human subjects, no studies have been performed to assess sphingolipid changes in the salivary glands of diabetic patients. Thus, before the introduction of our results into the clinical practice, further studies on the subject are required.

Data Availability

All data achieved during our experiment are included in the tables attached to the manuscript.

Conflicts of Interest

The authors declare that they have no conflicts of interest.

Acknowledgments

This study was supported by the Medical University of Białystok, grant nos. N/ST/ZB/17/003/3330 and SUB/1/DN/19/003/3330.

References

- [1] O. Amano, K. Mizobe, Y. Bando, and K. Sakiyama, "Anatomy and histology of rodent and human major salivary glands: -overview of the japan salivary gland society-sponsored workshop-", *Acta Histochemica et Cytochemica*, vol. 45, no. 5, pp. 241–250, 2012.
- [2] M. H. Cleveland, J. M. Sawyer, S. Afelik, J. Jensen, and S. D. Leach, "Exocrine ontogenies: On the development of pancreatic acinar, ductal and centroacinar cells," *Seminars in Cell & Developmental Biology*, vol. 23, no. 6, pp. 711–719, 2012.
- [3] J. Harunaga, J. C. Hsu, and K. M. Yamada, "Dynamics of salivary gland Morphogenesis," *Journal of Dental Research*, vol. 90, no. 9, pp. 1070–1077, 2011.
- [4] C. A. Pinkstaff, "The Cytology of Salivary Glands," *International Review of Cytology*, vol. 63, pp. 141–261, 1980.
- [5] R. Racz, A. Nagy, Z. Rakonczay, E. K. Dunavari, G. Gerber, and G. Varga, "Defense Mechanisms Against Acid Exposure by Dental Enamel Formation, Saliva and Pancreatic Juice Production," *Current Pharmaceutical Design*, vol. 24, no. 18, pp. 2012–2022, 2018.
- [6] P. G. Lankisch, M. Apte, and P. A. Banks, "Acute pancreatitis," *The Lancet*, vol. 386, no. 9988, pp. 85–96, 2015.
- [7] V. K. Singh, B. U. Wu, T. L. Bollen et al., "Early Systemic Inflammatory Response Syndrome Is Associated With Severe Acute Pancreatitis," *Clinical Gastroenterology and Hepatology*, vol. 7, no. 11, pp. 1247–1251, 2009.
- [8] J. A. Windsor and M. S. Petrov, "Acute pancreatitis reclassified," *Gut*, vol. 62, no. 1, pp. 4–5, 2013.
- [9] N. G. Forouhi and N. J. Wareham, "Epidemiology of diabetes," *Medicine*, vol. 42, no. 12, pp. 698–702, 2014.
- [10] T. Konończuk, B. Łukaszuk, M. Żendzian-Piotrowska et al., "Plasma Sphingolipids in Acute Pancreatitis," *International Journal of Molecular Sciences*, vol. 18, no. 12, p. 2606, 2017.
- [11] T. Konończuk, B. Łukaszuk, A. Mikłosz, A. Chabowski, M. Żendzian-Piotrowska, and K. Kurek, "Cerulein-Induced Acute Pancreatitis Affects Sphingomyelin Signaling Pathway in Rats," *Pancreas*, vol. 47, no. 7, pp. 898–903, 2018.
- [12] K. Kurek, M. Garbowska, D. M. Ziembicka et al., "Myriocin treatment affects lipid metabolism in skeletal muscles of rats with streptozotocin-induced type 1 diabetes," *Advances in Medical Sciences*, vol. 62, no. 1, pp. 65–73, 2017.
- [13] Y. A. Hannun and L. M. Obeid, "Sphingolipids and their metabolism in physiology and disease," *Nature Reviews Molecular Cell Biology*, vol. 19, no. 3, pp. 175–191, 2018.
- [14] B. Ogretmen, "Sphingolipid metabolism in cancer signalling and therapy," *Nature Reviews. Cancer*, vol. 18, no. 1, pp. 33–50, 2018.
- [15] K. Kurek, P. Wiesiołek-Kurek, D. M. Piotrowska, B. Łukaszuk, A. Chabowski, and M. Żendzian-Piotrowska, "Inhibition of Ceramide De Novo Synthesis with Myriocin Affects Lipid Metabolism in the Liver of Rats with Streptozotocin-Induced Type 1 Diabetes," *BioMed Research International*, vol. 2014, Article ID 980815, 10 pages, 2014.
- [16] P. J. Larsen and N. Tennagels, "On ceramides, other sphingolipids and impaired glucose homeostasis," *Molecular Metabolism*, vol. 3, no. 3, pp. 252–260, 2014.
- [17] K. Kurek, A. Mikłosz, B. Łukaszuk, A. Chabowski, J. Górski, and M. Żendzian-Piotrowska, "Inhibition of Ceramide De Novo Synthesis Ameliorates Diet Induced Skeletal Muscles Insulin Resistance," *Journal of Diabetes Research*, vol. 2015, Article ID 154762, 9 pages, 2015.
- [18] N. Turner, G. J. Cooney, E. W. Kraegen, and C. R. Bruce, "Fatty acid metabolism, energy expenditure and insulin

- resistance in muscle,” *The Journal of Endocrinology*, vol. 220, no. 2, pp. T61–T79, 2014.
- [19] K. Hanada, “Serine palmitoyltransferase, a key enzyme of sphingolipid metabolism,” *Biochimica et Biophysica Acta (BBA) - Molecular and Cell Biology of Lipids*, vol. 1632, no. 1–3, pp. 16–30, 2003.
- [20] A. Mikłosz, B. Łukaszuk, A. Chabowski, F. Rogowski, K. Kurek, and M. Zendzian-Piotrowska, “Hyperthyroidism evokes myocardial ceramide accumulation,” *Cellular Physiology and Biochemistry*, vol. 35, no. 2, pp. 755–766, 2015.
- [21] J. Matczuk, A. Zalewska, B. Łukaszuk et al., “Insulin resistance and obesity affect lipid profile in the salivary glands,” *Journal of Diabetes Research*, vol. 2016, Article ID 8163474, 9 pages, 2016.
- [22] J. Matczuk, A. Zalewska, B. Łukaszuk et al., “Effect of streptozotocin-induced diabetes on lipids metabolism in the salivary glands,” *Prostaglandins & Other Lipid Mediators*, vol. 126, pp. 9–15, 2016.
- [23] M. Garbowska, B. Łukaszuk, A. Mikłosz et al., “Sphingolipids metabolism in the salivary glands of rats with obesity and streptozotocin induced diabetes,” *Journal of Cellular Physiology*, vol. 232, no. 10, pp. 2766–2775, 2017.
- [24] B. Łukaszuk, A. Mikłosz, M. Zendzian-Piotrowska, B. Wojcik, J. Gorski, and A. Chabowski, “Changes in the diaphragm lipid content after administration of Streptozotocin and high-fat diet regime,” *Journal of Diabetes Research*, vol. 2017, Article ID 3437169, 12 pages, 2017.
- [25] J.-K. Min, H.-S. Yoo, E.-Y. Lee, W.-J. Lee, and Y.-M. Lee, “Simultaneous Quantitative Analysis of Sphingoid Base 1-Phosphates in Biological Samples by o-Phthalaldehyde Pre-column Derivatization after Dephosphorylation with Alkaline Phosphatase,” *Analytical Biochemistry*, vol. 303, no. 2, pp. 167–175, 2002.
- [26] T. Kamisawa, Y. Tu, N. Egawa, N. Sakaki, S. Inokuma, and N. Kamata, “Salivary gland involvement in chronic pancreatitis of various etiologies,” *The American Journal of Gastroenterology*, vol. 98, no. 2, pp. 323–326, 2003.
- [27] K. Miyabe, Y. Zen, L. D. Cornell et al., “Gastrointestinal and Extra-Intestinal Manifestations of IgG4-Related Disease,” *Gastroenterology*, vol. 155, no. 4, pp. 990–1003.e1, 2018.
- [28] Y. Gokel, B. Gulalp, and A. Acikalin, “Parotitis due to organophosphate intoxication,” *Journal of Toxicology: Clinical Toxicology*, vol. 40, no. 5, pp. 563–565, 2002.
- [29] P. A. Vargas, F. D. Bernardi, V. A. Alves et al., “Uncommon histopathological findings in fatal measles infection: pancreatitis, sialoadenitis and thyroiditis,” *Histopathology*, vol. 37, no. 2, pp. 141–146, 2000.
- [30] L. Benini, R. F. Harvey, I. Vantini et al., “Lactoferrin concentration in the parotid saliva of patients with chronic pancreatitis,” *Digestion*, vol. 28, no. 2, pp. 77–81, 1983.
- [31] Q. Li, C. Wang, Q. Zhang, C. Tang, N. Li, and J. Li, “The Role of Sphingosine Kinase 1 in Patients with Severe Acute Pancreatitis,” *Annals of Surgery*, vol. 255, no. 5, pp. 954–962, 2012.
- [32] H.-B. Liu, N.-Q. Cui, Q. Wang, D.-H. Li, and X.-P. Xue, “Sphingosine-1-phosphate and its analogue fty720 diminish acute pulmonary injury in rats with acute necrotizing pancreatitis,” *Pancreas*, vol. 36, no. 3, pp. e10–e15, 2008.
- [33] C. A. Müller, O. Belyaev, W. Burr et al., “Effects of fty720 and rapamycin on inflammation in taurocholate-induced acute pancreatitis in the rat,” *Pancreas*, vol. 41, no. 7, pp. 1086–1091, 2012.
- [34] T. Otani and A. Matsukura, “Premature Trypsinogen Activation During Cerulein Pancreatitis in Rats Occurs Inside Pancreatic Acinar Cells,” *Pancreas*, vol. 20, no. 4, pp. 421–422, 2000.
- [35] Z. Warzecha, P. Sendur, P. Ceranowicz et al., “Protective effect of pretreatment with acenocoumarol in cerulein-induced acute pancreatitis,” *International Journal of Molecular Sciences*, vol. 17, no. 10, p. 1709, 2016.
- [36] X. Kang, X.-G. Lu, L.-B. Zhan et al., “Dai-huang-fu-zi-tang alleviates pulmonary and intestinal injury with severe acute pancreatitis via regulating aquaporins in rats,” *BMC Complementary and Alternative Medicine*, vol. 17, no. 1, p. 288, 2017.
- [37] S. P. Humphrey and R. T. Williamson, “A review of saliva: Normal composition, flow, and function,” *The Journal of Prosthetic Dentistry*, vol. 85, no. 2, pp. 162–169, 2001.
- [38] F. K. Ibuki, A. Simões, and F. N. Nogueira, “Antioxidant enzymatic defense in salivary glands of streptozotocin-induced diabetic rats: a temporal study,” *Cell Biochemistry and Function*, vol. 28, no. 6, pp. 503–508, 2010.

Research Article

Resveratrol Improves Hepatic Redox Status and Lipid Balance of Neonates with Intrauterine Growth Retardation in a Piglet Model

Kang Cheng, Shuli Ji, Peilu Jia, Hao Zhang, Ting Wang, Zhihua Song, Lili Zhang , and Tian Wang 

College of Animal Science and Technology, Nanjing Agricultural University, Nanjing 210095, China

Correspondence should be addressed to Lili Zhang; zhanglili@njau.edu.cn and Tian Wang; tianwangnjau@163.com

Received 9 April 2020; Accepted 30 June 2020; Published 18 July 2020

Academic Editor: Monica Fedele

Copyright © 2020 Kang Cheng et al. This is an open access article distributed under the Creative Commons Attribution License, which permits unrestricted use, distribution, and reproduction in any medium, provided the original work is properly cited.

Abnormal lipid metabolism, oxidative stress (OS), and inflammation play a pivotal role in the increased susceptibility to neonatal fatty liver diseases associated with intrauterine growth retardation (IUGR). This study was firstly conducted to investigate whether resveratrol could alleviate IUGR-induced hepatic lipid accumulation, alteration of redox and immune status in a sucking piglet model and explore the possible mechanisms at transcriptional levels. A total of 36 pairs of 7 d old male normal birth weight (NBW) and IUGR piglets were orally fed with either 80 mg resveratrol/kg body weight/d or 0.5% carboxymethylcellulose sodium for a period of 14 days, respectively. Compared with the NBW piglets, the IUGR piglets displayed compromised growth performance and liver weight, reduced plasma free fatty acid (FFA) level, increased hepatic OS, abnormal hepatic lipid accumulation and weakened hepatic immune function, and hepatic aberrant transcriptional expression of some genes such as heme oxygenase 1, superoxide dismutase 1, sterol regulatory element-binding protein 1c, stearoyl-CoA desaturase 1, liver fatty acid-binding proteins 1, toll-like receptor 4, and tumor necrosis factor alpha (TNF- α). Oral administration of resveratrol to piglets decreased the levels of FFA and total triglycerides (TG) in the plasma and hepatic TNF- α concentration, and increased glutathione reductase activity and reduced glutathione level in the liver. Resveratrol restored the increased alanine aminotransferase activity in the plasma of IUGR piglets. Treatment with resveratrol ameliorated the increased hepatic malondialdehyde, protein carbonyl, TG, and FFA concentrations induced by IUGR. Resveratrol treatment alleviated the reduced lipoprotein lipase activity and its mRNA expression as well as TNF- α gene expression in the liver of IUGR piglets. Hepatic glutathione peroxidase 1 and monocyte chemoattractant protein 1 genes expression of piglets was upregulated by oral resveratrol administration. In conclusion, resveratrol administration plays a beneficial role in hepatic redox status and lipid balance of the IUGR piglets.

1. Introduction

Metabolic syndrome (MS) is a cluster of metabolic disorders including obesity, hypertension, dyslipidemia, hyperglycemia, and insulin resistance [1, 2] and is a contributor to the deaths resulting from noncommunicable diseases such as diabetes and cardiovascular disease [2]. In the etiology of these diseases, excessive fat storage in nonadipose tissues (e.g., liver) is a risk factor [3]. Ectopic deposition of lipid in hepatocytes is the result of an increased free fatty acid input correlated with its inefficient β -oxidation, esterification, or both [4, 5]. Of note, excellent antioxidative and immune status is beneficial for the biological oxidative phosphorylation

of glycolipid substrate, which is very important for maintaining lipid balance. With the exception of diet and lifestyle, birth weight (BW) is also regarded as the main link between abnormal accumulation of lipid in the liver and the increased incidence of MS and its related diseases [6]. A large number of epidemiological and animal studies have shown that lower BW induced by intrauterine growth retardation (IUGR) is associated with elevated risk for the development of nonalcoholic fatty liver disease (NAFLD) in both children and adults [7–10]. Pigs were widely used as an animal model for IUGR studies in humans due to their biological similarity to humans [11]. Furthermore, the spontaneous occurrence of IUGR in pigs is similar to that of humans, which is mainly

caused by placental insufficiency [12, 13]. In previous studies, IUGR pigs exhibited insulin resistance [14, 15] and increased lipid level [15, 16], oxidative stress (OS) [16, 17], and abnormal inflammation [18, 19] in the liver from birth to adulthood at different stages of growth. Therefore, improving hepatic lipid metabolism, redox and immune status in an IUGR piglet model may help in developing new strategies for IUGR infants to prevent or/and slow the progression of NAFLD.

Resveratrol (RSV, 3, 5, 4'-trihydroxystilbene) was isolated from various type of plants such as peanuts, grapes, and *Polygonum cuspidatum*. A body of evidence in preclinical studies showed that resveratrol can treat high-fat diet-induced NAFLD by decreasing OS, inhibiting inflammation, and regulating lipid metabolism [4, 5]. Of course, RSV has been reported to exert a critical role in diet-induced MS associated with disease models such as cognitive impairment [20], osteoarthritis [21], nephropathy [22], and cardiovascular disease [23]. However, until now, no available research has been conducted to investigate the beneficial effect of RSV on the status of lipid, redox, and immunity in the liver of IUGR piglets. Therefore, the effect of RSV on hepatic lipid metabolism, OS, and inflammation of IUGR newborn piglets was firstly explored.

2. Materials and Methods

The experiment was carried out according to the guidelines of the Ethics Committee of Nanjing Agricultural University for the use of animals in research.

2.1. Animal and Experimental Design. During the preparation, healthy sows (Landrace × Yorkshire) with the same parity of the third and similar expected days of farrowing (<3 d) were chosen. At birth, sows that had similar litter sizes (i.e., 11–13 piglets) and met the selection criteria for IUGR piglets were chosen. A total of 72 male newborn piglets (Duroc × (Landrace × Yorkshire)) were collected and tagged from 36 litters (1 normal birth weight (NBW) piglet and 1 IUGR piglet from 1 litter) for the experiment: 36 were NBW piglets (~1.72 kg) and the other 36 were naturally occurring IUGR littermates (~0.88 kg) according to their birth weight using our previous method [24]. An IUGR piglet was defined as having a birth weight which was 2 SD below the mean BW of the total population, whereas a NBW littermate had a birth weight within 0.5 SD unit of the mean birth weight of the whole litter. The NBW and IUGR piglets were cross-fostered after birth by 24 four-parity sows (standardized litters: 3 experimental piglets and 8 same type nonexperimental piglets). At 7 days of age, the NBW and IUGR piglets were orally fed with 80 mg RSV/kg body weight/d (purity 98%; Zhejiang Yixin Pharmaceutical Co., Ltd, China; diluted in 0.5% carboxymethylcellulose sodium (CMC-Na)) or the same volume of 0.5% CMC-Na (Sinopharm Chemical Reagent Co., Ltd., Shanghai, China; diluted in 0.86% saline) for a period of 14 days, respectively. Therefore, all piglets were assigned into 4 groups (6 replicate per group, 3 piglets per replicate): NBW-CON, NBW-RSV, IUGR-CON, and IUGR-RSV. During the whole experimental period, all piglets remained with sows. The whole animal experiment was

conducted in an experimental farm of Anyou Biotechnology Group (Taicang, China). During the pregnancy and lactation, sows are fed and managed according to standard procedures of the experimental farm. The piglets' average body weight (ABW) was recorded carefully.

2.2. Sample Collection. At 21 days of postnatal age, 1 piglet per replicate (6 piglets per treatment) was selected to collect a heparinized blood sample from the anterior vena cava after fasting for 8 h. The plasma was obtained by centrifugation at 2000×g for 20 min at 4°C and stored at -20°C until assays. After then, these piglets were killed as we previously described [25], and the liver (right lobe) sample was immediately collected and stored at -80°C for further analysis.

2.3. Plasma Biochemical Parameter Analysis. In the plasma, total triglycerides (TG), total cholesterol (TC), high-density lipoprotein cholesterol (HDL-C), low-density lipoprotein cholesterol (LDL-C), glucose (Glu) and free fatty acid (FFA) levels, and alanine aminotransferase (ALT) and aspartate aminotransferase (AST) activities were determined by commercial kits (Nanjing Jiancheng Institute of Bioengineering, Nanjing, China). A commercial enzyme-linked immunosorbent assay (ELISA) kit (CUSABIO Biotech, Wuhan, China) was used to measure the plasma insulin level. The sensitivity limit of insulin determination was 1 μIU/mL, and the inter- and intra-assay coefficients of variation were less than 15%. The homeostasis model assessment of insulin resistance (HOMA-IR) was used to calculate insulin resistance according to the following formula: HOMA-IR = fasting plasma insulin (μU/mL) × fasting plasma glucose (mmol/L)/22.5 [26].

2.4. Hepatic Lipid Metabolism Parameters. The levels of TG, TC, and FFA and the activities of lipoprotein lipase (LPL), hepatic lipase (HL), and total lipase (TL) in the liver were determined according to the instructions of the manufacturer (Nanjing Jiancheng Institute of Bioengineering, Nanjing, China). These results were normalized to the total protein concentration in each sample for intersample comparison. Hepatic protein concentration was detected according to the Bradford method [27].

2.5. Determination of Hepatic Redox Status. The contents of malondialdehyde (MDA), protein carbonyl (PC), and reduced glutathione (GSH) and the activities of total superoxide dismutase (T-SOD), glutathione peroxidase (GPX), and glutathione reductase (GR) were measured by using assay kits purchased from the Nanjing Jiancheng Institute of Bioengineering (Nanjing, China) following the guidelines of the manufacturer. All parameters related to redox status were normalized against protein content in each sample for intersample comparison. The protein concentrations in the liver homogenate were quantified following the Bradford method [27].

2.6. Hepatic Cytokine Concentration Assays. The production of tumor necrosis factor alpha (TNF-α) was measured using an ELISA kit (Beijing Solarbio Science & Technology Co., Ltd., Beijing, China), which was performed according to the manufacturer's protocol. The detection limits were 5 pg/mL;

the inter- and intra-assay coefficients of variation were less than 10%. All results were normalized to the total protein concentration in each sample for intersample comparison. Hepatic protein concentration was detected according to the Bradford method [27].

2.7. mRNA Expression. Total RNA isolation, reverse transcription, and quantitative real-time PCR (qRT-PCR) analysis were carried out as described previously [5, 28]. The primers used for qRT-PCR are presented in Table 1. The $2^{-\Delta\Delta C_t}$ method was used to calculate the mRNA expression levels of target genes relative to the housekeeping gene β -actin, as described previously [29]. The values of the NBW-CON group were regarded as a calibrator.

2.8. Statistical Analysis. Two-way ANOVA was used to determine the main effects (BW and RSV) and their interaction using the general linear model procedure of SPSS software (version 20.0; SPSS Inc.). When a significant interaction between BW and RSV treatment was observed, post hoc testing was conducted using Turkey's multiple comparison test. The individual piglet was used as the experimental unit with the exception of growth performance. Data are presented as means with their standard errors. Differences were considered significant at $P < 0.05$, and $0.05 < P < 0.10$ were considered a trend.

3. Results

3.1. RSV Does Not Affect the Growth Performance but Improves the Circulatory Metabolism of Piglets. The IUGR piglets had lower ABW and liver weight but exhibited higher liver relative weight compared with the NBW piglets ($P < 0.05$, Table 2). However, RSV had no effects on the growth performance and organ weight of the piglets ($P > 0.05$). There is a significant interaction between BW and RSV treatment for the plasma TG level ($P < 0.05$, Table 3). Oral RSV reduced ($P < 0.05$) the level of plasma TG in the NBW piglets rather than in the IUGR piglets. Compared with NBW, IUGR decreased the concentration of FFA in the plasma of piglets ($P < 0.05$). Oral administration of RSV decreased the levels of FFA ($P < 0.05$), TG ($P < 0.05$), and Glu ($P = 0.061$) in the plasma of piglets. However, BW and RSV had no effects on HDL-C, LDL-C, TC, insulin, and HOMA-IR levels ($P > 0.05$).

3.2. RSV Alleviates Hepatic Injury of IUGR Piglets. Amino-transferase activities in the circulatory system are considered as reliable markers of hepatic damage. We measured ALT and AST activities in the plasma and found that BW and RSV treatment had a significant interaction effect on the plasma ALT activity in piglets ($P < 0.05$, Figure 1(b)). Resveratrol restored the increased ALT activity in the plasma of IUGR piglets ($P < 0.05$). There was no significant difference in the plasma AST activity of piglets among these groups ($P > 0.05$, Figure 1(a)).

3.3. RSV Affects the Hepatic Lipid Metabolism of Piglets. The imbalance of lipid metabolism is an important driver to hepatic dysfunction and damage of the IUGR individuals. Thus, we evaluated the effect of RSV on the hepatic lipid

metabolism of the IUGR piglets. Compared with the NBW piglets, IUGR increased TG and FFA levels and decreased LPL, HL, and TL activities in the liver of piglets ($P < 0.05$, Figures 2(a) and 2(c)–2(f)). Administration of RSV to piglets reduced TG and FFA levels and increased LPL activity in the liver ($P < 0.05$). In addition, BW and RSV treatment had significant interaction effects on LPL activity and the levels of TG and FFA in the liver of piglets ($P < 0.05$). Resveratrol treatment ameliorated the increased TG and FFA levels and the reduced LPL activity in the liver of IUGR piglets ($P < 0.05$).

The mRNA abundance of sterol regulatory element-binding protein 1c (SREBP1c, $P = 0.091$, Figure 3), stearoyl-CoA desaturase 1 (SCD1, $P = 0.073$), and liver fatty acid-binding proteins 1 (L-FABP1, $P < 0.05$) were increased by IUGR compared with NBW. A tendency for the increased ($P = 0.081$) expression of the hepatic LPL gene was found in the piglets exposed to RSV treatment. A significant interaction ($P < 0.05$) between BW and RSV treatment was observed in the hepatic mRNA expression of peroxisome proliferator-activated receptor alpha, microsomal triglyceride transfer protein, cluster of differentiation 36, fatty acid transport proteins 1, and L-FABP1. No significant differences ($P > 0.05$) were observed in the hepatic genes expression of acetyl-CoA carboxylase (ACC), fatty acid synthase (FAS), hormone-sensitive lipase and carnitine palmitoyltransferase 1 alpha, and TC level (Figure 2(b)) among these groups.

3.4. RSV Improves the Hepatic Redox Status of Piglets. Since OS is implicated in IUGR-induced liver injury, we also tested whether RSV improves hepatic redox status of the IUGR piglets. As shown in Figure 4, compared with the NBW piglets, the higher ($P < 0.05$) concentrations of MDA and PC, the lower ($P = 0.096$) T-SOD activity, and the reduced ($P < 0.05$) GSH level were observed in the IUGR piglets. Resveratrol treatment reduced MDA and PC contents and increased GR activity and GSH level in the liver of piglets ($P < 0.05$). There was an interaction between BW and RSV treatment for hepatic MDA, PC, and GSH levels ($P < 0.05$). Treatment with RSV ameliorated ($P < 0.05$) the increased hepatic MDA and PC concentrations induced by IUGR and increased ($P < 0.05$) hepatic GSH level in the NBW piglets rather than in the IUGR piglets. The mRNA expression of heme oxygenase 1 (HO1, $P = 0.077$, Figure 5) and SOD1 ($P < 0.05$) in the liver was downregulated by IUGR compared with NBW. Hepatic GPX1 gene expression was upregulated by oral RSV administration ($P < 0.05$). There was a significant interaction between BW and RSV treatment for the mRNA abundance of hepatic Kelch-like ECH-associated protein 1 ($P < 0.05$). There were no significant differences ($P > 0.05$) in hepatic genes expression of nuclear factor erythroid-derived 2-like 2, glutamate-cysteine ligase catalytic subunit, glutamate-cysteine ligase modifier subunit, and GR as well as GPX activity.

3.5. RSV Affects the Hepatic Immune Status of Piglets. Abnormal immune response is a key event in IUGR-induced liver injury. Therefore, we also studied the effect of RSV on hepatic inflammation of the IUGR piglets. Compared with the NBW piglets, IUGR decreased ($P < 0.05$, Figure 6) the hepatic

TABLE 1: Sequences for real-time PCR primers.

Gene	GenBank ID	Sequence (5' → 3', forward primer/reverse primer)	Product length (bp)
Nrf2	XM_013984303.2	ATCCAGCGGATTGCTCGTAG TCAAATCCATGTCCTTGCGG	155
Keap1	NM_001114671.1	TCTGCTTAGTCATGGTGACCT GGGGTTCCAGATGACAAGGG	158
HO1	NM_001004027.1	TGATGGCGTCCTTGTACCAC GACCGGGTTCTCCTTGTGT	71
SOD1	NM_001190422.1	CATTCCATCATTGGCCGCAC TTACACCACAGGCCAAACGA	118
GPX1	NM_214201.1	CCTCAAGTACGTCCGACCAG GTGAGCATTGCGCCATTCA	85
GCLC	XM_003482164.4	CTAGTGGGTAGGCGGACTGG CGGTGTCGTGCTCTAGCTTC	81
GCLM	XM_001926378.4	GGACAAAACCCAGTTGGAGC TCACACAGCAAGAGGCAAGA	86
GR	AY368271.1	GTGAGCCGACTGAACACCAT CAGGATGTGAGGAGCTGTGT	141
SREBP1c	NM_214157.1	GCGACGGTGCCTCTGGTAGT CGCAAGACGGCGGATTTA	218
PPAR α	NM_001044526.1	GGCACTGAACATCGAATGTAGAAT TGCAACCTTCACAGGCATGA	80
ACC	NM_001114269.1	ATCCCTCCTTGCCTCTCCTA ACTTCCCCTTCAGATTCCG	208
FAS	NM_001099930.1	TACCTTGTGGATCACTGCATAGA GGCGTCTCCTCCAAGTTCTG	113
SCD1	NM_213781.1	ATTGGGAGCTGTGGGTGAG AAGTTGATGTGCCAGCGGTA	90
HSL	NM_214315.3	GCAGCATCTTCTCCGCACA AGCCCTTGGGTAGAGTGACA	195
CPT1 α	NM_001129805.1	TCAAAAACGGCAAGATGGGC TGGAATGTTGGGGTTGGTGT	155
LPL	NM_214286.1	CACATTCACCAGAGGGTC TCATGGGAGCACTTCACG	177
L-FABP1	NM_001004046.2	AGGGGACATCGAAATCGTG TCACACTCCTTCCCAAGGT	103
CD36	NM_001044622.1	TGACCCAGCACTGAAGCAA AAGATATCAGTTAGGAGTCCGATGA	130
FATP1	NM_001083931.1	AGGTCTGGCGTGGGTCAAAG GGAGTAGAGGGCAAAGCAGG	208
MTTP	NM_214185.1	AGCAAAATGGTCCGTCGAGT CGAATGGGGACCACGTTCTA	114
MCP1	NM_214214.1	AAACGGAGACTTGGGCACAT GCAAGGACCCTTCCGTCATC	74
F4/80	XM_021083974.1	TCCTTCTCTTTTGGGGTGT GCCATTGACTCCAACGGAGA	73
CD11c	XR_002342355.1	GGAGCAAATGGACAGACCGT GAATGCAGGTGCAAAGGCAA	95
TLR4	GQ304754	TTTCTTGCAGTGGGTGCGAGG GGAAGGTGAGAACTGACGCA	161

TABLE 1: Continued.

Gene	GenBank ID	Sequence (5' → 3', forward primer/reverse primer)	Product length (bp)
MyD88	NM001099923.1	GTGCCGTCGGATGGTAGTG TCTGGAAGTCACATTCCTTGCTT	65
TRAF6	NM_001105286.1	GCTGCATCTATGGCATTGAAG CCACAGATAACATTTGCCAAAGG	71
NF- κ B, p65	NM_001114281.1	GGGGCGATGAGATCTTCCTG CACGTCGGCTTGTGAAAAGG	110
TNF- α	NM_214022.1	GCCCTTCCACCAACGTTTTC CAAGGGCTCTTGATGGCAGA	97
IL6	NM_214399.1	ACAAAGCCACCACCCCTAAC CGTGGACGGCATCAATCTCA	185
IL1 β	NM_214055.1	ATTCAGGGACCCTACCCTCTC ATCACTTCCTTGCGGGTTC	92
IL10	NM_214041.1	CGGCCAGTGAAGAGTTTCT GGCAACCCAGGTAACCCTTA	98
β -Actin	XM_003124280.5	CTCCAGAGCGCAAGTACTCC AATGCAACTAACAGTCCGCC	153

Nrf2: nuclear factor erythroid-derived 2-like 2; Keap1: Kelch-like ECH-associated protein 1; HO1: heme oxygenase 1; SOD1: superoxide dismutase 1; GPX1: glutathione peroxidase 1; GCLC: glutamate-cysteine ligase catalytic subunit; GCLM: glutamate-cysteine ligase modifier subunit; GR: glutathione reductase; SREBP1c: sterol regulatory element-binding protein 1c; FAS: fatty acid synthase; ACC: acetyl-CoA carboxylase; SCD1: stearoyl-CoA desaturase 1; PPAR α , peroxisome proliferator-activated receptor alpha; HSL: hormone-sensitive lipase; CPT1 α : carnitine palmitoyltransferase 1 alpha; LPL: lipoprotein lipase; L-FABP1: liver fatty acid-binding proteins 1; CD36: cluster of differentiation 36; FATP1: fatty acid transport proteins 1; MTTP: microsomal triglyceride transfer protein; MCP1: monocyte chemotactic protein 1; F4/80: adhesion G protein-coupled receptor E1; CD11c: integrin alpha X; TLR4: toll-like receptor 4; MyD88: myeloid differentiation factor 88; TRAF6: tumor necrosis factor receptor-associated factor 6; NF- κ B: nuclear factor- κ B; TNF- α : tumor necrosis factor alpha; IL-6: interleukin 6; IL1 β : interleukin 1 β ; IL10: interleukin 10; β -actin: beta actin.

TABLE 2: Growth performance and organ weight of piglets at 21 days of age.

Items	NBW-CON	NBW-RSV	IUGR-CON	IUGR-RSV	P value		
					BW	RSV	BW \times RSV
ABW (kg)	7.17 \pm 0.18	6.94 \pm 0.12	4.32 \pm 0.09	4.45 \pm 0.12	<0.001	0.995	0.337
Liver (g)	185.62 \pm 7.22	190.52 \pm 3.56	142.63 \pm 12.81	164.15 \pm 5.20	<0.001	0.114	0.311
Liver relative weight (g/kg)	25.43 \pm 1.13	22.00 \pm 0.39	26.78 \pm 2.10	26.60 \pm 0.89	0.032	0.176	0.219

ABW: average body weight; BW: birth weight; RSV: resveratrol; NBW-CON: normal birth weight piglets orally fed with 0.5% carboxymethylcellulose sodium; NBW-RSV: normal birth weight piglets orally fed with 80 mg RSV/kg body weight/d; IUGR-CON: intrauterine growth-retarded piglets orally fed with 0.5% carboxymethylcellulose sodium; IUGR-RSV: intrauterine growth-retarded piglets orally fed with 80 mg RSV/kg body weight/d. Results present as means and standard errors, $n = 6$.

TNF- α concentration in the piglets. Resveratrol reduced TNF- α concentration in the liver of piglets ($P < 0.05$). There was a significant interaction between BW and RSV treatment for hepatic TNF- α concentration ($P < 0.05$); RSV treatment to the NBW piglets led to a significant decrease in hepatic TNF- α concentration. Hepatic toll-like receptor 4 (TLR4) gene expression in the IUGR piglets was lower than those in the NBW piglets ($P < 0.05$, Figure 7). Gene expression of monocyte chemotactic protein 1 (MCP1) in the liver of piglets was increased by RSV administration ($P < 0.05$). There was an interaction between BW and RSV treatment for hepatic TNF- α ($P < 0.05$) and MCP1 ($P = 0.060$) genes expression. Resveratrol increased TNF- α gene expression in the liver of IUGR piglets ($P < 0.05$). Hepatic genes expression of CD11c, adhesion G protein-coupled receptor E1, myeloid differentiation factor 88, tumor necrosis factor receptor-

associated factor 6, nuclear factor- κ B p65, interleukin 6 (IL6), IL1 β , and IL10 were not affected ($P > 0.05$) among these groups.

4. Discussion

The occurrence of NAFLD in IUGR offspring endangers public health. NAFLD represents a spectrum of pathological changes from hepatic steatosis (fatty liver) without hepatocellular damage to nonalcoholic steatohepatitis which is the extreme form of the disease characterized by excessive fat accumulation (triglycerides) in hepatocytes [30, 31]. Besides, OS and inflammation play an important role in the development of NAFLD subjects associated with IUGR [32]. Yamada et al. [33] reported that IUGR newborns persistently exhibited an increase in hepatic lipid content and upregulated lipogenic

TABLE 3: Glycolipid metabolism parameters in plasma of piglets at 21 days of age.

Items	NBW-CON	NBW-RSV	IUGR-CON	IUGR-RSV	<i>P</i> value		
					BW	RSV	BW × RSV
HDL-C (mmol/L)	1.97 ± 0.15	1.84 ± 0.12	1.70 ± 0.08	1.69 ± 0.23	0.192	0.662	0.715
LDL-C (mmol/L)	1.38 ± 0.24	0.88 ± 0.07	0.96 ± 0.29	0.85 ± 0.08	0.269	0.137	0.330
TG (mmol/L)	1.25 ± 0.19 ^a	0.66 ± 0.05 ^b	0.94 ± 0.12 ^{ab}	0.95 ± 0.07 ^{ab}	0.901	0.028	0.021
TC (mmol/L)	7.06 ± 0.96	5.47 ± 0.39	4.90 ± 0.71	5.38 ± 0.45	0.107	0.416	0.136
FFA (μmol/L)	200 ± 24.70	116.71 ± 12.65	135.44 ± 4.70	81.73 ± 2.80	0.002	<0.001	0.308
Glu (mmol/L)	20.49 ± 1.76	18.99 ± 1.45	21.83 ± 1.73	16.47 ± 1.93	0.736	0.061	0.278
Insulin (μIU/mL)	31.89 ± 13.20	23.83 ± 5.79	26.40 ± 9.02	24.43 ± 6.34	0.791	0.586	0.741
HOMA-IR	28.27 ± 10.80	20.11 ± 5.58	26.00 ± 9.37	18.15 ± 4.75	0.795	0.331	0.985

FFA: free fatty acids; Glu: glucose; HDL-C: high-density lipoprotein cholesterol; HOMA-IR: homeostasis model assessment of insulin resistance; LDL-C: low-density lipoprotein cholesterol; TC: total cholesterol; TG: total triglycerides; BW: birth weight; RSV: resveratrol; NBW-CON: normal birth weight piglets orally fed with 0.5% carboxymethylcellulose sodium; NBW-RSV: normal birth weight piglets orally fed with 80 mg RSV/kg body weight/d; IUGR-CON: intrauterine growth-retarded piglets orally fed with 0.5% carboxymethylcellulose sodium; IUGR-RSV: intrauterine growth-retarded piglets orally fed with 80 mg RSV/kg body weight/d. Results present as means and standard errors, $n = 6$. Means in a row without a common letter differ significantly ($P < 0.05$).

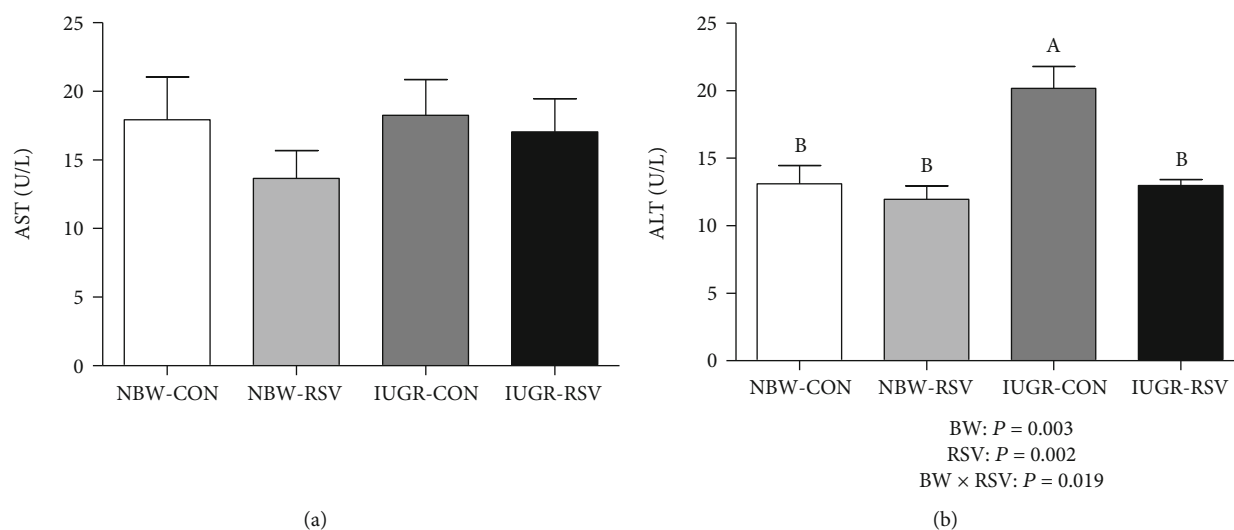


FIGURE 1: Aminotransferase activities in plasma of piglets at 21 days of age. (a) AST: aspartate aminotransferase; (b) ALT: alanine aminotransferase. BW: birth weight; RSV: resveratrol; NBW-CON: normal birth weight piglets orally fed with 0.5% carboxymethylcellulose sodium; NBW-RSV: normal birth weight piglets orally fed with 80 mg RSV/kg body weight/d; IUGR-CON: intrauterine growth-retarded piglets orally fed with 0.5% carboxymethylcellulose sodium; IUGR-RSV: intrauterine growth-retarded piglets orally fed with 80 mg RSV/kg body weight/d. The column and its bar represented the means value and standard error, $n = 6$, respectively. Means without a common letter differ significantly ($P < 0.05$).

indices, which suggests that fatty liver occurs early in IUGR offspring. As expected, in the present study, hepatic dysfunction and injury in the IUGR piglets were evidenced by the increased plasma ALT activity, hepatic OS, and lipid accumulation, which were alleviated by oral RSV administration.

The accumulation of lipid in the liver is due to the fact that fatty acid uptake and synthesis exceed hepatocyte oxidative capacity [32]. The present study found that IUGR increased TG and FFA concentrations and the mRNA expression of SREBP1c, SCD1, and L-FABP1 in the liver of piglets. SREBP1c, a nuclear transcription regulator, can regulate lipogenic genes expression including ACC, SCD1, and FAS. SCD1 is a microsomal enzyme which catalyzes the syn-

thesis of monounsaturated long-chain fatty acids from saturated fatty acyl-CoAs [34]. A previous study reported that liver-specific SCD1 inhibition resulted in decreased rates of fatty acid synthesis and downregulated expression of key lipogenic genes (e.g., FAS and ACC), partly through reduced transcription of SREBP1c [35]. Thus, the genes expression levels of SREBP1c and SCD1 are critical for hepatic *de novo* lipogenesis. L-FABP1 may facilitate the transport of fatty acids across the cellular membrane, and fatty acids may be involved in metabolic, inflammatory, and oxidative responses [34]. Interestingly, we also found that IUGR decreased hepatic LPL, HL, and TL activities of piglets. LPL and HL, members of the family of triglyceride lipase, are to catalyze the hydrolysis

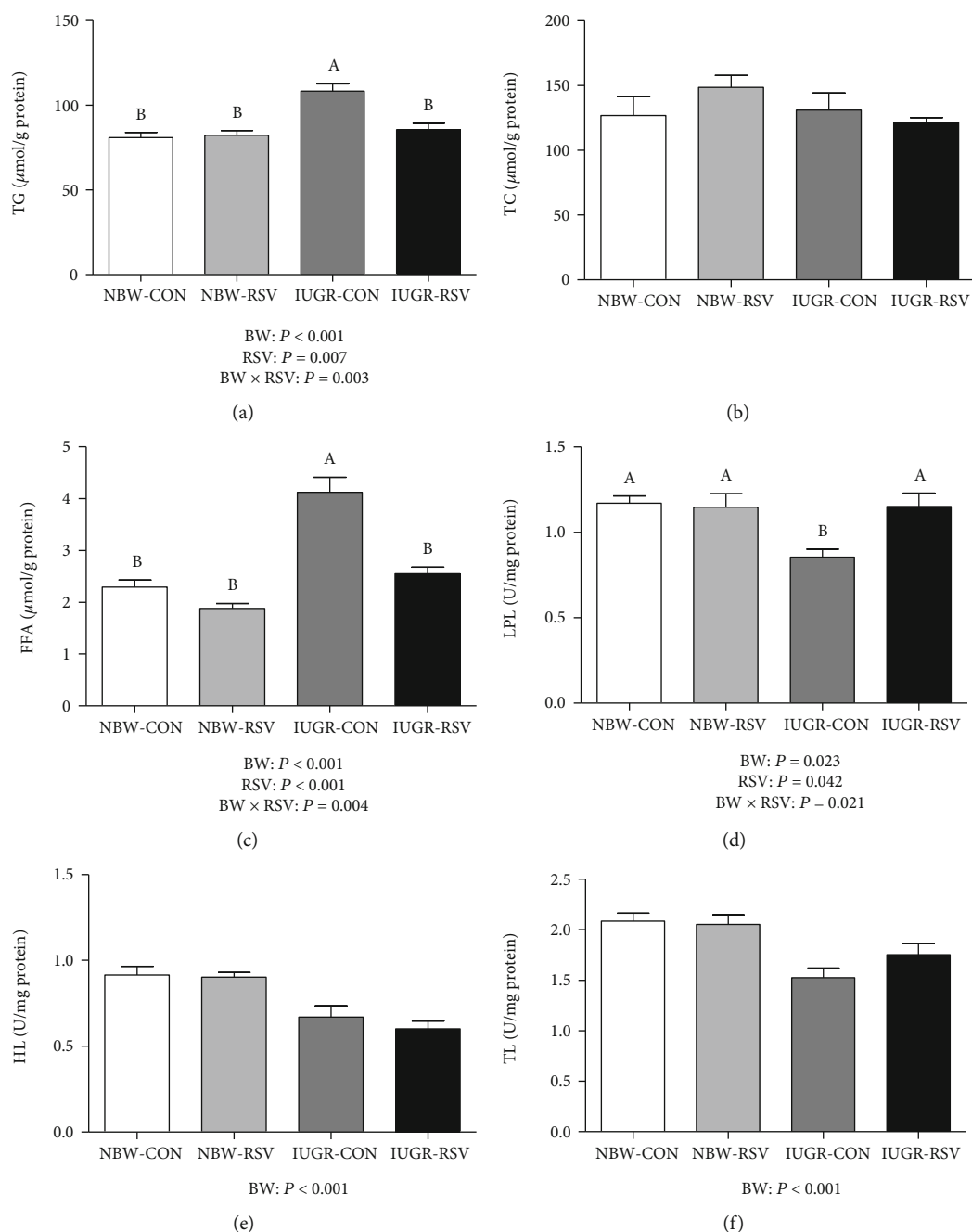


FIGURE 2: Hepatic lipid metabolism parameters of piglets at 21 days of age. (a) TG: total triglycerides; (b) TC: total cholesterol; (c) FFA: free fatty acids; (d) LPL: lipoprotein lipase; (e) HL: hepatic lipase; (f) TL: total lipase; BW: birth weight; RSV: resveratrol; NBW-CON: normal birth weight piglets orally fed with 0.5% carboxymethylcellulose sodium; NBW-RSV: normal birth weight piglets orally fed with 80 mg RSV/kg body weight/d; IUGR-CON: intrauterine growth-retarded piglets orally fed with 0.5% carboxymethylcellulose sodium; IUGR-RSV: intrauterine growth-retarded piglets orally fed with 80 mg RSV/kg body weight/d. The column and its bar represented the means value and standard error, $n = 6$, respectively. Means without a common letter differ significantly ($P < 0.05$).

of triacylglycerol in circulating lipoproteins such as chylomicron and very low-density lipoprotein, providing FFA and glycerol for tissue storage or utilization [36]. The results of this study indicated that IUGR increased hepatic *de novo* lipogenesis and direct fatty acid uptake of piglets, leading to hepatic lipid accumulation. Similar results were obtained in an IUGR piglet model which was conducted by He et al. [15]. In addition, the reduced circulatory FFA level in IUGR piglets may

be attributed to the increased uptake of fatty acid in the liver. Expectedly, RSV decreased hepatic TG and FFA concentrations and increased hepatic LPL activity and its gene expression of the IUGR piglets. However, RSV had no effects on the genes expression of lipogenesis in the liver of IUGR piglets. Zhang et al. [24] found that IUGR impaired mitochondrial biogenesis and energy homeostasis in the liver of piglets, and these negative influences were restored by RSV.

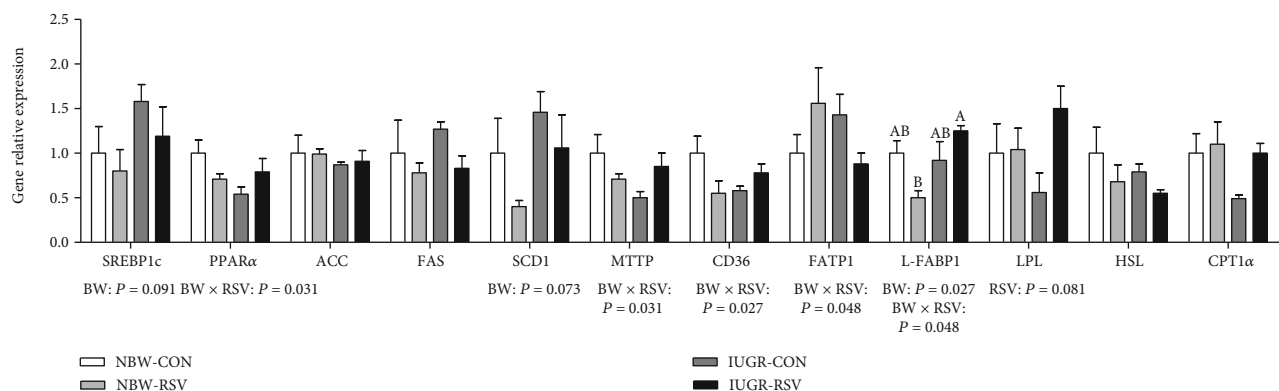


FIGURE 3: Genes expression related to lipid metabolism in the liver of piglets at 21 days of age. BW: birth weight; RSV: resveratrol; SREBP1c: sterol regulatory element-binding protein 1c; PPAR α : peroxisome proliferator-activated receptor alpha; ACC: acetyl-CoA carboxylase; FAS: fatty acid synthase; SCD1: stearoyl-CoA desaturase 1; MTP: microsomal triglyceride transfer protein; CD36: cluster of differentiation 36; FATP1: fatty acid transport proteins 1; L-FABP1: liver fatty acid-binding proteins 1; LPL: lipoprotein lipase; HSL: hormone sensitive lipase; CPT1 α : carnitine palmitoyltransferase 1 alpha; NBW-CON: normal birth weight piglets orally fed with 0.5% carboxymethylcellulose sodium; NBW-RSV: normal birth weight piglets orally fed with 80 mg RSV/kg body weight/d; IUGR-CON: intrauterine growth-retarded piglets orally fed with 0.5% carboxymethylcellulose sodium; IUGR-RSV: intrauterine growth-retarded piglets orally fed with 80 mg RSV/kg body weight/d. The column and its bar represented the means value and standard error, $n = 5$, respectively. Means without a common letter differ significantly ($P < 0.05$).

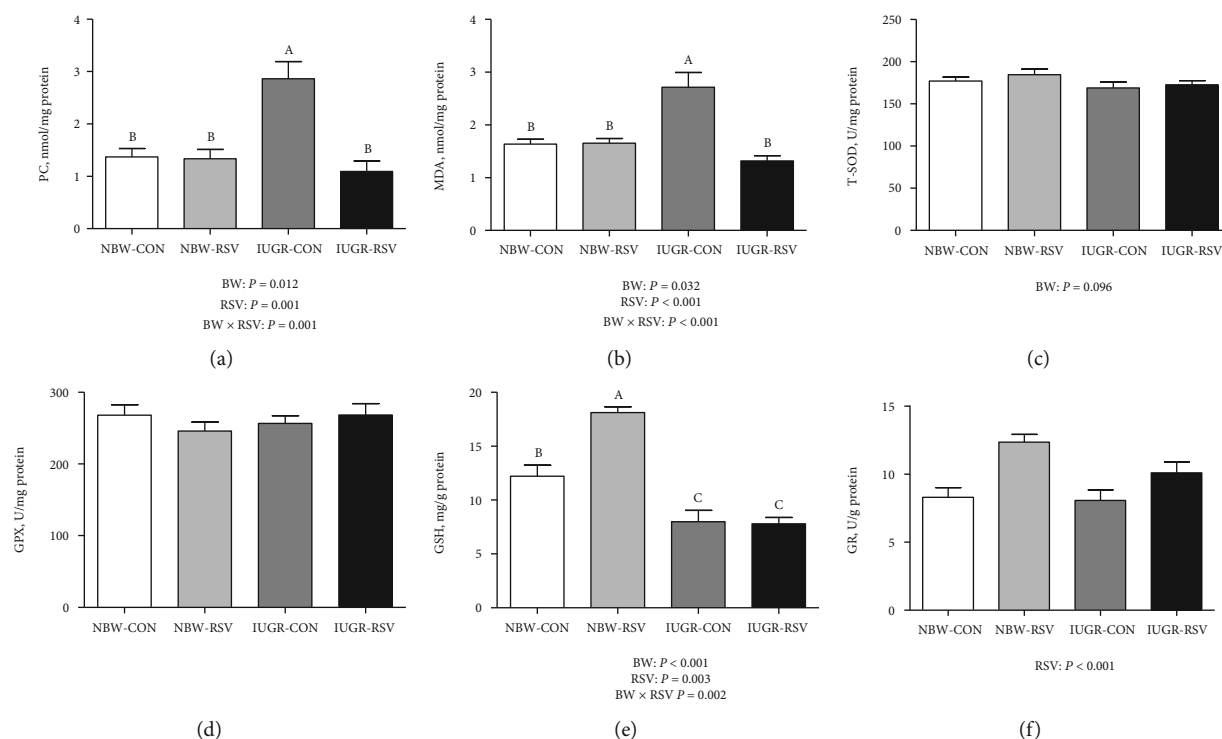


FIGURE 4: Redox status in the liver of piglets at 21 days of age. (a) PC: protein carbonyl; (b) MDA: malondialdehyde; (c) T-SOD: total superoxide dismutase; (d) GPX: glutathione peroxidase; (e) GSH: reduced glutathione; (f) GR: glutathione reductase; BW: birth weight; RSV: resveratrol; NBW-CON: normal birth weight piglets orally fed with 0.5% carboxymethylcellulose sodium; NBW-RSV: normal birth weight piglets orally fed with 80 mg RSV/kg body weight/d; IUGR-CON: intrauterine growth-retarded piglets orally fed with 0.5% carboxymethylcellulose sodium; IUGR-RSV: intrauterine growth-retarded piglets orally fed with 80 mg RSV/kg body weight/d. The column and its bar represented the means value and standard error, $n = 6$, respectively. Means without a common letter differ significantly ($P < 0.05$).

Mitochondria are important organelles which are essential for energy generation and are the primary site for fatty acid β -oxidation [37], indicating that normal mitochondrial function plays a vital role in hepatic lipid equilibrium. This study sug-

gested that the lipid-lowering effect of RSV on the liver of IUGR piglets may be through the improvement of mitochondrial function rather than the inhibition of lipid synthesis and uptake.

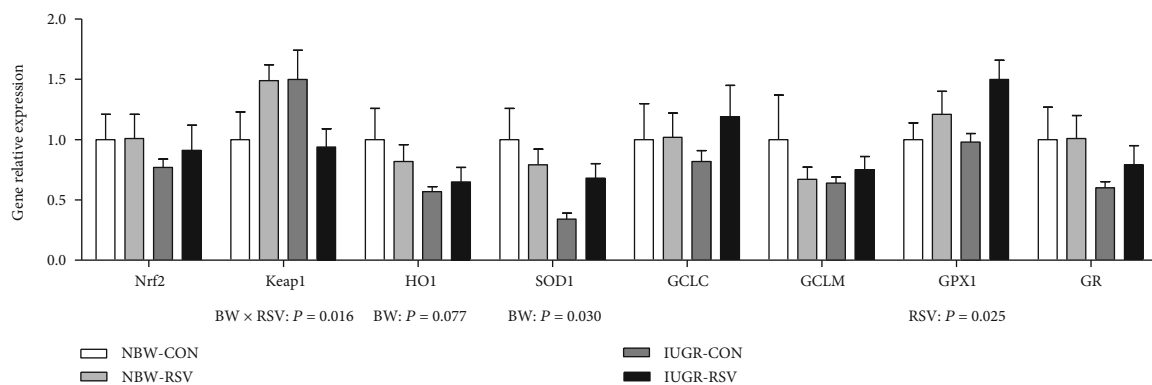


FIGURE 5: Genes expression related to antioxidation in the liver of piglets at 21 days of age. BW: birth weight; RSV: resveratrol; Nrf2: nuclear factor erythroid-derived 2-like 2; Keap1: Kelch-like ECH-associated protein 1; HO1: heme oxygenase 1; SOD1: superoxide dismutase 1; GCLC: glutamate-cysteine ligase catalytic subunit; GCLM: glutamate-cysteine ligase modifier subunit; GPX1: glutathione peroxidase 1; GR: glutathione reductase; NBW-CON: normal birth weight piglets orally fed with 0.5% carboxymethylcellulose sodium; NBW-RSV: normal birth weight piglets orally fed with 80 mg RSV/kg body weight/d; IUGR-CON: intrauterine growth-retarded piglets orally fed with 0.5% carboxymethylcellulose sodium; IUGR-RSV: intrauterine growth-retarded piglets orally fed with 80 mg RSV/kg body weight/d. The column and its bar represented the means value and standard error, $n = 5$, respectively. Means without a common letter differ significantly ($P < 0.05$).

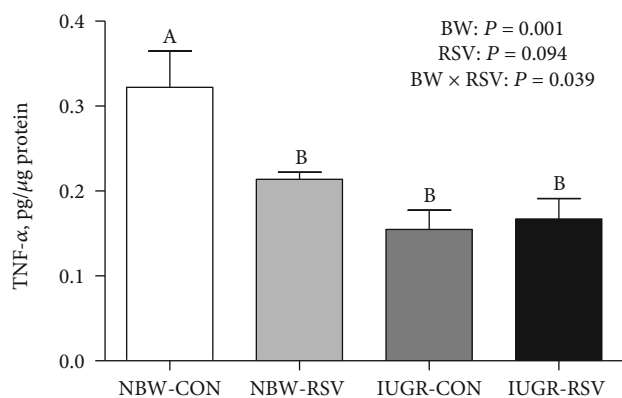


FIGURE 6: Tumor necrosis factor alpha (TNF- α) concentration in the liver of piglets at 21 days of age. BW: birth weight; RSV: resveratrol; NBW-CON: normal birth weight piglets orally fed with 0.5% carboxymethylcellulose sodium; NBW-RSV: normal birth weight piglets orally fed with 80 mg RSV/kg body weight/d; IUGR-CON: intrauterine growth-retarded piglets orally fed with 0.5% carboxymethylcellulose sodium; IUGR-RSV: intrauterine growth-retarded piglets orally fed with 80 mg RSV/kg body weight/d. The column and its bar represented the means value and standard error, $n = 6$, respectively. Means without a common letter differ significantly ($P < 0.05$).

The balance of redox status in the organism is achieved by reactive oxygen species (ROS) production and antioxidant defense capacity and is essential for maintaining the normal function of organs (e.g., liver) [38]. The excessive generation of ROS damages lipids, proteins, and DNA due to the impairment of the antioxidant system [5], indicating that OS occurs. In the present study, hepatic MDA and PC levels were increased in the IUGR piglets, which was consistent with a previous study [25]. MDA and PC contents reflect the degree of lipid peroxidation and protein oxidation, respectively, and are regarded as the index of OS [39]. Obviously, in the present study, hepatic OS in the IUGR piglets was observed and

may be due to the reduced T-SOD activity and GSH level. The antioxidant defense system in cells, including enzymatic (e.g., SOD) and nonenzymatic (e.g., GSH) antioxidants, protects the organism against oxidative damage [40]. SOD catalyzes the reduction of the superoxide anion to hydrogen peroxide, which is further decomposed into water and oxygen by GPX or/and catalase [5]. GSH with its sulfhydryl group functions in the maintenance of sulfhydryl groups of other molecules (especially proteins), as a catalyst for disulfide exchange reactions, and in the detoxification of foreign compounds and free radicals [41]. Similar to previous studies [25, 39], IUGR harms antioxidant levels in offspring, which partly leads to OS. In addition, another reason for hepatic OS of the IUGR piglets is the overproduction of mitochondrial ROS. Mitochondrial fatty acid oxidation increases in response to excessive hepatic fat accumulation [42], and then, the generation of ROS was elevated in the liver. Interestingly, the elevated hepatic TG and FFA concentrations were found in the IUGR piglets. Thus, the enhancement of antioxidant defense is beneficial for lipid balance and redox status. In the present study, RSV administration reduced MDA and PC concentrations and increased GR activity and GSH level in the liver of piglets. Similar results observed in rodents' studies demonstrated that RSV enhances the activities of various antioxidant enzymes (e.g., SOD and GPX) and the induction of GSH by regulating various signaling pathways including Nrf2 and nuclear factor κ B [43]. Zhang et al. [44] reported that dietary RSV supplementation increased antioxidative capacity, GPX activity, and its mRNA level in the longissimus dorsi of finishing pigs. In the present study, RSV treatment only upregulated hepatic GPX1 mRNA expression of piglets but had no effects on other related genes expressions, which indicated that RSV may improve hepatic redox status through the posttranslational protein modifications rather than the mRNA level regulation. The deeper molecular mechanism needs to be further investigated. In the present study, we speculated that RSV alleviated IUGR-induced increased MDA and PC concentrations in the liver

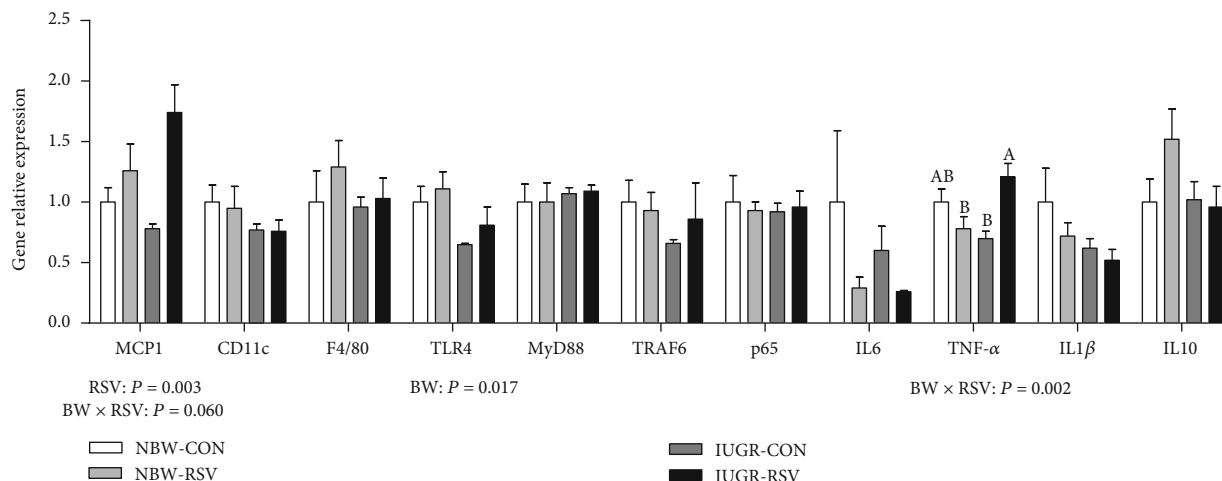


FIGURE 7: Genes expression related to inflammation in the liver of piglets at 21 days of age. BW: birth weight; RSV: resveratrol; MCP1: monocyte chemoattractant protein 1; CD11c: integrin alpha X; F4/80: adhesion G protein-coupled receptor E1; TLR4: toll-like receptor 4; MyD88: myeloid differentiation factor 88; TRAF6: tumor necrosis factor receptor-associated factor 6; NF- κ B p65: nuclear factor- κ B; IL-6: interleukin 6; TNF- α : tumor necrosis factor alpha; IL1 β : interleukin 1 β ; IL10: interleukin 10; NBW-CON: normal birth weight piglets orally fed with 0.5% carboxymethylcellulose sodium; NBW-RSV: normal birth weight piglets orally fed with 80 mg RSV/kg body weight/d; IUGR-CON: intrauterine growth-retarded piglets orally fed with 0.5% carboxymethylcellulose sodium; IUGR-RSV: intrauterine growth-retarded piglets orally fed with 80 mg RSV/kg body weight/d. The column and its bar represented the means value and standard error, $n = 5$, respectively. Means without a common letter differ significantly ($P < 0.05$).

of suckling piglets by reducing ROS production via the enhancement of hepatic mitochondrial function [24] and the improvement of redox status.

Anti- and pro-inflammatory cytokine levels generated by immune cells are very important to resist the invasion of foreign antigens. TLR4 is a member of toll-like receptor and mediates the innate immune responses. However, defects at the level of expression of TLR4 could contribute to poor recruitment of antigen-presenting cells, and T and B cells at the site of inflammation, resulting in suboptimal adaptive immune responses which leads to the increased risk of infections with Gram-negative bacteria [45]. In the present study, IUGR piglets exhibited decreased hepatic TNF- α content, which may be related to the reduced TLR4 and TNF- α genes expression. The results suggested that IUGR can impair the hepatic immune function of piglets and increase the risk of illness. Similar results were shown in a piglet study in which IUGR markedly decreased mRNA abundance of TLR9 and toll-interacting protein in the ileum of piglets during the suckling period [46]. In the present study, although RSV upregulated hepatic MCP1 and TNF- α genes expression in the IUGR piglets, hepatic TNF- α protein content in the IUGR piglets was not altered by RSV. However, it is lacking the effect of RSV on the inflammation of pigs. The underlying mechanisms involved in the beneficial effect of RSV on hepatic inflammation of the IUGR piglets need to be investigated in the future.

5. Conclusions

In conclusion, oral RSV treatment reduced hepatic fat accumulation and OS in the IUGR piglets, which may suggest a potential nutritional strategy to prevent or/and slow the development of NAFLD in human infants with IUGR.

Data Availability

The data used to support the findings of this study are available from the corresponding authors upon request.

Conflicts of Interest

The authors declare that there are no conflicts of interest.

Acknowledgments

The present study was supported by the Fundamental Research Funds for the Central Universities (Grant No. KJQN201935), the National Natural Science Foundation of China (Grant Nos. 31802101, 31772634, and 31802094), and the Natural Science Foundation of Jiangsu Province (Grants No BK20180531).

References

- [1] S. M. Grundy, Brewer HB Jr, J. I. Cleeman et al., "Definition of metabolic syndrome: report of the National Heart, Lung, and Blood Institute/American Heart Association conference on scientific issues related to definition," *Circulation*, vol. 109, no. 3, pp. 433–438, 2004.
- [2] C. Y. Hou, Y. L. Tain, H. R. Yu, and L. T. Huang, "The effects of resveratrol in the treatment of metabolic Syndrome," *International Journal of Molecular Sciences*, vol. 20, no. 3, p. 535, 2019.
- [3] K. Cusi, "Role of obesity and lipotoxicity in the development of nonalcoholic steatohepatitis: pathophysiology and clinical implications," *Gastroenterology*, vol. 142, no. 4, pp. 711–725.e6, 2012.
- [4] T. Charytoniuk, K. Drygalski, K. Konstantynowicz-Nowicka, K. Berk, and A. Chabowski, "Alternative treatment methods attenuate the development of NAFLD: a review of resveratrol

- molecular mechanisms and clinical trials,” *Nutrition*, vol. 34, pp. 108–117, 2017.
- [5] K. Cheng, Z. Song, H. Zhang et al., “The therapeutic effects of resveratrol on hepatic steatosis in high-fat diet-induced obese mice by improving oxidative stress, inflammation and lipid-related gene transcriptional expression,” *Medical Molecular Morphology*, vol. 52, no. 4, pp. 187–197, 2019.
 - [6] M. G. M. Pruis, P. A. van Ewijk, V. B. Schrauwen-Hinderling, and T. Plösch, “Lipotoxicity and the role of maternal nutrition,” *Acta Physiologica*, vol. 210, no. 2, pp. 296–306, 2014.
 - [7] V. Nobili, M. Marcellini, G. Marchesini et al., “Intrauterine growth retardation, insulin resistance, and nonalcoholic fatty liver disease in children,” *Diabetes Care*, vol. 30, no. 10, pp. 2638–2640, 2007.
 - [8] A. Fraser, S. Ebrahim, G. D. Smith, and D. A. Lawlor, “The associations between birthweight and adult markers of liver damage and function,” *Paediatric and Perinatal Epidemiology*, vol. 22, no. 1, pp. 12–21, 2007.
 - [9] K. P. Newton, H. S. Feldman, C. D. Chambers et al., “Low and high birth weights are risk factors for nonalcoholic fatty liver disease in children,” *The Journal of Pediatrics*, vol. 187, pp. 141–146.e1, 2017.
 - [10] M. A. Hyatt, D. S. Gardner, S. Sebert et al., “Suboptimal maternal nutrition, during early fetal liver development, promotes lipid accumulation in the liver of obese offspring,” *Reproduction*, vol. 141, no. 1, pp. 119–126, 2011.
 - [11] C. A. Merrifield, M. Lewis, S. P. Claus et al., “A metabolic system-wide characterisation of the pig: a model for human physiology,” *Molecular Biosystems*, vol. 7, no. 9, pp. 2577–2588, 2011.
 - [12] K. Ferenc, P. Pietrzak, M. M. Godlewski et al., “Intrauterine growth retarded piglet as a model for humans - Studies on the perinatal development of the gut structure and function,” *Reproductive Biology*, vol. 14, no. 1, pp. 51–60, 2014.
 - [13] C. Burke, K. Sinclair, G. Cowin et al., “Intrauterine growth restriction due to uteroplacental vascular insufficiency leads to increased hypoxia-induced cerebral apoptosis in newborn piglets,” *Brain Research*, vol. 1098, no. 1, pp. 19–25, 2006.
 - [14] Z. Ying, H. Zhang, W. Su et al., “Dietary methionine restriction alleviates hyperglycemia in pigs with intrauterine growth restriction by enhancing hepatic protein kinase B signaling and glycogen synthesis,” *The Journal of Nutrition*, vol. 147, no. 10, pp. 1892–1899, 2017.
 - [15] J. He, L. Dong, W. Xu et al., “Dietary tributyrin supplementation attenuates insulin resistance and abnormal lipid metabolism in suckling piglets with intrauterine growth retardation,” *PLoS One*, vol. 10, no. 8, article e0136848, 2015.
 - [16] L. Shen, M. Gan, S. Zhang et al., “Transcriptome analyses reveal adult metabolic syndrome with intrauterine growth restriction in pig models,” *Frontiers in Genetics*, vol. 9, p. 291, 2018.
 - [17] L. Che, Y. Xuan, L. Hu et al., “Effect of postnatal nutrition restriction on the oxidative status of neonates with intrauterine growth restriction in a pig model,” *Neonatology*, vol. 107, no. 2, pp. 93–99, 2015.
 - [18] J. Liu, J. He, Y. Yang et al., “Effects of intrauterine growth retardation and postnatal high-fat diet on hepatic inflammatory response in pigs,” *Archives of Animal Nutrition*, vol. 68, no. 2, pp. 111–125, 2014.
 - [19] K. Ferenc, P. Pietrzak, M. Wierzbicka et al., “Alterations in the liver of intrauterine growth retarded piglets may predispose to development of insulin resistance and obesity in later life,” *Journal of Physiology and Pharmacology*, vol. 69, no. 2, pp. 211–218, 2018.
 - [20] S. W. Li, H. R. Yu, J. M. Sheen et al., “A maternal high-fat diet during pregnancy and lactation, in addition to a postnatal high-fat diet, leads to metabolic syndrome with spatial learning and memory deficits: beneficial effects of resveratrol,” *Oncotarget*, vol. 8, no. 67, pp. 111998–112013, 2017.
 - [21] M. Jiang, X. Li, X. Yu et al., “Oral administration of resveratrol alleviates osteoarthritis pathology in C57BL/6J mice model induced by a high-fat diet,” *Mediators of Inflammation*, vol. 2017, Article ID 7659023, 11 pages, 2017.
 - [22] K. Cheng, Z. Song, Y. Chen et al., “Resveratrol protects against renal damage via attenuation of inflammation and oxidative stress in high-fat-diet-induced obese mice,” *Inflammation*, vol. 42, no. 3, pp. 937–945, 2019.
 - [23] A. A. Sabe, A. A. Sadek, N. Y. Elmadhun et al., “Investigating the effects of resveratrol on chronically ischemic myocardium in a swine model of metabolic syndrome: a proteomics analysis,” *Journal of Medicinal Food*, vol. 18, no. 1, pp. 60–66, 2015.
 - [24] H. Zhang, Y. Li, W. Su et al., “Resveratrol attenuates mitochondrial dysfunction in the liver of intrauterine growth retarded suckling piglets by improving mitochondrial biogenesis and redox status,” *Molecular Nutrition & Food Research*, vol. 61, no. 5, p. 1600653, 2017.
 - [25] H. Zhang, W. Su, Z. Ying et al., “N-acetylcysteine attenuates intrauterine growth retardation-induced hepatic damage in suckling piglets by improving glutathione synthesis and cellular homeostasis,” *European Journal of Nutrition*, vol. 57, no. 1, pp. 327–338, 2018.
 - [26] D. R. Matthews, J. P. Hosker, A. S. Rudenski, B. A. Naylor, D. F. Treacher, and R. C. Turner, “Homeostasis model assessment: insulin resistance and β -cell function from fasting plasma glucose and insulin concentrations in man,” *Diabetologia*, vol. 28, no. 7, pp. 412–419, 1985.
 - [27] M. M. Bradford, “A rapid and sensitive method for the quantitation of microgram quantities of protein utilizing the principle of protein-dye binding,” *Analytical Biochemistry*, vol. 72, no. 1–2, pp. 248–254, 1976.
 - [28] Z. H. Song, K. Cheng, X. C. Zheng, H. Ahmad, L. L. Zhang, and T. Wang, “Effects of dietary supplementation with enzymatically treated *Artemisia annua* on growth performance, intestinal morphology, digestive enzyme activities, immunity, and antioxidant capacity of heat-stressed broilers,” *Poultry Science*, vol. 97, no. 2, pp. 430–437, 2018.
 - [29] K. J. Livak and T. D. Schmittgen, “Analysis of Relative Gene Expression Data Using Real-Time Quantitative PCR and the $2^{-\Delta\Delta C_T}$ Method,” *Methods*, vol. 25, no. 4, pp. 402–408, 2001.
 - [30] R. M. Williamson, J. F. Price, S. Glancy et al., “Prevalence of and risk factors for hepatic steatosis and nonalcoholic fatty liver disease in people with type 2 diabetes: the Edinburgh Type 2 Diabetes Study,” *Diabetes Care*, vol. 34, no. 5, pp. 1139–1144, 2011.
 - [31] J. Ludwig, T. R. Viggiano, D. McGill, and B. J. Oh, “Nonalcoholic steatohepatitis: Mayo Clinic experiences with a hitherto unnamed disease,” *Mayo Clinic Proceedings*, vol. 55, no. 7, pp. 434–438, 1980.
 - [32] M. Li, C. M. Reynolds, S. A. Segovia, C. Gray, and M. H. Vickers, “Developmental programming of nonalcoholic fatty liver disease: the effect of early life nutrition on susceptibility and disease severity in later life,” *Bio Med Research International*, vol. 2015, article 437107, 12 pages, 2015.

- [33] M. Yamada, D. Wolfe, G. Han, S. W. French, M. G. Ross, and M. Desai, "Early onset of fatty liver in growth-restricted rat fetuses and newborns," *Congenital Anomalies*, vol. 51, no. 4, pp. 167–173, 2011.
- [34] G. Musso, R. Gambino, and M. Cassader, "Recent insights into hepatic lipid metabolism in non-alcoholic fatty liver disease (NAFLD)," *Progress in Lipid Research*, vol. 48, no. 1, pp. 1–26, 2009.
- [35] G. Jiang, Z. Li, F. Liu et al., "Prevention of obesity in mice by antisense oligonucleotide inhibitors of stearoyl-CoA desaturase-1," *The Journal of Clinical Investigation*, vol. 115, no. 4, pp. 1030–1038, 2005.
- [36] H. Han, D. Dai, W. Wang et al., "Impact of serum levels of lipoprotein lipase, hepatic lipase, and endothelial lipase on the progression of coronary artery disease," *Journal of Interventional Medicine*, vol. 2, no. 1, pp. 16–20, 2019.
- [37] S. K. Mantena, A. L. King, K. K. Andringa, H. B. Eccleston, and S. M. Bailey, "Mitochondrial dysfunction and oxidative stress in the pathogenesis of alcohol- and obesity-induced fatty liver diseases," *Free Radical Biology & Medicine*, vol. 44, no. 7, pp. 1259–1272, 2008.
- [38] K. Cheng, M. Zhang, X. Huang et al., "An evaluation of natural and synthetic vitamin E supplementation on growth performance and antioxidant capacity of broilers in early age," *Canadian Journal of Animal Science*, vol. 98, no. 1, pp. 187–193, 2017.
- [39] H. Zhang, Y. Chen, Y. Li, L. Yang, J. Wang, and T. Wang, "Medium-chain TAG attenuate hepatic oxidative damage in intra-uterine growth-retarded weanling piglets by improving the metabolic efficiency of the glutathione redox cycle," *British Journal of Nutrition*, vol. 112, no. 6, pp. 876–885, 2014.
- [40] K. Cheng, Z. H. Song, X. C. Zheng et al., "Effects of dietary vitamin E type on the growth performance and antioxidant capacity in cyclophosphamide immunosuppressed broilers," *Poultry Science*, vol. 96, no. 5, pp. 1159–1166, 2017.
- [41] K. Manda and A. L. Bhatia, "Prophylactic action of melatonin against cyclophosphamide-induced oxidative stress in mice," *Cell Biology and Toxicology*, vol. 19, no. 6, pp. 367–372, 2003.
- [42] N. E. Sunny, E. J. Parks, J. D. Browning, and S. C. Burgess, "Excessive hepatic mitochondrial TCA cycle and gluconeogenesis in humans with nonalcoholic fatty liver disease," *Cell Metabolism*, vol. 14, no. 6, pp. 804–810, 2011.
- [43] V. L. Truong, M. Jun, and W. S. Jeong, "Role of resveratrol in regulation of cellular defense systems against oxidative stress," *Biofactors*, vol. 44, no. 1, pp. 36–49, 2018.
- [44] C. Zhang, J. Luo, B. Yu et al., "Dietary resveratrol supplementation improves meat quality of finishing pigs through changing muscle fiber characteristics and antioxidative status," *Meat Science*, vol. 102, pp. 15–21, 2015.
- [45] O. Equils, S. Singh, S. Karaburun, D. Lu, M. Thamotharan, and S. U. Devaskar, "Intra-uterine growth restriction downregulates the hepatic toll like receptor-4 expression and function," *Clinical & Developmental Immunology*, vol. 12, no. 1, pp. 59–66, 2005.
- [46] L. Hu, X. Peng, H. Chen et al., "Effects of intrauterine growth retardation and *Bacillus subtilis* PB6 supplementation on growth performance, intestinal development and immune function of piglets during the suckling period," *European Journal of Nutrition*, vol. 56, no. 4, pp. 1753–1765, 2017.